

# Suspension, yielding, microstructure and applications of bacterial cellulose dispersion

**Jie Song**

A thesis submitted in fulfilment  
of the requirements for the degree of  
Doctor of Philosophy



**UNSW**  
SYDNEY

**School of Chemical Engineering**  
**Faculty of Engineering**  
**University of New South Wales**

05 September 2019

## Abstract

Soft matter materials have been widely explored and applied because of their unique rheological response. One of the most common approaches to fluid microstructure design is to create a colloidal gel, a self-supported network that forms spontaneously from attractive particles. Fluid products containing colloidal gels have superior suspension abilities, because they possess a yield stress that makes the fluid elastic until a threshold stress is exceeded.

Yield stress fluids have been widely studied, but the local aspects of yielding, and the effects of particle shape on suspension performance are still not well-understood. This work examines the unique yielding of bacterial cellulose fiber networks using a new microrheology technique developed specifically for this purpose. The fiber gels exhibit a dynamic structural rearrangement response to applied stress that is shown to be advantageous in applications like particle suspension and surface coating.

The cellulose system and its unique structural and yielding properties are also studied in several systems with direct relevance to commercial formulated material production. A suspension of dense particles trapped within a cellulose fiber network is characterised as it slowly compresses and fails under its particulate load, and the phenomenon is used to measure gel permeability and model the long-time behaviour of such systems in order to predict stability.

Medical nasal sprays incorporating cellulose microfibrils are shown to be greatly enhanced in their ability to coat and adhere to surfaces, as the gel yield stress provides a more consistent flow resistance than traditional viscosity modification. Finally, a novel form of microcapsule is developed by engineering the growth of bacterial cellulose on emulsion droplet interfaces, creating soft, permeable shells with custom geometries. The structures are proposed as a new approach for encapsulation and protection, and potentially a framework for artificial cells.

## Acknowledgments

Firstly, I would like to give a very special thanks to my supervisor, Associate Professor Patrick T. Spicer, whom offered me a fantastic research opportunity in his group. This thesis would not have been possible without his guidance, advice and support. Thank you for sharing your expertise in colloidal science with me, especially with respect to rheology. Your excellent research taste, critical thinking and passion for research have profoundly affected me. You have taught me how to apply knowledge to solve practical problems, and also how to think more like an engineer, which will promisingly influence my future career. Again, I am very fortunate to have been accompanied by you as a supervisor, and also as a friend, during my PhD journey!

I would also like to thank my co-supervisor, Dr Stuart Prescott, for his valuable advice on the project. Thanks for constructing a computer-controlled bubble rheometer for my research.

Many thanks to Dr Marco Caggioni for great help and discussion, and nicely offering me an internship opportunity in Procter & Gamble Company, USA.

I am also grateful to Professor Todd Squires (University of California, Santa Barbara) and Professor James F. Gilchrist (Lehigh University) for discussing two-fluid yielding dynamics. Your ideas and support are very appreciated.

Thanks to Professor Paul Young and Professor Daniela Traini (Woolcock Institute of Medical Research), regarding applying microfibrillated cellulose in nasal drug delivery.

I also want to thank Professor Kuanyu Li (Nanjing University) whom supervised my Bachelor thesis. She helped me develop essential laboratory literacy which ultimately lead me into the world of research.

Many thanks to the lab managers, Camillo Taraborrelli and Eh Hau Pan, for providing access to the labs and instruments, to Dr Michael Carnell who delivers imaging suggestions and helps in BMIF, and to all other chemical engineering staff in UNSW who helped and supported my work and campus life.

I acknowledge all the Complex Fluids group members at UNSW: Haiqiao, Zengyi, Goldina, Prerna, Isaac, Zhiwei, Haoda, Firoozeh and Maryam. My time working

with you in the lab has been the happiest part throughout my PhD. You are the most lovely colleagues and friends I met.

I must mention my fiancé, Jinji Zha. Thank you for your company and understanding through the good and the bad.

Finally, to my father, mother and brother who unconditionally support me and encourage me to pursue what I like. You are always my staunch supporters. Thank you for believing in me.

# Contents

<b>Abstract</b>	<b>i</b>
<b>1 Introduction</b>	<b>1</b>
1.1 Parameters controlling gel structures and mechanical strength . . . . .	3
1.1.1 Size and aspect ratio . . . . .	3
1.1.2 Particle interactions . . . . .	8
1.1.3 Flexibility . . . . .	10
1.1.4 Structural heterogeneity . . . . .	11
1.2 Relating gel microstructure to yielding dynamics . . . . .	12
1.2.1 Linear elastic deformation . . . . .	14
1.2.2 Non-linear plasticity and restructuring . . . . .	16
1.2.3 Heterogeneous fiber network yielding . . . . .	17
1.3 Project aims and overview . . . . .	26
1.4 References . . . . .	28
<b>2 Heterogeneous yielding of microfibrillar cellulose gels: bubble rheometer</b>	<b>35</b>
2.1 Introduction . . . . .	35
2.2 Experimental methods . . . . .	37
2.2.1 Sample preparation . . . . .	37
2.2.2 Bulk rheology . . . . .	37
2.2.3 Microscale rheology . . . . .	39
2.3 Results and discussion . . . . .	41
2.4 Conclusions . . . . .	56
2.5 References . . . . .	57
<b>3 Strain rate-dependent yielding of microfibrillar cellulose gels</b>	<b>61</b>
3.1 Introduction . . . . .	61
3.2 Experimental methods . . . . .	63
3.2.1 Sample preparation . . . . .	63
3.2.2 Fiber imaging . . . . .	64
3.2.3 Critical suspension stress measurements . . . . .	64

3.2.4	Static structure deformation . . . . .	66
3.3	Results and discussion . . . . .	67
3.4	Conclusions . . . . .	77
3.5	References . . . . .	78
<b>4</b>	<b>Accelerated gravitational yielding of sparse fiber collidal gels</b>	<b>81</b>
4.1	Introduction . . . . .	81
4.2	Experimental methods . . . . .	83
4.2.1	Sample preparation . . . . .	83
4.2.2	Visual observations . . . . .	84
4.2.3	Rheology measurement . . . . .	85
4.2.4	Curve fitting and calculation . . . . .	86
4.3	Results and Discussion . . . . .	88
4.4	Conclusions . . . . .	99
4.5	References . . . . .	100
<b>5</b>	<b>Enhancing surface coating by adding microfibrinous cellulose</b>	<b>103</b>
5.1	Introduction . . . . .	103
5.2	Experimental methods . . . . .	105
5.2.1	Sample preparation . . . . .	105
5.2.2	Fiber network observation . . . . .	106
5.2.3	Rheological characterization . . . . .	106
5.2.4	Run-off film thickness measurements . . . . .	107
5.2.5	Surface tension measurements . . . . .	107
5.3	Results and discussion . . . . .	108
5.4	Conclusions . . . . .	114
5.5	References . . . . .	114
<b>6</b>	<b>Soft bacterial cellulose microcapsules with adaptable shapes</b>	<b>117</b>
6.1	Introduction . . . . .	117
6.2	Experimental methods . . . . .	119
6.2.1	Materials and microcapsule preparations . . . . .	119
6.2.2	Optical microscopy imaging and analysis . . . . .	121
6.2.3	Elasticity measurements . . . . .	122
6.2.4	Large-amplitude microcapsule deformation . . . . .	124
6.3	Results and discussion . . . . .	124

6.4	Conclusions . . . . .	138
6.5	References . . . . .	139
<b>7</b>	<b>Conclusions and future work</b>	<b>145</b>
<b>A</b>	<b>Supplementary information for Chapter 2</b>	<b>149</b>



# Chapter 1

## Introduction

Soft matter microstructures can be commonly found throughout most sectors of industrial areas because of their unique rheological properties. Forming self-supported networks in liquid can impart solid-like properties, such as elasticity and yield stress, to the fluids. Contrary to glasses formed by jamming, colloidal gels are formed from suspensions of particles with attractive interactions. The resulting gel structures often have small yield stresses and low viscosities, effectively suspending heavy particles and, at the same time, allowing easy flow in commercial products.

The features of building blocks, like geometry, size and flexibility, are critical for complex fluid design so as to achieve desired rheological responses. Although spheres are the most commonly used particle shape, fibers are increasingly drawing attentions due to their high efficiency in forming gel structures at low concentrations. Microfibrillar cellulose (MFC) produced from bacterial cellulose is characterized by a large particle aspect ratio, high purity, strong mechanical strength, and bio-degradability, suggesting strong potential for application in many industrial areas.

The microstructures formed in fluids are fundamental for their performance. For example, the resistance between particles in jammed structures dissipates the majority of applied stresses, while the interconnected networks play a dominant role in colloidal gels. Also, the poroelastic structures in colloidal gels show a stronger ability for rearrangement than glassy structures that poorly rearrange under ap-

plied stress.<sup>1</sup> Gel structures became increasingly stiff during non-linear deformation, which is also advantageous for applied soft matter applications. For instance, non-linear elastic deformation of cytoskeleton structures allows cell migration without loss of overall structural integrity.

Although the yielding dynamics in condensed suspensions have been extensively reviewed and summarized,<sup>2</sup> the unique yielding behaviours of colloidal gels, especially with highly sparse fiber networks, are still poorly understood. One reason is that the gel structures and the flow dynamics are heterogeneous, which conflicts with the assumption of uniformity made in traditional yielding theory.<sup>3</sup> Much past research studied yielding without considering structure rearrangement prior to yielding, leading to difficulties in explaining the subsequent yielding dynamics in different suspension systems.

This review summarizes recent research studying the yielding dynamics of colloidal gels with highly sparse networks. The poroelastic structures formed by long colloidal fibers provide a unique model network<sup>4,5</sup> and will be the focus of the review. The parameters that control the morphology of gels composed of fiber networks, including size, aspect ratio, flexibility and particle interactions, were firstly explored and linked to different network formations. The yielding dynamics under various conditions, such as different length and time scales, were understood from the perspective of structural changes in three stages: elastic response, non-linear deformation and structure failure. Understanding the formation of fiber networks and relating to the yielding dynamics will enhance our ability to formulate and design complex fluids with novel performance, such as enhanced suspension and surface coating. It is also important in explaining biological functions of cell mobility and muscle contraction, for instance.<sup>6,7</sup>

## 1.1 Parameters controlling gel structures and mechanical strength

Construction of self-supported structures is fundamental to the rheological properties of colloidal gels. Understanding the mechanisms and morphology of different network formation helps explain the unique yielding dynamics. Generally, with increasing particle concentrations, three regimes of dispersions can be generated: dilute suspensions, colloidal gels, and jammed glasses.<sup>8</sup> The particles are disconnected in dilute suspensions and there is no self-supported network formation, while at high concentrations, particles closely pack together, forming jammed microstructures. Contrary to glassy systems, more open microstructures can be formed at semi-dilute concentrations in colloidal gels, but require attractive interactions between particles, Figure 1.1. The properties of particle building blocks, such as size, aspect ratio and flexibility, all affect gelation structure percolation volume fractions.<sup>9,10</sup>

### 1.1.1 Size and aspect ratio

Depending on their sizes, fibers can be Brownian, colloidal or granular. Brownian fibers, such as cellulose nanocrystals, carbon nanotubes and some synthetic polymer fibers,<sup>11-14</sup> have a width and length at the nanoscale, while granular fibers, like wood pulp,<sup>15,16</sup> have both dimensions larger than 1  $\mu\text{m}$ . The resulting aspect ratio for Brownian and granular fibers is less than 500. Colloidal fibers are characterized by a nanoscale width but a microscale length, yielding an aspect ratio larger than 1000, and a great example is bacterial cellulose fibers.<sup>17-20</sup> Nanometer wide fibers have the properties of Brownian particles, such as limited light scattering and extensive surface interactions, while a length on the micrometer scale yields large ex-

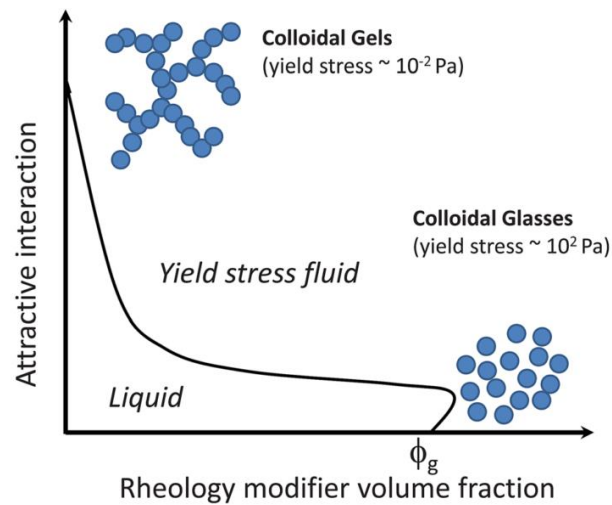


**Figure 1.1:** Colloidal glasses were formed by jamming particles at high volume fractions, and the resulting fluids are highly viscous with large yield stress. Increasing the attractive interactions between particles can generate colloidal gels at low volume fractions, imparting small yield stress to fluids without significantly modifying viscosity. Image reproduced from<sup>22</sup>

cluded volume, significantly preventing particle overlap.<sup>21</sup> Arrested structures can then be formed at lower volume fractions by colloidal fibers due to effective use of available volume.<sup>10</sup>

High aspect ratio particles can form colloidal gels at low volume fractions because of large excluded volume, which is defined as the spatial volume around particles that constrain overlapping of particles.<sup>23</sup> Figure 1.2a qualitatively shows larger excluded volumes with increasing particle aspect ratio, from 1 to over 100, by assuming that the particles share the same volume of around  $4 \mu\text{m}^3$ , based on the theory developed by Balberg *et al.*<sup>9</sup>. The excluded volume could be more than  $1300 \times$  large than the real particle volume at an aspect ratio of 1000, showing the high fiber efficiency. The inter-connected networks are superior when formed from fibers, while the spheres are disconnected at the same volume fractions, Figures 1.2b.1 and 1.2b.2. Exploring the percolation particle density that allows inter-connected

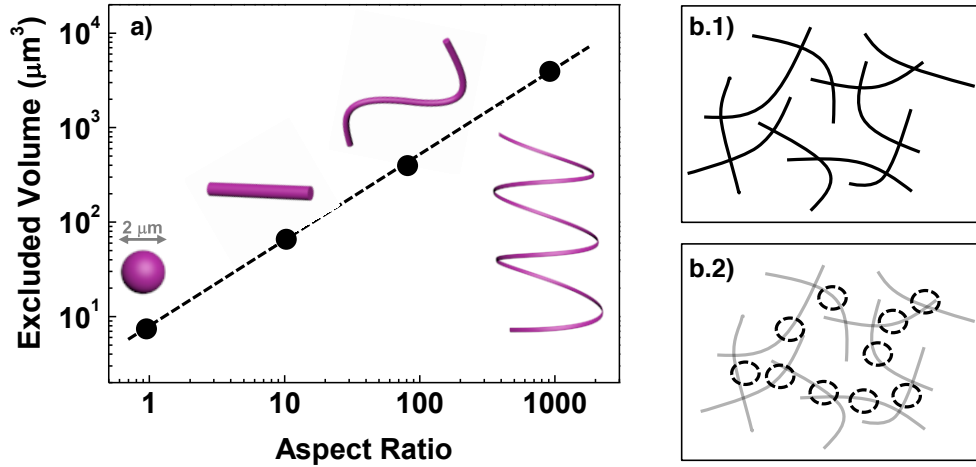


**Figure 1.2:** (a) Assuming that the particles have the same volume of around  $4 \mu\text{m}^3$ , the excluded volume increases when using large aspect ratio particles.<sup>9</sup> The diagrams show long fibers can form an interconnected structure by effective interaction (b.1), while spheres are isolated and cannot form a network at the same particle volume fraction (b.2).

structure formation is highly useful to numerous applications, such as imparting solid-like properties to fluids with minimum usage of materials. Herein, two concepts of percolation threshold,  $\phi_{per}$ , need to be clarified: geometric percolation and rigid percolation, which have different applicable significance.

Geometric percolation refers to the minimum fiber density that can generate a continuous inter-connection.<sup>24</sup> The resulting network may not efficiently support its structure on a global scale. Electrical percolation is a type of geometric percolation, which only requires continuous interconnections for conductivity.<sup>25,26</sup> Nevertheless, rigid percolation requires the formed structure to be self-supported.<sup>24</sup> Some experimental methods, like gravitational gel collapse and dynamic light scattering, are often performed to explore the threshold of rigid percolation.<sup>27,28</sup>

Assuming particles only interact mechanically and the structure is homogeneous, the geometric percolation threshold can be predicted by  $\phi_{per} \sim 1/r$ , here  $r$  is the particle aspect ratio.<sup>10,29</sup> The constant was found to be around 0.7 for geometric

percolation,<sup>30</sup> while the value for stiff percolation was found around seven times higher,<sup>31</sup> which is only slightly smaller than the maximum packing limit.<sup>32</sup> Therefore, we conclude purely entangled fibers form percolation structures at lower volume fractions with increasing particle aspect ratio, but the elastic gelling threshold is approaching to the boundary of the glass regime, showing the small contribution of mechanical entanglements in forming poroelastic gels.

The presence of attractive interactions between particles can significantly lower percolation threshold. The geometric percolation volume fractions for attractive spheres was  $\sim 3 \times 10^{-5}$ ,<sup>27</sup> while the threshold increased to  $> 0.05$  when forming self-supported networks under gravity,<sup>33</sup> rigid percolation. Also, increasing the particle aspect ratio in attractive suspensions can significantly reduce the percolation threshold as well. Wilkins *et al.*<sup>4</sup> found the transition from dilute suspensions to network structures occurred at lower volume fractions as fiber aspect ratio increased.

However, it is still challenging to precisely predict the percolation volume fractions for large aspect ratio rods. The computational simulations barely agree with the experiments, and the experimental results can vary significantly from different studies. A key reason for the variations is the presence of extensive physical complexity in real rod suspensions. For instance, semi-flexible fibers and large size distributions can significantly lower percolation threshold.<sup>31,34</sup>

Numerical simulations often reveal higher percolation values than experimental findings because they assume monodisperse fibers with homogeneous structures.<sup>24</sup> The formation of cluster-like heterogeneous networks can arrest particle dynamics at lower volume fractions.<sup>30,35,36</sup> Vigolo *et al.*<sup>26</sup> found increasing the adhesion energy between fibers by just  $0.006KT$  can reduce their percolation threshold by 300% because heterogeneous fractal structures form. Future studies exploring

## 1.1. Parameters controlling gel structures and mechanical strength

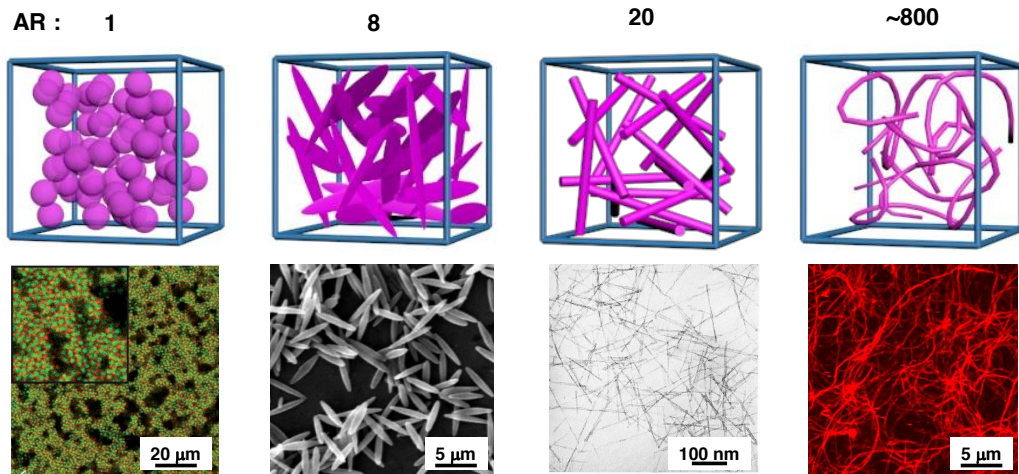


**Figure 1.3:** By selectively using particles with a large aspect ratio (AR), more sparse networks can be formed at lower volume fractions. The top row is the schematic drawing of structures, and the bottom row is images of real gel structures formed by the particles with comparable aspect ratio to the first row: (left to right) silica<sup>37</sup>, PMMA ellipsoids<sup>38</sup>, boehmite<sup>39</sup>, and bacterial cellulose fibers<sup>8,40</sup>.

percolation volume fraction of fiber networks need to account for different particle features, interaction strength between particles, and structural heterogeneity.

The possible gel structures formed by particles with different aspect ratio are illustrated in Figure 1.3. The first row is a schematic diagram, below which the corresponding gel structures with similar particle aspect ratios from literature are shown.<sup>8,37-40</sup> It can be observed how long fibers build more sparse networks at lower volume fractions. Also, semi-flexible fibers largely increase the number of effective contacts, resulting in higher network strength, when compared to spheres and short rods at the same mass concentrations.<sup>21,41,42</sup> For instance, the elasticity of fiber networks increased by more than a factor of 100 when the length of F-actin increased from 0.4 to 5 μm.<sup>43</sup> Large aspect ratio fibers can then build networks at lower volume fractions, reducing material usage but achieving similar rheological performance.

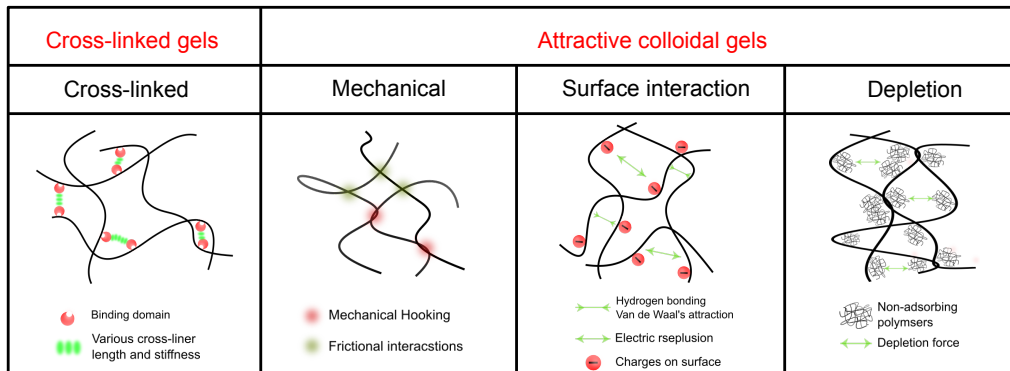


**Figure 1.4:** Illustration of inter-particle forces that enable gel structure formation. The cross-linked gels were formed in the presence of cross-linkers, while attractive colloidal gels can be built by mechanical entanglement and hooking, surface interactions, and depletion attraction.

### 1.1.2 Particle interactions

Interactions between fibers are necessary for making useful gel structures at low concentrations. Based on the interaction types, fiber structures can be separated into two categories: cross-linked gels and colloidal gels, Figure 1.4. Cross-linked fiber networks are formed when chemical bonds connect fibers by “pin joint”, “rotational joint” or “welded joint”. The types of cross-links were determined and clarified by the fiber properties and cross-linkers as well.<sup>44</sup> Some long-chain polymers usually cross-linked and gelled by chemical bonds. Actin fibers get cross-linked and form elastic networks in the presence of actin-binding proteins.

The morphology and mechanical responses of cross-linked structures are strongly correlated to the types and concentrations of cross-linkers.<sup>45,46</sup> Different microstructures were mapped by Lieleg et al.<sup>45</sup> in the presence of various cross-linkers and concentrations. Picu<sup>44</sup> reviewed and summarized the transmission of force and movement through these joints and the mechanics of networks formed by these cross-links. It was reported that the mechanical responses were governed by the degree of cross-linkers rather than individual fibers.<sup>46</sup> Two elasticity regimes were

## 1.1. Parameters controlling gel structures and mechanical strength

---

found at different cross-linker concentrations, and stiffening strain reduced during transition from bending- to stretching-dominated deformation at increased cross-linker concentrations.<sup>19</sup> Yielding of cross-linked fiber networks often occurs at small strain, and the yield strain only slightly reduced with increasing fiber and cross-linker concentrations.

However, in colloidal suspensions, interactions between fibers are mainly generated by mechanical entanglements, caused by the constraint of spatial volume,<sup>47</sup> and surface interactions, including hydrogen bonding, van der Waals attractions, and electrostatic repulsion, Figure 1.4. High aspect ratio fibers can entangle and hook mechanically,<sup>48</sup> and the friction between fibers is essential to form entangled networks<sup>49,50</sup>. Adding surfactant or polyelectrolytes into dispersions can reduce frictional forces and lower gel strength<sup>51</sup>. The orientation of fibers is also important in entangled structure formation. Randomly orientated fibers result in a large number of effective contacts, and the distribution of contacts is uniform.<sup>52</sup> Strong alignments between fibers reduces the degree of effective interactions and forms a weaker gel.

Colloidal forces, based on Derjaguin-Landau-Verwey-Overbeek (DLVO) theory, govern the structure formation of gels composed of fibers. The colloidal stability of fiber suspensions strongly depends on the balance between attractive forces and repulsive contributions. The attractive interactions are essential for building gel structures, but can also lead to disastrous aggregation and flocculation,<sup>34</sup> depending on its significance. Electrostatic repulsion, on the other hand, prevents fiber aggregation, resulting in more uniform dispersion but potentially lowering gel elasticity. For example, natural wood pulp fibers strongly agglomerate in water suspensions due to low zeta potential, while modified fibers with more surface charges form more uniform dispersions.<sup>53</sup> Suppressing or extending electrical double layers

by controlling pH or ion concentration can effectively alter microstructure formation and gel strength.

Introducing surfactant and polymers into fiber suspensions can also create some non-DLVO interactions. For instance, the adsorption of polymers onto fiber surfaces can introduce more charges and increase electrostatic repulsion to prevent flocculation,<sup>54</sup> while non-adsorbing polymers generate depletion forces, enhancing aggregation<sup>55</sup>.

### 1.1.3 Flexibility

The flexibility of fibers can affect the mechanical responses of the networks. Rigid rods, like cellulose nanocrystals, and single-wall carbon nanotubes, cannot bend or elongate, though they freely rotate in dilute suspensions. The elasticity of gel networks formed by rigid rods then only results from inter-particle bonds. By contrast, semi-flexible fibers can bend and stretch at the cost of external energy, as often occurs in many bio-materials and synthetic polymer fibers.<sup>56</sup> The deformation of individual semi-flexible fibers is as important as inter-particle bonds in the mechanical response of networks. Also, the non-linear elastic responses of fiber networks occur at larger strains when using semi-flexible fibers, compared to rigid fibers that show structural stiffening at a few percent strain.<sup>57</sup>

Generally, semi-flexible fibers have a low resistance to bending but become highly stiff when stretched. Bending and self-folding of fibers were both observed under shearing or confinement.<sup>58,59</sup> The persistence length of semi-flexible fibers is larger than its original length, allowing extensive stretching and dissipating high stresses.<sup>41,56</sup> Selecting fibers with high tensile strength, such as bacterial cellulose instead of pulp cellulose,<sup>60</sup> can increase the strength of the networks produced.<sup>61</sup>

## 1.1. Parameters controlling gel structures and mechanical strength

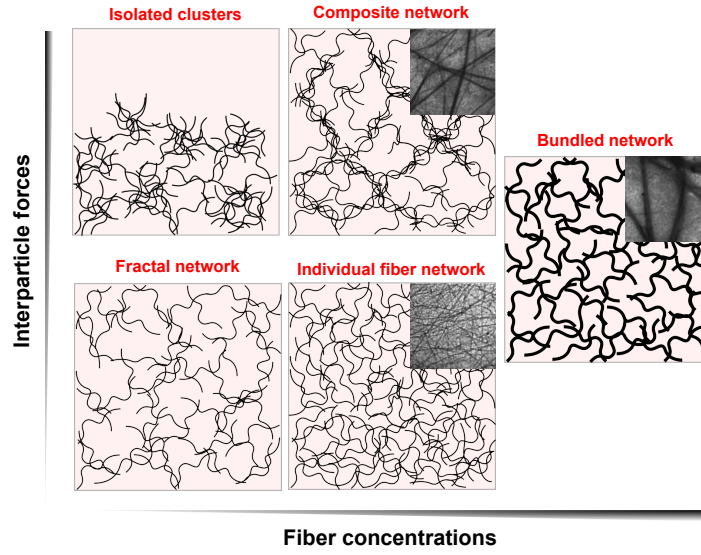


**Figure 1.5:** The morphology of fiber structure is strongly associated with concentration and inter-particle strength. Increasing fiber concentrations results in more homogeneous structures, while the increased attractive forces between particles increase heterogeneity, forming large isolated clusters or a composite network. The insets are the real microscopic images of fiber structures formed by F-Actin.<sup>55</sup>

Complex deformation and yielding properties in the structure of semi-flexible fiber networks will be discussed in more detail later.

### 1.1.4 Structural heterogeneity

Heterogeneity of gel structures is strongly related to their elastic and plastic deformation. The morphology of semi-flexible fiber networks is mainly affected by fiber concentration and interparticle forces.<sup>8</sup> The degree of particle interactions can be quantified by  $U_{contact}/\kappa_B T$ , where  $U_{contact}$  represents pair potential energy, and  $\kappa_B T$  is the thermal energy. When  $U_{contact}/\kappa_B T \ll 1$ , or  $U_{contact}/\kappa_B T \gg 1$ , isotropic networks can be formed at high particle concentrations. Most modelling of mechanics of fiber networks assumes isotropic networks.<sup>57</sup> However, at low particle concentrations, gel structures are normally heterogeneous. The formation of gel structures at low concentrations requires the value of  $U_{contact}/\kappa_B T$  is near or

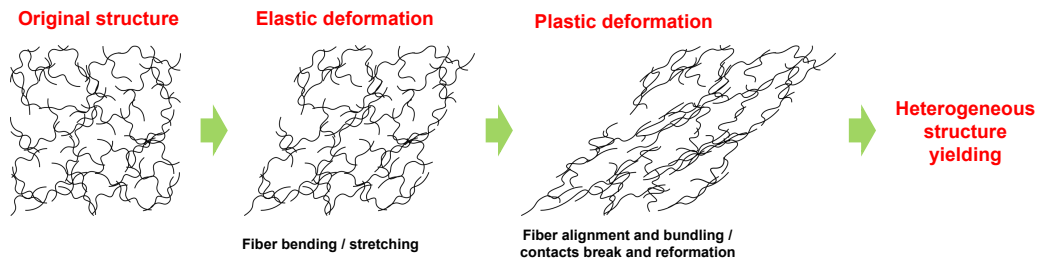
slightly higher than unity. Heterogeneous fiber structures are commonly encountered in commercial suspensions.

Figure 1.5 maps the potential structural morphology formed by semi-flexible long fibers, as a function of concentration and interparticle forces. It can be observed that when the attractive interaction is low, the fibers form clusters,<sup>30</sup> building heterogeneous networks at low solid concentrations. As concentration increases, the structure becomes more homogeneous, although fibers can bundle significantly at high concentrations.<sup>4</sup> Increasing the attractive interactions can induce more heterogeneous structure formation. The highly attractive fibers can aggregate significantly, breaking inter-connected gel structure and forming isolated clusters at low concentrations. A composite network, with bundled and individual fibers, will be created at higher concentrations under higher attractive interactions.<sup>4,55</sup> Some typical structures formed by actin fibers under various depletion forces are shown and compared in Figure 1.5 insets.

The deformation and yielding of heterogeneous fiber networks are non-uniform and difficult to computationally model.<sup>6</sup> Recent studies found the structural heterogeneity can be magnified and have a strong effect on final yielding behaviours, when the network is deformed at relatively low strain rates.<sup>40,62</sup> The bulk strength of a network is the combined function of inter-particle forces and the overall number of contacts.<sup>34,39,55</sup> Controlling the interactions between fibers to produce a well-dispersed suspension, but preserving a cohesive gel structure, is highly desirable for practical applications.

## **1.2 Relating gel microstructure to yielding dynamics**

The formation of microstructures in fluids results in viscoelastic properties where the fluids behave as solids under small applied stress but flow like liquids if the



**Figure 1.6:** The yielding dynamics of fiber networks in three stages: elastic deformation under a small strain where fibers bend and stretch, followed by the plastic deformation region that induces non-reversible restructuring, and eventually structure yielding.

applied stress yields the network. As seen from Figure 1.6, gel structures experience three stages when applied stress is increased gradually: linear elastic response at the beginning, followed by a strain-stiffening or plastic deformation, and eventually structure breakage when the stress exceeds the gel yield stress.<sup>63</sup>

Hooke's law describes an ideal elastic behaviour of gel structures where the deformation of materials is proportional to the applied stress, and the structures recover when the external stress is removed. Soft materials with poroelastic structures are prominent in experiencing a plastic region, in which the structures become highly stiff, and the stress-strain behaviour diverges from linearity. A large non-linear elastic region in the yielding of soft matter is a result of network restructuring, which is advantageous to dissipate large external strain or stress. For instance, non-linear elastic deformation of cytoskeleton structures allows cell migration through constraints but still maintains overall integrity. Consequently, if the structural rearrangement can no longer be accommodated by the continuum gel networks without rupturing inter-particle bonds, the structures will yield, and the materials flows.

However, past work found the yielding of sparse fiber networks diverges from conventional bulk yielding theories that assume continuous homogeneous structure.<sup>22,62,64</sup> The yielding occurring at small length scales can be significantly dif-

ferent from bulk dynamics, and the strained fiber networks at various deformation rates reveal different strength values.<sup>65,66</sup> The rheological responses of colloidal gels with highly sparse networks should this be interpreted from a theory that fully accounts for the microstructure perspective, such as two-fluid description<sup>67</sup>. The rest of this chapter will focus on the responses of sparse gel structures at different stages related to the unique yielding phenomenon.

### 1.2.1 Linear elastic deformation

Elasticity directly indicates the effective interactions in a gel that can dissipate stress. The frequency dependence of the gel storage modulus,  $G'$ , indicates the formation of arrested gel structures in a fluid. Only the particles that interact with at least three neighbours can be immobilized, contributing to the rigidity and elasticity of gel structures.<sup>68</sup> A power-law function for the increased elasticity with particle volume fraction is applicable for sphere, clay, and rod systems,  $G' \sim V^n$  where  $V$  is particle volume fraction and  $n$  is the power-law exponent, consistent with both simulation and experimental results.<sup>40</sup> At low concentrations, long fibers are more favourable in creating effective contacts and forming elastic gel structures. For instance, the gels formed by long fibers, such as microfibrillar cellulose, show frequency dependency of  $G'$  at concentrations as low as 0.01 wt.%,<sup>40</sup> while the  $G'$  increased with increasing frequency in low concentration suspensions of short fibers like cellulose nano-whiskers.

The strain response increased linearly with stress during elastic deformation, but the contributions differ in diverse fiber structures, such as cross-linked versus aggregated gels composed of fibers. In cross-linked networks, increasing fiber stiffness and concentrations cause the elastic deformation mode to transfer from fiber bending to stretching,<sup>69</sup> and the increase of  $G'$  with increasing fiber concentration

is more dramatic<sup>19</sup>. The elastic deformation in cross-linked fiber networks is fully reversible and only occurs at low strains, on the order of 5%.<sup>46,69</sup> However, for the gel structures formed by attractive interactions and aggregation of fibers, the viscoelastic modulus has a weak dependence on the frequency,<sup>70</sup> indicating considerable viscous components and easily restructuring character. Also, deformed attractive gel structures have low reversibility,<sup>69</sup> suggesting inter-particle bonds are partially rearranged, and the restructuring is not necessary for plasticity.

The attractive interactions between fibers are temporal and can slide and reform during deformation.<sup>71</sup> Applied strain can bend individual fibers, such as carbon nanotubes,<sup>58</sup> and at the same time adjust interactive points.<sup>71</sup> Strain-induced bonds break and reform in aggregated fiber networks, leading to alignment and densification.<sup>69</sup> Slight increases in of elastic modulus occur during increasing frequency deformation as a result of structural rearrangement.<sup>72</sup>

In addition to the interaction types, the elastic deformation mechanism is also determined by fiber concentration.<sup>5</sup> Microstructural and dynamical transitions can be explored with increasing fiber concentrations, from porous to glassy networks.<sup>4</sup> In sparse fiber networks formed at low concentrations, the elasticity mainly originates from bending of single fibers, known as non-affine deformation.<sup>11,73</sup> The additional source of the non-affine deformation to sparse fiber networks is significant structural rearrangement,<sup>74</sup> resulting in heterogeneous networks that are unique in dissipating local stresses. However, in more compact networks stretching dominates the elasticity, and the networks experience affine deformation.<sup>5</sup> Highly packed networks can only be slightly rearranged and will rupture at a smaller strain.<sup>11,19,75</sup>

## 1.2.2 Non-linear plasticity and restructuring

After elastic deformation, the continuous increase of applied stress transitions the gels to a plastic region, in which the stress-strain behavior is non-linear. The non-linear deformation of fiber networks is a result of irreversible restructuring.<sup>76</sup> In a cross-linked fiber network, for example, if the structural deformation goes above a critical strain, 5% to 30%, small-scale movement of particles appears to unbind cross-linkers, and the structure can not recover fully.<sup>19</sup> The critical strain, at the onset of gel plasticity, is independent of fiber concentrations in cross-linked structures.<sup>77</sup> However, the sparse fiber networks formed by attractive interactions yield a larger non-linear deformation strain, up to 100%, at low fiber concentrations because of significant spatial rearrangement.<sup>19</sup> The critical strain can be strongly governed by the connectivity of networks in attractive gels composed of fibers.<sup>77</sup>

As known in stress-resistance networks, the coordination numbers should be at least three, and the structure will yield if its functionality loses all connections. In attractive gels composed of fibers, the applied stress can break fiber-fiber connections, but at the same time, the fibers can potentially re-interact with other neighbours and form new contacts, which is negligible in cross-linked networks. Therefore, the non-linear responses of attractive gels are complex results of fiber bending, stretching, contacts sliding and new contacts re-building.<sup>71</sup>

Depending on the initial network strength, the fiber structures can become more soft or stiff during the plastic deformation. In weak gels, high applied strain can directly break fiber contacts, and soften networks. However, in relatively strong fiber networks, a large applied strain can align fibers, which rapidly increases the strength of networks, causing strain-stiffening. For instance, the highest storage modulus of fiber networks was found at the largest stiffening strain just before net-

work yielding.<sup>19</sup> Because of the origin of heterogeneity in fiber networks, the non-linear deformation has a broad microscopic distribution. Rearrangement of microstructure in the different microenvironment can further enhance this non-linear deformation.<sup>78</sup>

Some observations in experiments directly indicate restructuring at stiffening regions in attractive gels composed of sparse fiber networks. The appearance of negative normal force is a typical indicator of structural rearrangement.<sup>79</sup> The magnitude of negative normal forces increased with increasing strain,<sup>80</sup> and the resulting elastic modulus increased linearly with normal force<sup>77</sup> when the networks become stiffening. It was also found that the storage modulus in the non-linear regime was weakly dependent on fiber concentrations. Instead, the applied strains actually govern the mechanics of the networks,<sup>77,81,82</sup> which emphasizes sparse fiber networks are highly responsive to the loaded stress, providing a possibility to explain the high efficiency of fiber networks in particle suspensions<sup>22</sup>.

Herein, it also should be noted that the non-linear responses of fiber networks are sensitive to the measurement conditions and fiber features.<sup>83</sup> The measured elasticity of fiber networks is strain-rate dependent.<sup>66,68</sup> Also, high temperature increase the dynamics of fibers and reduces the stiffening effects so that the transition to strain-softening behaviour at high strains can be observed at extreme conditions. Shortening fiber length can also significantly soften network strength under applied strains. By increasing the numbers of effective contacts per fiber to six, a shifting from strain-softening to strain-stiffening networks can be induced.<sup>83,84</sup>

### 1.2.3 Heterogeneous fiber network yielding

When the applied stress cannot be fully dissipated by elastic deformations, the gel structures starts rupturing, and the gels flow as a consequence. Conventional rhe-

ology studies the yielding of gels on scales much larger than particle size, which is useful in industrial processing such as mixing and pumping. Classical yielding theory assumes continuum flow and averages flow properties over a large measurement geometry, working well in condensed glasses with relatively uniform structures. However, the yielding of the gels with sparse fiber networks is highly heterogeneous, resulting from both structural origins and pre-stressed network deformation.<sup>78</sup>

Microstructural heterogeneity of fiber networks results in non-uniform velocity profiles during bulk flow.<sup>65</sup> The shear stress responses are heterogeneous and have a broad distribution over a large measurement scale when yielding a gel with space-filling microstructures. Boundary stress microscopy enables direct observations of local heterogeneous microstructures and non-uniform rheological responses in colloidal gels.<sup>78</sup> Studies on the yielding of gels composed of fibers need to take structural heterogeneity into consideration, which is fundamental to explain yielding over a range of length and time scales.

### **Yielding on bulk scales**

Although bulk rheology has been developed and explored for many years, it is still challenging to study the yielding of colloidal gels with sparse fiber networks. Strong heterogeneity commonly appears during yielding. For example, step increases of strain can lead to irreversible structure changes before yielding starts. Similarly, shear banding can occur even at relatively high shear rates,  $> 10 \text{ s}^{-1}$ , increasing the difficulty of obtaining a full flow curve. In a more developed flow, the rupturing of interparticle connections is also accompanied by the re-formation of voids and aggregates along the principal axes of flow.<sup>85</sup> The determination of gel bulk yield

## 1.2. Relating gel microstructure to yielding dynamics

---

stress is also difficult, and the results can vary dramatically depending on experimental methods and even operators.<sup>70,83</sup>

The static yield stress refers to the stress threshold that just ruptures the gel, which is often determined by a creep test that exposes the sample to step increased stresses and recording its the responses. Oscillation stress sweeps provide an additional approach for measuring static yield stress, in which the sample is oscillated under increased stress, and the oscillation stress at the onset of  $G'$  reduction is comparable to the gel static yield stress. In these studies, the gel structure was strained in advance, and the pre-stresses applied on the network are critical to its static yielding dynamics.

As we discussed above, applied low strains can either weaken or strengthen fiber networks in different conditions. Therefore, a strain-softening network would yield at smaller stress than a strain-stiffening network, though their original microstructure strength is similar. Also, the non-linear deformation of attractive gels with sparse fiber networks is strain-rate dependent, so the yield stress determination could strongly depend on deformation rates, which will be discussed in the next section.

In another situation, steady-state flow, the gels were sheared at a series of increased or reduced deformation rates in a bulk geometry. At high shear rates, the flow is relatively homogeneous. Fibers stretched and aligned in the direction of applied shear with increasing shear rates, and their shear stress decreased, showing shear-thinning properties. However, as shear rates are reduced, the flow starts becoming more heterogeneous, where fibers can aggregate significantly. Also, the applied shear at low rates is not imposed uniformly over the measuring geometry, which means the shear localizes in a small region with high local shear rate, while the remaining part of the fluid behaves like a solid, known as shear banding.<sup>86,87</sup> The shear rate, below which particles strongly aggregate, is defined as the critical

shear rate.<sup>88</sup> When the applied shear rates are lower than the critical rate, some microstructures can quickly build up under shearing by forming large clusters and aggregates, and the stress response increases accordingly. In this case, it would be difficult to measure whole flow curves,<sup>89</sup> especially for colloidal gels of fibers because of the high possibility of restructuring at low shear rates. Developing a unique yield stress model, which takes structure and flow of fluids into consideration, can successfully predict full flow curves with a similar shape to experimental results.<sup>87,89</sup>

Compared to shearing, uniaxial yielding shows higher mechanical strength in attractive gels composed of fibers.<sup>90</sup> It was reported that the majority of bonds in a gel would be compressed, while equal numbers of connections will be stretched and compressed under shear. An applied compressive stress can significantly align and bundle fibers as well as increasing the number of contacts due to reduced volume fraction during compression. The maximum compressive strain can reach 96% before yielding.<sup>91,92</sup> Therefore, uniaxial yielding of networks is expected to be more heterogeneous due to strong fiber bundling and interaction reformation.

Although heterogeneous yielding dynamics were observed, it is difficult to quantify and model this heterogeneity and its effects on non-linear rheology. A critical step towards solving this problem is to develop a robust theory that predicts and separates the dynamics of dispersed and continuous phases subjected to an external flow. The local responses of structures under shearing or extension can be probed using microrheology, and the dynamics of particles directly imaged under a microscope. Therefore, studying the microscale yielding of fiber networks is necessary, to examine the fundamental microstructural changes and interpret bulk yielding behaviours. Such insights can help explain some yielding phenomena occurring at the small scale, such as suspending micro-sized particles.

### **Yielding in micro scales**

Microrheology uses small tracers to probe the rheology of fluids at a length scale comparable to particle size, allowing exploration of local yielding in heterogeneous systems.<sup>93</sup> The viscoelasticity of fluids can be directly reflected by the motion of tracers, and the stress-induced microstructural deformation can be connected to the rheological behaviours locally.<sup>94</sup> For instance, the non-linear elasticity and unique yielding in space filling gels were successfully correlated to microstructure deformation like fiber alignment and densification, by direct confocal imaging.<sup>62</sup>

Based on probe environment, microrheology techniques can be separated into two classes:<sup>95</sup> passive microrheology relying on thermal fluctuation,<sup>96,97</sup> and active microrheology, using magnetic and optical tweezers<sup>98,99</sup> to manually generate a driving force on probes. The selection of microrheology probes, including sizes and surface properties, is critical for the measurements.<sup>93,100</sup> Tracking multiple particles can quantify the heterogeneity of networks in a large area.<sup>20,97,101</sup>

In a heterogeneous gel structure, both strain-softening and strain-hardening are able to occur during the microrheology measurements in different microenvironments.<sup>78,83</sup> The microrheological properties can vary significantly over small measuring scales. For example, the elastic modulus of F-actin solutions varied by a factor of 2 to 3 in the same sample at different positions.<sup>102</sup> Composite heterogeneous fiber networks show more uniform micro yielding behaviours at a small length scale than fractal bundled networks.<sup>6</sup>

The largest micro stress generated from probes, which can yield the networks, is defined as the gel micro yield stress. The values of micro yield stress in a heterogeneous fluid can vary significantly for different microenvironments, not only due to heterogeneity but also network rearrangement before yielding. Contrary to

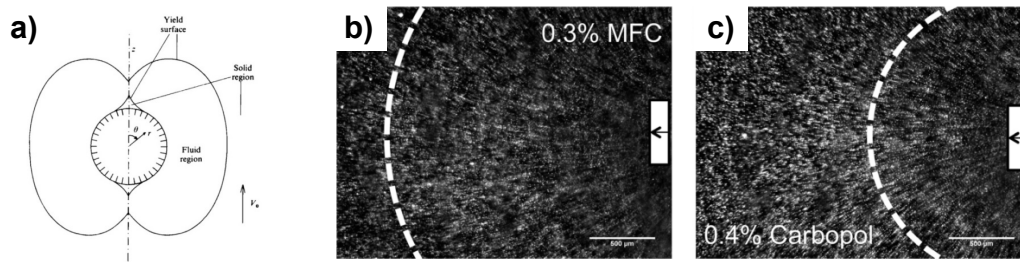


**Figure 1.7:** (a) The yielded area around a probe particle was simulated in a yield stress fluid.<sup>104</sup> (b-c) The sparse fiber network shows a larger yielded area than a jammed glass of carbopol.<sup>22</sup>

macrorheological measurements which produce pure shear, the probes used for microrheology generate both shear and compression onto networks.<sup>103</sup> Since compression often reveals higher network strength than shearing, the magnitude of micro yield stress is expected to be higher than the gel bulk yield stress. For example, the micro yield stress of Laponite gels, performed by magnetic tweezers, were higher than purely sheared bulk yield stress, though the microrheology technique was calibrated with a bulk rheometer before measuring.<sup>64</sup>

When the stress applied from a probe exceeds the micro yield stress, the gel network will yield. Contrary to bulk yielding there is a fluid layer around a probe, which needs to flow with the probe when yielding occurs microscopically, Figure 1.7a.<sup>104</sup> The large yielded area helps dissipate stress exerted on the structure, and the micro yield stress of fluids can easily be underestimated if assuming the yielding area is the same as the probe size.<sup>40</sup> Therefore, the shape and size of the yielded regions around a probe can dramatically affect the micro yielding behaviours.

Cluster-like microstructures in the gels composed of fibers have anomalous shapes of yielded area, contrary to homogeneous string-like microstructures or jammed networks which have more regular and symmetric yielding shapes.<sup>105</sup> Increasing the structural heterogeneity by adding a depletion agent can alter the yielding area around a probe for instance.<sup>105</sup> Also, the size of the yielded area in micro yielding

was found to be larger in heterogeneous fiber networks than in jammed homogeneous networks of spheres, Figures 1.7b and 1.7c.<sup>22</sup> Tensed and compressed fibers can amplify the micro stress into a large scale, and the large scale transmission of micro force shows increased deformation area, especially in highly disordered fiber structures.<sup>106,106</sup> In the more developed flow after yielding, the velocity of tracers fluctuated, again indicating heterogeneity of fiber networks.<sup>40,102</sup>

Herein, we conclude that the inconsistency of microrheology results with bulk rheology can potentially result from local structure heterogeneity, extra yielded surface area, and more significant structural rearrangement. The bulk rheology measurements performed on heterogeneous microstructural fluids may not effectively reflect the real yielding behaviours due to different local micro-flows.<sup>107</sup> Assessing the yielding of structured fluids, especially with highly sparse and heterogeneous networks, in both micro and bulk scales helps reinforce understanding.

### **Rate-dependent yielding**

The structural changes in colloidal gels, either for spheres<sup>85,108,109</sup> or rods<sup>38,110</sup>, are strongly shear rate-dependent because the high porosity of the networks at low particle concentrations enables particles to rearrange. Low deformation rates could induce significant restructuring and densification, which was directly imaged during experiments.<sup>62,85</sup> Compared to the cross-linked networks that reveal similar strain ramp results over two decades of strain rates, attractive gels are more sensitive to deformation rates since the rheological results only agree at high strain rates.<sup>70</sup> The restructuring occurring at low rates is usually irreversible, or takes a long time to fully recover, because of different structural deformation ability, contrary to reversible elastic responses at high rates. In the gels composed of fibers, the elastic response at high deformation rates are initiated by fiber bending and stretching,

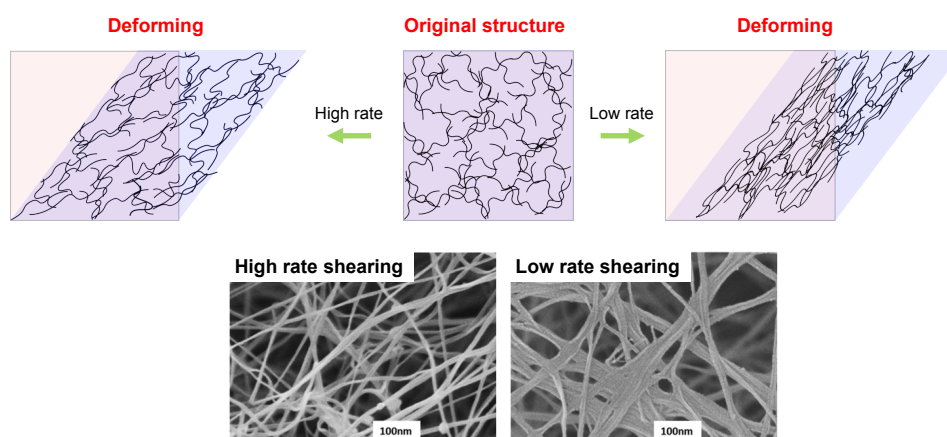


**Figure 1.8:** Illustration of fiber network deformation at high and low rates. A more dense fiber structure can be created by draining solvent out at low rates. The two SEM images show the formation of dense and thick fibers under low deformation rates, compared to high rate deformations.<sup>66</sup>

while fiber alignment and buckling are more favourable at low rate yielding.<sup>74</sup> The gel structures undergo both fast elastic response and stress relaxation at low deformation rates. The stress relaxation is easily achieved by interparticle bond movement and reformation in aggregated space filling gels.

In addition to particle re-organization, solvent permeation throughout poro-elastic structures can also occur at low deformation rates in gels with space-filling networks. For instance, partially squeezing the background fluids out of fiber networks, which is strain rate-dependent, leads to non-recoverable restructured networks with higher mechanical strength.<sup>66</sup> In this case, the colloidal gels of fibers could be treated as two components, elastic compressive fiber networks permeated by a non-compressible solvent as a continuous phase. The viscoelasticity of gels composed of fibers results from both fiber and solvent responses at low frequency, which was quantitatively modelled by two-fluid theory.<sup>111,112</sup> As seen from Figure 1.8, the model describes a continuous deformation or flow at high rates because the high pressure generated from the continuous phase forces dispersed particles to

## 1.2. Relating gel microstructure to yielding dynamics

---

flow with them at the same velocity. However, at low rates when the elastic force balances viscous drag, the solvent starts to drain out of elastic networks, and the flow should be treated as two-phase. The critical frequency, below which the drainage occurs in a gel, can be predicted by  $\omega_c \approx G' \xi^2 / \eta a^2$ , where  $G'$  is network elasticity,  $\xi$  is mesh size,  $\eta$  is solvent viscosity, and  $a$  is the diameter of measuring geometry.<sup>113</sup> When the solvent flows out of elastic networks at low rates, the structures will be compressed and strengthened due to particle densification.<sup>66,114,115</sup> For example, the microstructure of bacterial cellulose hydrogel was deformed permanently when the shear rate is smaller than  $0.33 \mu\text{m/s}$ , resulting in the formation of thick cellulose fibers and higher elasticity at low shear rates, Figure 1.8.<sup>66</sup>

It was also found that the drainage of water around the probe could enlarge the mechanical response area, over which external stress was stored and dissipate. Chen *et al.*<sup>116</sup> found the mechanical layer was enlarged twice around the probe due to the drainage of fluids throughout of the elastic structure. Over a large scale, strain rate-dependent yielding is non-uniform in the gels with heterogeneous microstructures. As mentioned above, the more open networks can be easily deformed and densified at low rates, while the relatively concentrated networks are less compressive due to increased elasticity and reduced permeability. Therefore, when yielding a heterogeneous fiber network at low rates, the local areas with relatively sparse and weak structures will be deformed more significantly than in other dense and strong regions. The strength of highly rearranged regions will increase more dramatically, and the weakness of networks will be eliminated, eventually resulting in more homogeneous structures with the best performance in dissipating external stress at initial low volume fractions.

### 1.3 Project aims and overview

The literature review shows that large aspect ratio fibers are highly efficient in modifying fluid rheology because of their high effective volume fraction. Compared to spherical particles, fibers are able to form gel structures at much lower concentrations, saving material usage in commercial applications. Microfibrillar cellulose (MFC) produced from bacterial cellulose are characterized by high purity, large tensile strength, semi-flexibility and large aspect ratio, which is an ideal material for making space filling colloidal gels at low volume fractions and with strong mechanical properties. The resulting yield stress of low concentration sparse gels shows higher suspension ability than gels of spherical particles with the same bulk yield stress, but the mechanism for the unique yielding dynamics is still unclear. Several studies also indicate large discrepancy when exploring the yielding at different length scales and time scales in the gels composed of fibers.

As a result, a key aim of this project is to study the microstructure and yielding mechanics of microfibrillar networks, enabling better design of commercial fluids with novel properties and performance for applications. A range of topics has been investigated and the contents of each chapter are briefly summarized below.

The heterogeneous yielding of sparse fiber networks was examined in Chapter 2. A microbubble was used as a probe to investigate yielding and measure gel suspension stress. A significant discrepancy was found between the gel's bulk and microscale yield stress, explained by variations in the size of the yielded region and local structure rearrangement during yielding. The restructuring of fiber networks induced heterogeneous yielding and flow, which cannot be modeled by traditional continuum models of yielding.

Significant variations were also evident in micro yield stress measurements at different deformation rates. Chapter 3 shows strong strain rate-dependent yielding of fiber networks as a result of structure rearrangement, which was directly imaged and quantified by confocal microscopy. The critical deformation rates, indicating the transition to restructuring regimes, agree well with the two-fluid model predictions for different MFC concentrations. The results suggest that a two-fluid interpretation can effectively model some aspects of the suspension during sparse network yielding.

The performance of low concentration space filling gels in the suspension of heavy particles was studied in Chapter 4. Accelerated gel collapse dynamics was studied using controlled particle loads to increase gravitational stress, shorten characteristic collapse times and predict shelf-life in commercial suspensions. Contrary to past work on gels of spherical particles, fiber structure can strongly rearrange in response to local gravitational stresses. Two regimes are identified during gel collapse, and can be differentiated using the particle-scale yield stress measured by bubble rheometry.

Chapter 5 explored another application of MFC in surface coating processes, such as nasal spray and irrigation. The low viscosity of MFC gels allows easy flow and spray under applied shear stress, and a quick recovery of networks prevents run-off when the shear was removed. The formation of liquid films by MFC gels was found to be superior to traditional excipients like hydroxy-propyl methylcellulose (HPMC), in both film thickness and retention time.

The design of fiber networks was also extended to the interfacial engineering of microfiber production by bacteria in Chapter 6. Emulsion templated growth of MFC microcapsules yielded controlled geometry and adjustable shapes. The highly porous structures were characterized by three-dimensional confocal imaging

and particle tracking, indicating a 30  $\mu\text{m}$  thick membrane with large pore sizes of more than 0.5  $\mu\text{m}$ . The mechanical studies of cellulose microcapsules reveal low elasticity and high flexibility, which allows them to dissipate stress and pass through constriction by changing shape without damaging membrane integrity. Poroelastic cellulose microcapsules potentially provide a new approach to encapsulate living organisms and behave as a framework able to mimic cells.

In the last part of the thesis, Chapter 7, the conclusions of the thesis are integrated and some future research directions are proposed. One exciting direction for future researchers is further development of the bubble rheometer concept using a computer-controlled pressure feed to manipulate bubble size and broaden the rheometric utility of the system. The demonstration of engineered MFC production to form microcapsules suggests the viability of their surface modification and functionalization to enable new applications.

## 1.4 References

- [1] H. C. de Cagny, B. E. Vos, M. Vahabi, N. A. Kurniawan, M. Doi, G. H. Koenderink, F. C. MacKintosh, D. Bonn, *Physical review letters* **2016**, *117*, 217802.
- [2] D. Bonn, M. M. Denn, L. Berthier, T. Divoux, S. Manneville, *Reviews of Modern Physics* **2017**, *89*, 035005.
- [3] B. Nazari, V. Kumar, D. W. Bousfield, M. Toivakka, *Journal of Rheology (1978-present)* **2016**, *60*, 1151–1159.
- [4] G. M. Wilkins, P. T. Spicer, M. J. Solomon, *Langmuir* **2009**, *25*, 8951–8959.
- [5] A. R. Wufsus, K. Rana, A. Brown, J. R. Dorgan, M. W. Liberatore, K. B. Neeves, *Biophysical journal* **2015**, *108*, 173–183.
- [6] O. Lieleg, K. M. Schmoller, C. J. Cyron, Y. Luan, W. A. Wall, A. R. Bausch, *Soft Matter* **2009**, *5*, 1796–1803.
- [7] M. Lenz, P. Ronceray, C. Broedersz, *APS Meeting Abstracts*, **2016**.

- 
- [8] M. J. Solomon, P. T. Spicer, *Soft Matter* **2010**, *6*, 1391–1400.
- [9] I. Balberg, C. Anderson, S. Alexander, N. Wagner, *Physical review B* **1984**, *30*, 3933.
- [10] I. Balberg, N. Binenbaum, N. Wagner, *Physical Review Letters* **1984**, *52*, 1465.
- [11] D. A. Head, A. J. Levine, F. MacKintosh, *Physical review letters* **2003**, *91*, 108102.
- [12] L. Hough, M. Islam, P. Janmey, A. Yodh, *Physical review letters* **2004**, *93*, 168102.
- [13] L. Hough, M. Islam, B. Hammouda, A. Yodh, P. Heiney, *Nano letters* **2006**, *6*, 313–317.
- [14] P. Pötschke, T. Fornes, D. Paul, *Polymer* **2002**, *43*, 3247–3255.
- [15] B. Derakhshandeh, D. Vlassopoulos, S. G. Hatzikiriakos, *Rheologica acta* **2012**, *51*, 201–214.
- [16] A. B. Fall, S. B. Lindström, O. Sundman, L. Ödberg, L. Wågberg, *Langmuir* **2011**, *27*, 11332–11338.
- [17] J. Xu, A. Palmer, D. Wirtz, *Macromolecules* **1998**, *31*, 6486–6492.
- [18] O. Lieleg, M. M. Claessens, A. R. Bausch, *Soft Matter* **2010**, *6*, 218–225.
- [19] M. Gardel, J. Shin, F. MacKintosh, L. Mahadevan, P. Matsudaira, D. Weitz, *Science* **2004**, *304*, 1301–1305.
- [20] J. Apgar, Y. , E. Fedorov, M. B. Herwig, S. C. Almo, D. Wirtz, *Biophysical journal* **2000**, *79*, 1095–1106.
- [21] X. Xu, F. Liu, L. Jiang, J. Zhu, D. Haagenson, D. P. Wiesenborn, *ACS applied materials & interfaces* **2013**, *5*, 2999–3009.
- [22] H. Emady, M. Caggioni, P. Spicer, *Journal of Rheology (1978-present)* **2013**, *57*, 1761–1772.
- [23] I. Balberg, C. Anderson, S. Alexander, N. Wagner, *Physical review B* **1984**, *30*, 3933.
- [24] V. Favier, J. Cavaille, G. Canova, S. Shrivastava, *Polymer Engineering & Science* **1997**, *37*, 1732–1739.
- [25] A. V. Kyrlyuk, M. C. Hermant, T. Schilling, B. Klumperman, C. E. Koning, P. Van der Schoot, *Nature nanotechnology* **2011**, *6*, 364–369.
- [26] B. Vigolo, C. Coulon, M. Maugey, C. Zakri, P. Poulin, *Science* **2005**, *309*, 920–923.

## References

---

- [27] S. Manley, L. Cipolletti, V. Trappe, A. Bailey, R. J. Christianson, U. Gasser, V. Prasad, P. Segre, M. Doherty, S. Sankaran *et al.*, *Physical review letters* **2004**, 93, 108302.
- [28] S. Manley, J. Skotheim, L. Mahadevan, D. A. Weitz, *Physical review letters* **2005**, 94, 218302.
- [29] A. Bug, S. Safran, I. Webman, *Physical review letters* **1985**, 54, 1412.
- [30] A. P. Philipse, A. M. Wierenga, *Langmuir* **1998**, 14, 49–54.
- [31] D. Rodney, M. Fivel, R. Dendievel, *Physical review letters* **2005**, 95, 108004.
- [32] A. P. Philipse, *Langmuir* **1996**, 12, 1127–1133.
- [33] R. Harich, T. Blythe, M. Hermes, E. Zaccarelli, A. Sederman, L. F. Gladden, W. Poon, *Soft Matter* **2016**, 12, 4300–4308.
- [34] A. V. Kyrilyuk, P. van der Schoot, *Proceedings of the National Academy of Sciences* **2008**, 105, 8221–8226.
- [35] V. Trappe, P. Sandkühler, *Current opinion in colloid & interface science* **2004**, 8, 494–500.
- [36] T. Schilling, S. Jungblut, M. A. Miller, *Physical review letters* **2007**, 98, 108303.
- [37] D. El Masri, T. Vissers, S. Badaire, J. C. Stiefelhagen, H. R. Vutukuri, P. Helfferich, T. H. Zhang, W. K. Kegel, A. Imhof, A. van Blaaderen, *Soft Matter* **2012**, 8, 6979–6990.
- [38] A. Mohraz, M. J. Solomon, *Langmuir* **2005**, 21, 5298–5306.
- [39] A. Wierenga, A. P. Philipse, H. N. Lekkerkerker, D. V. Boger, *Langmuir* **1998**, 14, 55–65.
- [40] J. Song, M. Caggioni, T. M. Squires, J. F. Gilchrist, S. W. Prescott, P. T. Spicer, *Rheologica Acta* **2019**, 58, 217–229.
- [41] C. Bennington, R. Kerekes, J. Grace, *The Canadian journal of chemical engineering* **1990**, 68, 748–757.
- [42] J. Liu, M. Gardel, K. Kroy, E. Frey, B. D. Hoffman, J. C. Crocker, A. Bausch, D. Weitz, *Physical review letters* **2006**, 96, 118104.
- [43] P. A. Janmey, S. Hvidt, J. Käs, D. Lerche, A. Maggs, E. Sackmann, M. Schliwa, T. P. Stossel, *Journal of Biological Chemistry* **1994**, 269, 32503–32513.
- [44] R. Picu, *Soft Matter* **2011**, 7, 6768–6785.

- 
- [45] O. Lieleg, M. M. Claessens, A. R. Bausch, *Soft Matter* **2010**, *6*, 218–225.
- [46] M. Gardel, F. Nakamura, J. Hartwig, J. C. Crocker, T. Stossel, D. Weitz, *Physical review letters* **2006**, *96*, 088102.
- [47] M. A. Hubbe, O. J. Rojas, *BioResources* **2008**, *3*, 1419–1491.
- [48] A. Sorvari, T. Saarinen, S. Haavisto, J. Salmela, M. Vuoriluoto, J. Seppälä, *Carbohydrate polymers* **2014**, *106*, 283–292.
- [49] C. F. Schmid, D. J. Klingenberg, *Journal of colloid and interface science* **2000**, *226*, 136–144.
- [50] L. H. Switzer, D. J. Klingenberg, *International Journal of Multiphase Flow* **2004**, *30*, 67–87.
- [51] S. Zauscher, D. J. Klingenberg, *Colloids and Surfaces A: Physicochemical and Engineering Aspects* **2001**, *178*, 213–229.
- [52] S. E. Whitney, M. G. Gothard, J. T. Mitchell, M. J. Gidley, *Plant Physiology* **1999**, *121*, 657–664.
- [53] A. Isogai, T. Saito, H. Fukuzumi, *Nanoscale* **2011**, *3*, 71–85.
- [54] L. Wagberg, G. Decher, M. Norgren, T. Lindström, M. Ankerfors, K. Axnäs, *Langmuir* **2008**, *24*, 784–795.
- [55] R. Tharmann, M. Claessens, A. Bausch, *Biophysical journal* **2006**, *90*, 2622–2627.
- [56] W. Liu, L. Jawerth, E. Sparks, M. R. Falvo, R. Hantgan, R. Superfine, S. Lord, M. Guthold, *Science* **2006**, *313*, 634–634.
- [57] C. Storm, J. J. Pastore, F. C. MacKintosh, T. C. Lubensky, P. A. Janmey, *Nature* **2005**, *435*, 191–194.
- [58] P. Quinto-Su, X. Huang, S. Gonzalez-Avila, T. Wu, C. Ohl, *Physical review letters* **2010**, *104*, 014501.
- [59] K. B. Smith, J.-N. Tisserant, S. Assenza, M. Arcari, G. Nyström, R. Mezzenga, *Advanced Science* **2019**, *6*, 1801540.
- [60] A. Nakagaito, S. Iwamoto, H. Yano, *Applied Physics A* **2005**, *80*, 93–97.
- [61] M. Bai, A. R. Missel, A. J. Levine, W. S. Klug, *Acta biomaterialia* **2011**, *7*, 2109–2118.

## References

---

- [62] J. Song, M. Caggioni, T. M. Squires, J. F. Gilchrist, S. W. Prescott, P. T. Spicer, *Rheologica Acta* **2019**, *58*, 231–239.
- [63] E. Chanliaud, M. J. Gidley, *The plant journal* **1999**, *20*, 25–35.
- [64] J. P. Rich, J. Lammerding, G. H. McKinley, P. S. Doyle, *Soft Matter* **2011**, *7*, 9933–9943.
- [65] D. W. de Kort, S. J. Veen, H. Van As, D. Bonn, K. P. Velikov, J. P. van Duynhoven, *Soft matter* **2016**, *12*, 4739–4744.
- [66] P. Lopez-Sanchez, M. Rincon, D. Wang, S. Brulhart, J. Stokes, M. Gidley, *Biomacromolecules* **2014**, *15*, 2274–2284.
- [67] A. J. Levine, T. Lubensky, *Physical Review E* **2001**, *63*, 041510.
- [68] L. C. Hsiao, R. S. Newman, S. C. Glotzer, M. J. Solomon, *Proceedings of the National Academy of Sciences* **2012**, *109*, 16029–16034.
- [69] D. Vader, A. Kabla, D. Weitz, L. Mahadevan, *PloS one* **2009**, *4*, e5902.
- [70] C. P. Broedersz, K. E. Kasza, L. M. Jawerth, S. Münster, D. A. Weitz, F. C. MacKintosh, *Soft Matter* **2010**, *6*, 4120–4127.
- [71] G. Subramanian, C. R. Picu, *Physical Review E* **2011**, *83*, 056120.
- [72] H. Isambert, A. Maggs, *Macromolecules* **1996**, *29*, 1036–1040.
- [73] D. A. Head, F. MacKintosh, A. J. Levine, *Physical Review E* **2003**, *68*, 025101.
- [74] Q. Wen, A. Basu, P. A. Janmey, A. G. Yodh, *Soft matter* **2012**, *8*, 8039–8049.
- [75] D. Head, A. Levine, F. MacKintosh, *Physical Review E* **2003**, *68*, 061907.
- [76] C. P. Broedersz, X. Mao, T. C. Lubensky, F. C. MacKintosh, *Nature Physics* **2011**, *7*, 983–988.
- [77] A. J. Licup, S. Münster, A. Sharma, M. Sheinman, L. M. Jawerth, B. Fabry, D. A. Weitz, F. C. MacKintosh, *Proceedings of the National Academy of Sciences* **2015**, *112*, 9573–9578.
- [78] R. C. Arevalo, P. Kumar, J. S. Urbach, D. L. Blair, *PloS one* **2015**, *10*, e0118021.
- [79] S. M. Hashemnejad, S. Kundu, *Journal of Polymer Science Part B: Polymer Physics* **2016**, *54*, 1767–1775.

- 
- [80] P. A. Janmey, M. E. McCormick, S. Rammensee, J. L. Leight, P. C. Georges, F. C. MacKintosh, *Nature materials* **2007**, *6*, 48–51.
- [81] A. Sharma, A. Licup, K. Jansen, R. Rens, M. Sheinman, G. Koenderink, F. MacKintosh, *Nature Physics* **2016**, *12*, 584.
- [82] H. Kang, Q. Wen, P. A. Janmey, J. X. Tang, E. Conti, F. C. MacKintosh, *The Journal of Physical Chemistry B* **2009**, *113*, 3799–3805.
- [83] C. Semmrich, R. J. Larsen, A. R. Bausch, *Soft Matter* **2008**, *4*, 1675–1680.
- [84] J. Liu, G. Koenderink, K. Kasza, F. MacKintosh, D. Weitz, *Physical review letters* **2007**, *98*, 198304.
- [85] B. Rajaram, A. Mohraz, *Soft Matter* **2010**, *6*, 2246–2259.
- [86] P. Coussot, J. Raynaud, F. Bertrand, P. Moucheront, J. Guilbaud, H. Huynh, S. Jarny, D. Lesueur, *Physical review letters* **2002**, *88*, 218301.
- [87] P. Møller, S. Rodts, M. Michels, D. Bonn, *Physical Review E* **2008**, *77*, 041507.
- [88] N. Huang, G. Ovarlez, F. Bertrand, S. Rodts, P. Coussot, D. Bonn, *Physical review letters* **2005**, *94*, 028301.
- [89] P. C. Møller, J. Mewis, D. Bonn, *Soft matter* **2006**, *2*, 274–283.
- [90] R. Buscall, P. Mills, R. Stewart, D. Sutton, L. White, G. Yates, *Journal of Non-Newtonian Fluid Mechanics* **1987**, *24*, 183–202.
- [91] D. Durville, *Journal of materials science* **2005**, *40*, 5941–5948.
- [92] M. Baudequin, G. Ryschenkow, S. Roux, *The European Physical Journal B-Condensed Matter and Complex Systems* **1999**, *12*, 157–162.
- [93] T. Gisler, D. A. Weitz, *Current opinion in colloid & interface science* **1998**, *3*, 586–592.
- [94] M. Gardel, M. Valentine, J. C. Crocker, A. Bausch, D. Weitz, *Physical review letters* **2003**, *91*, 158302.
- [95] T. A. Waigh, *Reports on Progress in Physics* **2005**, *68*, 685.
- [96] B. Schnurr, F. Gittes, F. MacKintosh, C. Schmidt, *Macromolecules* **1997**, *30*, 7781–7792.
- [97] F. K. Oppong, J. R. de Bruyn, *Journal of non-newtonian fluid mechanics* **2007**, *142*, 104–111.

## References

---

- [98] A. R. Bausch, F. Ziemann, A. A. Boulbitch, K. Jacobson, E. Sackmann, *Biophysical journal* **1998**, 75, 2038–2049.
- [99] S. M. Block, L. S. Goldstein, B. J. Schnapp, *Nature* **1990**, 348, 348.
- [100] M. Valentine, Z. Perlman, M. Gardel, J. Shin, P. Matsudaira, T. Mitchison, D. Weitz, *Biophysical journal* **2004**, 86, 4004–4014.
- [101] M. T. Valentine, P. D. Kaplan, D. Thota, J. C. Crocker, T. Gisler, R. K. Prud'homme, M. Beck, D. A. Weitz, *Physical Review E* **2001**, 64, 061506.
- [102] F. Ziemann, J. Rädler, E. Sackmann, *Biophysical Journal* **1994**, 66, 2210.
- [103] A. J. Levine, T. Lubensky, *Physical review letters* **2000**, 85, 1774.
- [104] A. Beris, J. Tsamopoulos, R. Armstrong, R. Brown, *Journal of Fluid Mechanics* **1985**, 158, 219–244.
- [105] M. H. Lee, E. M. Furst, *Physical Review E* **2008**, 77, 041408.
- [106] P. Ronceray, C. P. Broedersz, M. Lenz, *Proceedings of the National Academy of Sciences* **2016**, 201514208.
- [107] J. C. Crocker, M. T. Valentine, E. R. Weeks, T. Gisler, P. D. Kaplan, A. G. Yodh, D. A. Weitz, *Physical Review Letters* **2000**, 85, 888.
- [108] N. Koumakis, G. Petekidis, *Soft Matter* **2011**, 7, 2456–2470.
- [109] J. Vermant, M. Solomon, *Journal of Physics: Condensed Matter* **2005**, 17, R187.
- [110] D. Mukhija, M. J. Solomon, *Journal of colloid and interface science* **2007**, 314, 98–106.
- [111] F. MacKintosh, C. Schmidt, *Current opinion in colloid & interface science* **1999**, 4, 300–307.
- [112] T. M. Squires, T. G. Mason, *Annual Review of Fluid Mechanics* **2009**, 42, 413.
- [113] F. Gittes, B. Schnurr, P. Olmsted, F. MacKintosh, C. Schmidt, *Physical review letters* **1997**, 79, 3286.
- [114] B. Cohen, W. Lai, V. Mow, *Journal of biomechanical engineering* **1998**, 120, 491–496.
- [115] R. G. De Kretser, D. V. Boger, P. J. Scales, *Rheology Reviews* **2003**, 125–166.
- [116] D. Chen, E. Weeks, J. C. Crocker, M. Islam, R. Verma, J. Gruber, A. Levine, T. C. Lubensky, A. Yodh, *Physical review letters* **2003**, 90, 108301.

## Chapter 2

# Heterogeneity, suspension, and yielding in sparse micro-fibrous cellulose gels: Bubble rheometer studies

## 2.1 Introduction

Yield stress fluids exhibit a unique class of non-Newtonian flow: behaving as a solid below a critical stress, but flowing above it. Often yield stress fluids are highly loaded systems, such as cement<sup>1</sup>, mineral slurries<sup>2</sup> and glassy compressed emulsions<sup>3</sup>, where particles crowd one another and impart a high viscosity to fluids. However, low volume fraction colloidal gels also possess a yield stress when particle interactions are strong and a space-filling network forms.<sup>4</sup> When a low volume fraction gel is made up of highly anisotropic rods or fibers,<sup>5</sup> the viscosity can approach that of the solvent while still retaining a relevant yield stress for applications.

Anisotropic colloidal and granular particles are increasingly applied, beyond traditional uses like paper pulp<sup>6</sup>, as structural reinforcements in solids like carbon nanofiber composites<sup>7</sup> and body armour<sup>8</sup> for example. Liquid consumer product formulations can also use fibers to impart a small yield stress and prevent particle sedimentation.<sup>4,9,10</sup> Dispersions of nanoscale cellulose fibers produced by bacterial fermentation<sup>11</sup> or plant fiber attrition<sup>12</sup> are sustainable, highly pure<sup>11</sup>, materials with a large aspect ratio<sup>13</sup>, and unique mechanical properties<sup>14,15</sup>. Dispersion

---

This chapter originally published as Song, J.; Caggioni, M.; Squires, T. M.; Gilchrist, J. E.; Prescott, S. W. & Spicer, P. T. "Heterogeneity, suspension, and yielding in sparse microfibrillar cellulose gels 1. Bubble rheometer studies" *Rheologica Acta*, **2019**, 58, 217-229

of cellulose nanofibers is fundamental to their application, and methods like enzyme digestion<sup>16</sup>, acid hydrolysis<sup>17–19</sup> and mechanical dispersion<sup>16,20</sup> have been used to distribute and set the material's key length scales. Well-dispersed cellulose nanofibers have a width around 50 nm and submicron lengths, and can form liquid crystalline structures,<sup>21,22</sup> while microfibers have similar widths and micron-scale lengths, with aspect ratios  $\geq 1000$ .<sup>20</sup> Microfiber dispersions typically form sparse colloidal gels with low percolation thresholds<sup>23</sup> that impart a yield stress to fluids.

Yielding of three-dimensional colloidal networks is an active research area because the heterogeneous structures formed during yielding complicate characterization and modeling of the phenomenon.<sup>24</sup> Observations of multistage bulk yielding<sup>25</sup> and shear banding<sup>26</sup> emphasize the need to study yielding at length scales approaching that of the constituent colloids. For example, confocal imaging of spherical systems has identified multiple stages of cluster structure evolution during, and after, yielding.<sup>24,27–30</sup> However, the yielding gels composed of rods and fibers has only recently been studied, and has been shown to exhibit heterogeneities that may be practically advantageous, but are not well-understood.<sup>4,10</sup>

Rich *et al.*<sup>31</sup> found the microscale yield stress of aqueous laponite gels to be much higher than the bulk yield stress, suggesting that local structure rearrangement and reinforcement around magnetic tweezer probes accounted for variable yielding behavior. Emady *et al.*<sup>4</sup> proposed a similar mechanism to explain enhanced suspension of millimetric particles by microfiber dispersions versus highly loaded particle glasses, even at the same bulk fluid yield stress. The observed enhancement is believed to occur because yielded areas in microfiber dispersions can vary in size as a result of rearrangements by the sparse mobile fibers just prior to yielding, but the microstructural details have not been studied in detail.<sup>4</sup>

We study here the microscale flows in microfibrinous cellulose, or MFC, dispersions in the stages before, during, and after yielding. A simple bubble tracer method characterizes small length scale yielding, rather than linear elastic behavior,<sup>32</sup> while tracer particle tracking indicates microstructure changes wrought by the deformation. The work is a new approach to combine rheology and microstructure studies using an air bubble and supports the idea of restructuring in sparse gels as a route to enhanced suspension performance.<sup>4</sup> A better understanding of fiber microstructure and nonlinear rheology at multiple length scales could improve our modeling and practical application design of such gels, enhancing design and performance of novel structured fluids.

## **2.2 Experimental methods**

### **2.2.1 Sample preparation**

Bacterial cellulose samples (Wong Coco, Indonesia) were first rinsed multiple times in deionized water to remove any non-cellulosic contaminants. Dispersions were prepared using coarse mechanical disruption in a laboratory blender (Sunbeam, Australia), followed by 5 minutes homogenization (T18 digital Ultra Turrax homogenizer, IKA). Then 0.5 ml of Kathon (Supelco, USA) preservative was added to 500 mL cellulose dispersions, containing roughly 0.4% w/w cellulose, to prevent bacterial contamination. The solids level of each starting dispersion was determined gravimetrically and subsequent dilution with deionized water was then used to prepare different concentrations.

### **2.2.2 Bulk rheology**

A stress-controlled rheometer (AR-1500 EX, TA instruments, New Castle, DE) with cone and plate geometry (cone diameter 60 mm, angle 2°) was used for all bulk fluid

measures. One of the challenges of using a cone and plate geometry with a dilute aqueous suspension is potential loss of fluid by leakage from the gap. Although we test low concentrations of MFC dispersions, fibers have a large aspect ratio,  $\sim 1000$ , and can form gels there. For all experiments, no fluid leakage was observed during rheology measurements. All measurements were performed at  $25^\circ\text{C}$  and after a 30 s pre-shear and a two minute relaxation period. Elastic modulus,  $G'$ , was obtained from a frequency sweep in the linear viscoelastic regime at a constant stress of  $\sigma = 0.01\text{ Pa}$ , Appendix Figure A.1. Dynamic yield stress was measured using steady flow with a shear rate decreasing from  $1000\text{ s}^{-1}$  to  $1\text{ s}^{-1}$  and by fitting to the Herschel-Bulkley equation:

$$\sigma = \sigma_y + K\dot{\gamma}^n \quad (2.1)$$

where  $\sigma$  is the total fluid stress,  $\sigma_y$  is the yield stress,  $K$  is the consistency factor,  $\dot{\gamma}$  is the shear rate, and  $n$  is the flow index. The flow curves used for Herschel-Bulkley fitting are provided in Appendix Figure A.3. For thixotropic MFC dispersions, the measured shear stress decreases with shear rate until a certain point, after which the stress increases as structure is re-built.<sup>33</sup> Here, all fitting to Equation 2.1 was performed for shear rates above this transition to ensure no flow heterogeneities are present.<sup>34</sup> The gel static yield stress was determined by an oscillatory stress sweep test over a range of  $\sigma = 0.01\text{ Pa}$  to  $10\text{ Pa}$ . The elastic modulus is almost constant at low oscillatory stress, followed by a gradual reduction when the stress increased further, Appendix Figure A.2. The gel static yield stress was then determined as the point of intersection between straight lines drawn through the plateau and decreasing regions.<sup>35</sup>

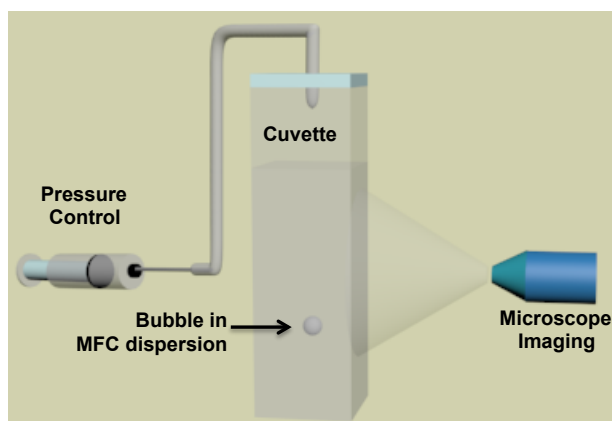


*Figure 2.1: Schematic diagram of bubble rheometer.*

### 2.2.3 Microscale rheology

A bubble-based system was used to study MFC gels, Figure 2.1, varying pressure in a closed sample cell to alter the size of a suspended bubble and apply a controlled amount of force to the fiber network. A volume of 3 mL of MFC gel was placed into the sample cuvette. A small air bubble was generated by syringe injection, from a non-vertical angle to avoid disturbing the bulk fluid, before making an airtight seal of the lid with resin (Araldite). The initially generated small bubbles are stably trapped in the gels, without yielding, though they may pre-stress the networks to a small degree. The bubbles are less than 1/10 the cuvette diameter in order to minimize wall effects. The cuvette headspace was connected to a length of tubing (Tygon, Saint-Gobain) and a syringe (BD) for pressure variation. The bubbles were observed via microscope (Leica WILD M3C, Leica) and recorded by digital imaging (Moticam 10MP, Motic) at two frames per second. The dynamics of bubble size and position were determined by image analysis with ImageJ.<sup>36</sup>

Spherical bubbles provide a more reproducible measure of yielding and stress than anisotropic shapes. We expect gas bubbles to remain spherical in a yield stress fluid if their interfacial tension and hydraulic pressure offset the surrounding fluid

rheology.<sup>38</sup> The low fluid viscosity of MFC gels gives a low capillary number,  $< 5 \times 10^{-8}$ , ensuring the bubbles remain spherical. In more concentrated colloidal glasses, high fluid viscosity can significantly increase capillary number, and distort bubbles from a spherical shape into elongated and twisted forms during expansion and flow.<sup>39</sup> This was used to set an upper limit on the bubble sizes used to characterize a given fluid rheology range, while the minimum measurable bubble size is set by microscopy resolution. Here we only used bubbles with initial diameters from 100 – 200  $\mu\text{m}$ , a length scale much larger than that of the gel mesh size of  $\approx 5\mu\text{m}$ . If the initial bubble size is very small, we may generate excessive extensional compression and flow around the bubble. The bubble rheometer varies stress by controlling pressure in the sealed cuvette. Reduction in pressure increases bubble size and the gravitational force on the bubble, as well as providing a rapid system response. Measurement of instantaneous bubble size then provides a measure of the force it exerts on the fluid. The rate of stress application is controlled by varying headspace pressure, enabling radial bubble growth rates from 0.1 – 6  $\mu\text{m/s}$ . We do observe increased suspension stress for lower expansion rates in the second part of this work, but here focus on high expansion rates where yielding is rate-independent. In this work, all measurements are performed using bubble expansion rates of more than 4  $\mu\text{m/s}$  as we find they provide reproducible and rate-independent measures of yielding.

A fluid is defined to have yielded at the moment the bubble discontinuously begins a steady flow upward. The critical suspension stress,  $\sigma_s$ , is an estimate of yield stress and is defined by the bubble buoyancy force divided by the hemispherical surface area of the bubble size at yielding. Densities used in all calculations are  $\rho_{air} = 1.205 \text{ kg/m}^3$  and  $\rho_{gel} = 1000 \text{ kg/m}^3$ . Local flow around the bubble was tracked using 6  $\mu\text{m}$  tracer particles (Polysciences, USA) stably trapped in the fiber

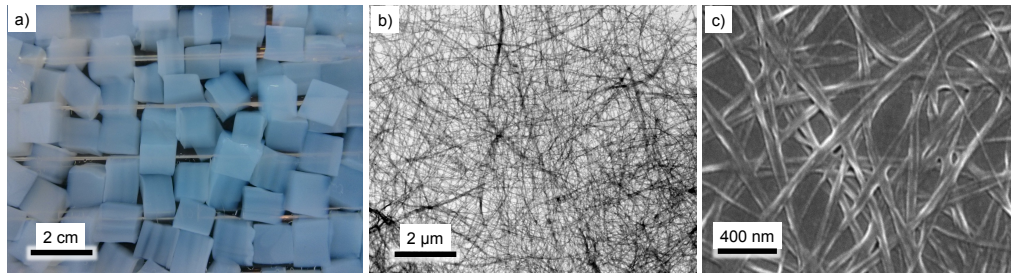


**Figure 2.2:** *The structure of cellulose mats produced by bacterial fermentation is quite robust, forming strong interconnected pellicles that can be cut into cubes that swell in water<sup>37</sup> as seen in (a). Decreasing the scale of observation indicates the large degree of anisotropy of the fibers when studied by cryo-TEM in (b) and by SEM in (c).*

network at a concentration of less than 0.03% w/w. Comparisons with and without tracer particles indicate no measurable effects on fluid rheology at this level.

MFC gels are highly thixotropic and the flow history can strongly affect final yielding behaviour. Multiple measurements on a sample can be performed by re-dispersion with  $\sim 10$  s of sonication, removing effects of past flow<sup>39</sup> without altering fiber properties.

## 2.3 Results and discussion

Imaging of the cellulose fibers enables characterization of the different structures formed and provides an indication of the degree of fiber interaction and packing. Figure 2.2a shows the original aggregated fibers in water, while Figure 2.2b and 2.2c show cryo-TEM and SEM images of fiber structures at increasing magnification levels after dispersal in water. The fibers are several microns in length, but only tens of nanometers in width, indicating an aspect ratio on the order of 1000. The fibers are longer than Brownian nanofibers but thinner than granular fibers, resulting in a very low percolation threshold for the gel network.

The cellulose microfibers are slightly negatively charged but hydrogen bonding and van der Waals attraction can cause bundling in water. High shear homogeni-

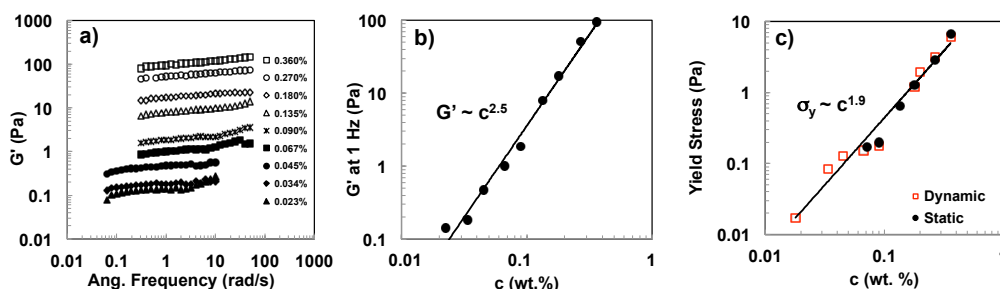


**Figure 2.3:** (a) Determination of dispersion modulus at different concentrations reveals (b) a power-law scaling with fiber content with a fitted exponent of  $2.5 \pm 0.11$ . (c) The bulk yield stress values determined by static and dynamic methods are in good agreement and exhibit power law scaling with concentration<sup>40</sup>.

sation helps disperse the fibers<sup>20</sup> and forms sparse colloidal gels at low volume fraction via agglomeration and entanglement. The elasticity and yield stress of the dispersion is measurable via bulk rheology.

The frequency dependence of the gel elastic modulus,  $G'$ , in the linear viscoelastic regime is an indication of the strength of fiber-fiber interactions.<sup>41</sup> For all systems studied here, the measured  $G'$  exceeds  $G''$  and plots of the moduli with oscillatory frequency have parallel slopes, Appendix Figure A.1. In Figure 2.3a, there is a slight increase in  $G'$  at higher frequencies, possibly as a result of some restructuring within the network. Plotting the plateau value of  $G'$  at  $\omega = 1$  Hz as a function of MFC content in Figure 2.3b shows the modulus scales as a power law with exponent  $2.5 \pm 0.1$ , in agreement with work on fractal gels composed spherical particles with a fractal dimension of  $D_f = 1.8$ <sup>40</sup> as well as carbon nanotubes<sup>7,42</sup>, and collagen<sup>43–46</sup>. Simulations predict a similar scaling exponent of 2.6 for semi-flexible fiber networks.<sup>47</sup>

The bulk yield stress of MFC gels was measured using steady state flow and oscillation stress sweep tests, with raw data shown in Appendix Figures A.2 and A.3. Overall, the yield stress of MFC gels scaled with fiber concentration via a power law with exponent of  $1.9 \pm 0.12$ , Figure 2.3c, lower than the exponent of 2.5–3 found in

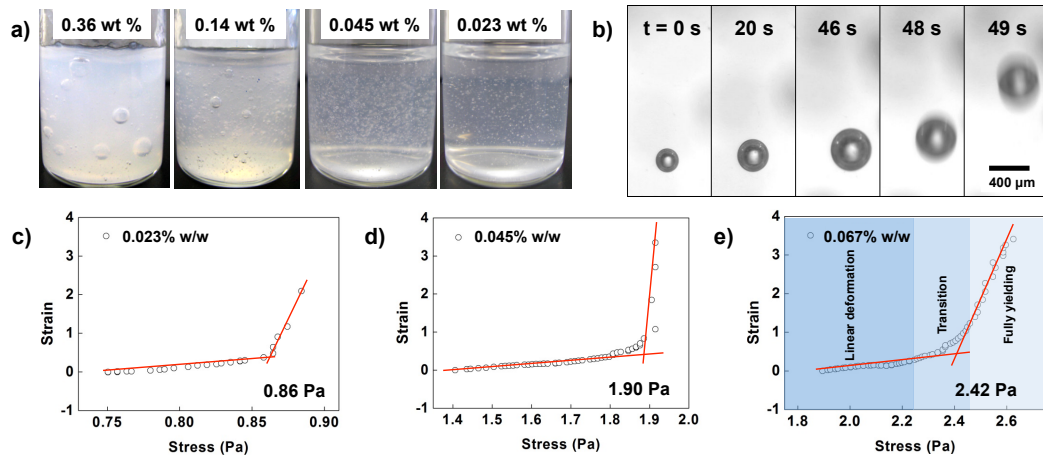


**Figure 2.4:** (a) The relative clarity and suspension ability of various MFC concentrations is evident from images of the air bubbles stably suspended in each case. The characteristic size of the bubbles provides a sensitive assessment of dispersion yield stress since only bubbles small enough to be suspended by the fluid yield stress are still present. (b) A series of images shows the growth of a tracer bubble as the system pressure is reduced and the resultant applied stress increases. Here the bubble grows upward, reflecting its buoyancy, but does not otherwise move until it exerts a strong enough stress to deform the surrounding fiber network. The concentration of fibers is 0.018% w/w. (c-e) Plots of stress and strain show the elastic deformation, linear increase of strain with increasing applied stress, and final yielding events for three fiber concentrations.

studies of granular fiber suspensions,<sup>48–50</sup> but consistent with cellulose nanocrystal suspensions.<sup>42</sup> The power law exponent varies across fiber systems, like wood pulp and collagen<sup>51,52</sup> because of variables like particle aspect ratio, modulus, surface chemistry, and size distribution.<sup>45,53</sup> For example, large aspect ratio particles are more efficient to impart yield stress to fluids<sup>54</sup> and bundled fiber networks, at relatively high concentrations, can form stronger networks than those formed by individual fibers<sup>51</sup>.

Changes in the network elasticity from 0.2 – 100 Pa, as a function of particle concentration, indicate the significant contribution of microstructural elements and interactions to bulk fluid properties, shown in Figure 2.3b. However, bulk rheol-

ogy can not determine microstructural effects on yielding, an important aspect of sedimentation and flow behavior at small length scales.<sup>4</sup>

Figure 2.4a shows suspensions of MFC at different concentrations with trapped bubbles. The size of the maximum stably suspended bubbles increases with increasing fiber concentration. The lack of any observed motion by the stabilized bubbles with time indicates the surrounding gel has a yield stress, rather than simply a high viscosity that would only slow motion. The bubble can thus provide an estimation of the local stress the fluid can withstand before yielding and flowing, suggesting a way to measure the suspension ability of gels as well as investigate local microstructural effects on suspension performance.

Inspired by Figure 2.4a, we use a simple approach to characterize fluid yielding in sparse networks and connect bulk-scale and microscale suspension behavior. A microrheological probe bubble is used to study deformation, yielding, and flow at a microstructural length scale. The method starts by generating bubbles at different sizes and expanding them at a controlled rate to access both the linear and non-linear elastic deformation regions of the surrounding fluid. An example of such an experiment is shown in Figure 2.4b, where an initially stationary bubble grows and slightly moves up, as the system pressure is reduced, until the last frame when it rapidly moves upward out of view: a yielding event. The bubble technique used here allows microrheological studies of sparse gels using a simple experimental setup with a rapid response to an applied pressure field.

Microscale stress and strain during deformation and yielding of MFC networks at 0.023%, 0.045% and 0.067% w/w fibers were studied with the bubble rheometer, Figures 2.4c-2.4e. The bubbles generate both extensional and shear flow during the tests, though shear dominates during yielding. However, for precise analysis, we include both extension,  $\Delta d$ , and shear deformation,  $\Delta x$ , in our reporting of strain

by assuming the two forms are additive:

$$\varepsilon = (\Delta d + \Delta x)/(d_t) \quad (2.2)$$

where  $d_t$  is instantaneous bubble diameter. The critical suspension stress,  $\sigma_s$ , is calculated by dividing the buoyancy force by the hemispherical bubble surface area:

$$\sigma_s = \frac{\frac{4}{3}\pi R^3(\rho_{gel} - \rho_{air})g}{2\pi R^2} = \frac{2(\rho_{gel} - \rho_{air})gR}{3} \quad (2.3)$$

where  $R$  is the bubble radius,  $\rho_{gel}$  is the liquid density,  $\rho_{air}$  is the air density, and  $g$  is the gravitational constant. Fiber networks experienced elastic deformation, as shown by a linear increase in strain with increasing applied stress in Figures 2.4c-2.4e, followed by a transitional stage where deformation becomes non-linear with stress. A sharp increase in strain then indicates the yielding of a network. The three gels in Figures 2.4c-2.4e yield at a similar strain, suggesting a constant yield strain as found in other fiber systems<sup>46,55</sup> and rod polymers. High concentration gels have a larger nonlinear region before fully yielding.<sup>56</sup>

A comparison between the bulk fluid yield stress and the particle-scale gravitational stress can be made with the dimensionless yield stress,  $Y$ :<sup>57</sup>

$$Y = \frac{2\pi R^2 \sigma_y}{\frac{4}{3}\pi R^3 (\rho_p - \rho_l) g} = \frac{1.5\sigma_y}{R(\rho_p - \rho_l) g} \quad (2.4)$$

Beris *et al.*<sup>57</sup> simulated the cessation of homogeneous flow around a particle in a Bingham fluid, finding the transition to arrest occurred at a critical value of  $Y_{crit} = 0.14$ . Sedimentation experiments in different colloidal systems find a range of values for  $Y_{crit} = 0.05 - 0.6$ , because of variations in use of flow cessation versus onset and fluid microstructures.<sup>4</sup>

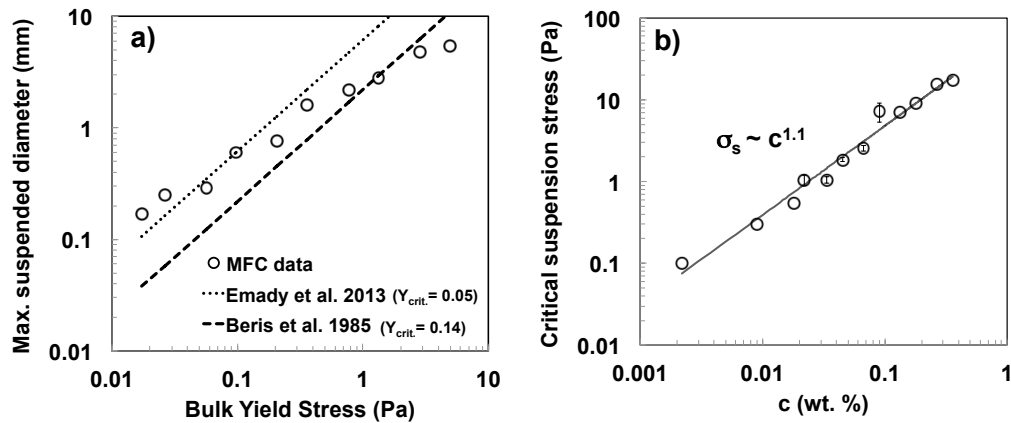


**Figure 2.5:** (a) Maximum bubble diameter that can be suspended in MFC gels at different bulk yield stress. The data shows a good agreement with experimental (dotted line) and simulated data from literature (dashed line). (b) The critical suspension stress, assuming dissipation of stress only over the bubble surface, of MFC gels increases strongly with fiber concentration.

Here we begin with stable, suspended bubbles and then increase their size until the MFC gels yield. The diameter of the largest bubble that the gel can suspend before yielding increases with increasing bulk yield stress, Figure 2.5a. The extreme values of  $Y_{crit}$  determined for an ideal Bingham fluid<sup>57</sup> (dashed line) and a sparse network of MFC fibers<sup>4</sup> (dotted line) are plotted in Figure 2.5a as well. Our microscale data nicely span these two limits, from non-ideal to ideal, as fiber concentration increases. At low concentrations, the suspension ability of MFC gels is more efficient, consistent with previous results for MFC when restructuring seemed to enhance performance.<sup>4</sup> At higher concentrations, more compact networks form and the largest suspended bubble size agrees well with the Bingham prediction.<sup>57</sup> The concentration-dependent suspension efficiency is higher than predicted by the Bingham model at low fiber concentrations, possibly because changes in network microstructure occur.<sup>56</sup> Bulk measurement of yield stress in such systems may significantly deviate from the yield stress experienced at smaller length scales.

Critical suspension stresses,  $\sigma_s$ , of MFC gels were calculated from the measured maximum suspended diameters in Figure 2.5a using Equation 2.3 and are plotted against MFC concentration in Figure 2.5b. Here  $\sigma_s$  scales as a power law with MFC concentration, but is as much as an order of magnitude higher than the bulk yield stress values,  $\sigma_y$ , in Figure 2.3c. Disagreement between microrheology and bulk rheology can occur for a number of reasons, often related to deviations of microstructural behavior from continuum flow expectations.<sup>58</sup> For example, the locally yielded region of fluid around spherical probes can be complex and non-spherical<sup>57,59</sup> and its size determines the stress dissipated by the fluid. Such changes are not significant in bulk rheology measurements, but near the length scale of the colloidal gel building blocks, significant local network heterogeneity could strongly affect flow around small-scale probes. Such rearrangements could account for observed strengthening<sup>4,31</sup> and heterogeneity<sup>26</sup> of gels made from sparse anisotropic colloids and we investigate such effects using visualization of the flows occurring in a sparse fiber network before, during, and after yielding.

Tracer particles added to MFC gels are trapped in the fiber network and allow tracking of the local flow as a bubble is expanded and deforms the fluid. Figure 2.6 shows several close-ups of bubbles expanding within four different MFC gel concentrations, beginning shear elastic deformation of the gel prior to full yielding. The relative position of tracer particles above the bubble indicates the local strain of the network as stress increases, allowing the determination of heterogeneities that arise. In Figure 2.6, the position of three tracer particles, highlighted in white, is shown at different times for each of the four fiber concentrations. The first image is the initial state, with the tracers positioned in gels before expansion begins. The middle image is after expansion has begun, and the last image is the bubble just before yielding. Based on the reduced distance between the tracers with time in

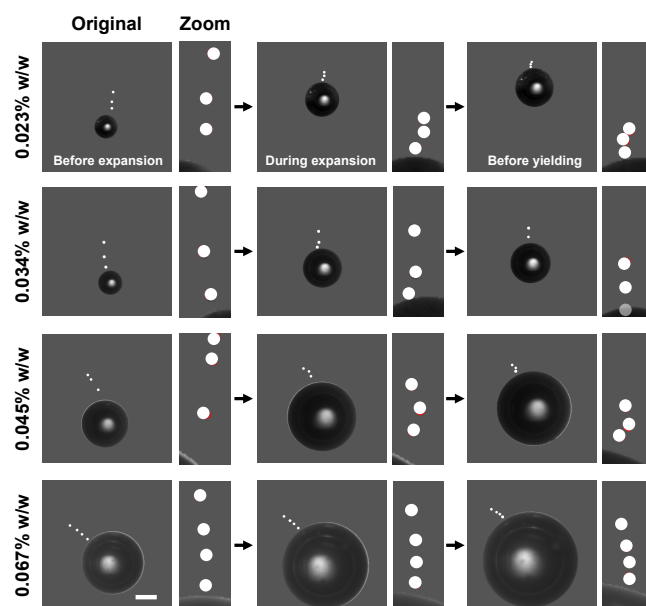


**Figure 2.6:** Multiple frame tracking of preliminary expansion and motion of bubbles prior to yielding, showing reduction in distance between red marked tracers that may indicate localized fiber network compression. The degree of compression before breaking the network reduced as fiber concentrations increased. Scale bar is 200  $\mu\text{m}$ .

each row of Figure 2.6, it appears that microstructural heterogeneities form because of the beginning of bubble motion as stress increases, even before yielding.<sup>60</sup> The stresses generated by bubble expansion can bend, stretch and align fibers above the bubble. Strain-stiffening of networks of spherical<sup>61,62</sup> and fiber<sup>63–66</sup> gels are also known to occur and may be relevant here. The degree of compression before yielding seems to reduce with increasing MFC concentrations, likely because the sparser networks have more space for fiber rearrangement. Highly responsive microstructures can result in locally heterogeneous microscale yielding, and the results in Figure 2.6 are consistent with previous suggested mechanisms for enhanced local fluid mechanical properties.<sup>4,31</sup> Local heterogeneities could even affect flow during yielding of the network, so we use the tracers to visualize yielding onset and the effects of the stress-induced local restructuring indicated by Figure 2.6.

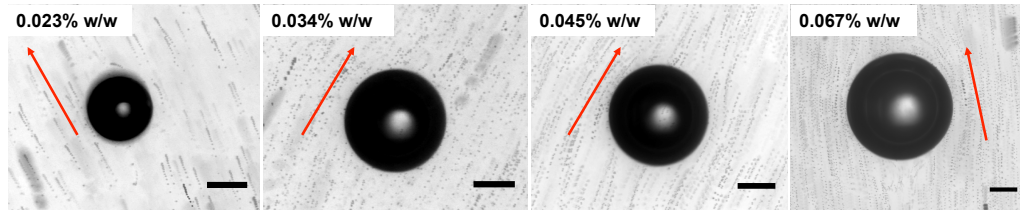


**Figure 2.7:** Visualization of the flow of tracers around a bubble just as yielding begins. Consistent with the previous result, there appears to be an obstruction above the bubble at the beginning of flow as all tracer streaks are angled off the vertical. Scale bar is 200  $\mu\text{m}$ .

By re-centering successive images on the bubble when yielding begins, the flow paths of tracers around the bubble can be used to visualize flow streamlines and the bubble trajectory, Figure 2.7. The buoyant bubbles direct their buoyancy stress upward as pressure is reduced, so the bubbles are expected to move vertically once the fluid yields. Figure 2.7, however, shows that bubbles suspended in four different fiber concentrations all deviate significantly from the vertical in their yielding trajectory. The inability of the bubbles to move straight up for all concentrations studied here indicates locally stronger network formation above the bubbles, consistent with the apparent densification of the network observed in Figure 2.6. Rich *et al.*<sup>31</sup> saw similar trajectory deviations for magnetic colloids suspended in laponite gels. However, in non-restructuring networks, such as aqueous Carbopol, bubbles moved up in a straight vertical trajectory.<sup>39</sup> Apparently, localized densification of the fiber network, before yielding, enhances its strength, allowing it to withstand larger microscale stresses without yielding and requiring the bubble to move off of a vertical trajectory during yielding. This may be why non-restructuring networks, such as jammed colloidal glasses, are less efficient at suspension of particles via yield stress.<sup>4</sup> A higher degree of fiber restructuring at low concentrations provides higher suspension efficiency to sparse gels, which is consistent with our bubble suspension data in Figure 2.5.

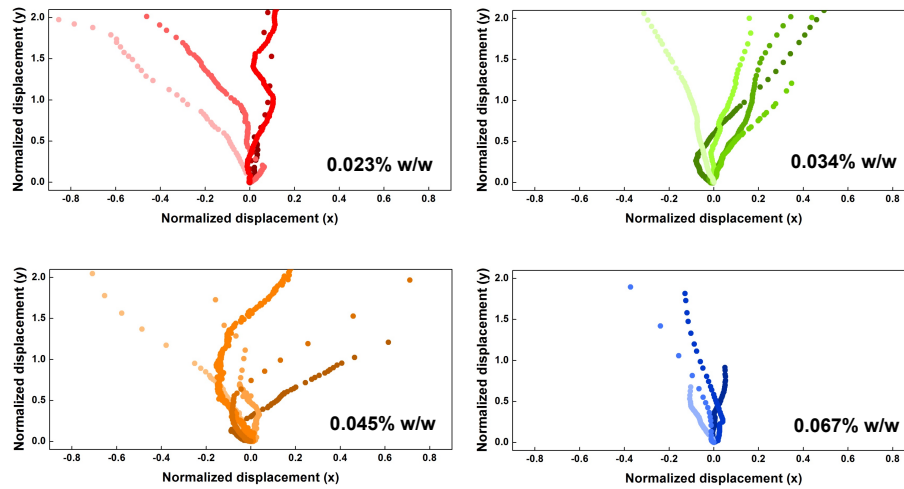


**Figure 2.8:** The continuous yielding of networks was mapped by plotting the bubble trajectory for several experiments. More heterogeneous yielding was found at lower MFC concentrations, but non-vertical yielding trajectories are found over all the concentrations studied here.

Heterogeneous flow behaviour continued long after the network yielded, as observed by longer-term tracking of bubble position through the fluid in Figure 2.8. All concentrations exhibited non-linear bubble trajectories after yielding, but higher concentrations decreased the normalized displacement of the bubble in the x-direction. Again, higher concentrations may present a more homogeneous flow environment for moving particles as compared to the lower concentration gels. Sparser gels have significant space and mobility in which to restructure and increase local fiber density above the average value. Non-Brownian yield stress fluids can potentially preserve such heterogeneities over long times, creating more complex subsequent flows.<sup>39,67,68</sup> All trajectories shown in Figure 2.8 are for the first yield event induced in a sample, preventing effects of previous history on the results. Some pronounced helical trajectories of bubbles are also seen in these results, for example in the 0.023% sample, as a result of heterogeneities in the fiber network. Helical trajectories were also noted in glassy microgel systems, occurring as a result

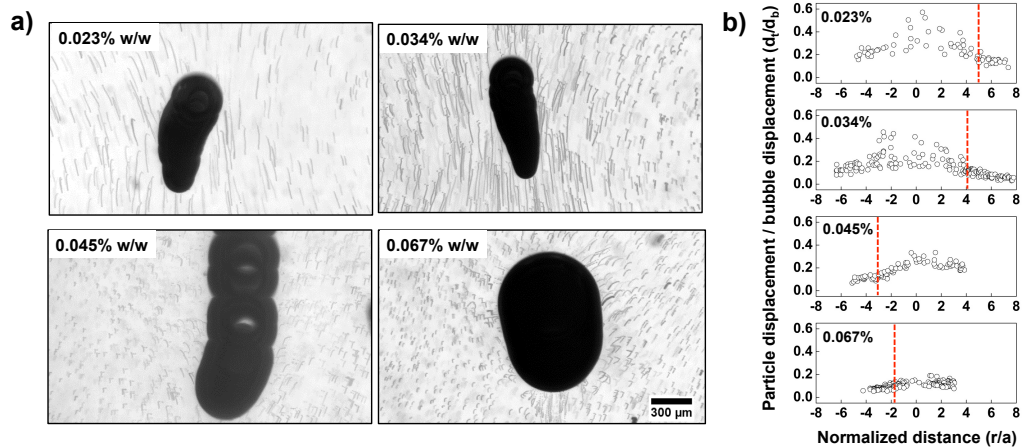


**Figure 2.9:** (a) Composite images of a bubble over a sequence of frames during, and just after, yielding. Bubbles rarely move straight upward from their initial position, likely because of fiber network restructuring and consolidation above the bubble. (b) Plotting the displacement of tracers embedded in the fiber network during the yielding event indicates the size of the region, indicated by red dashed lines, of fluid that must move before steady flow begins. Increasing fiber concentration decreases the size of the yielded region.

of flow instabilities.<sup>39</sup> Attractive fiber networks can clearly develop significant heterogeneity in structure, mechanical properties, yielding, and flow. Further study is needed to connect the fiber results with those for the yielding of spherical colloid networks<sup>24,30,69,70</sup> as well as previous studies of yielding flows around particles<sup>71</sup>.

Apparent structural rearrangement of fiber networks under applied stress locally enhances strength, creates heterogeneous post-yielding flow, and likely affects the size and shape of the local yielded region. More concentrated jammed microstructures are typically homogeneous, so their yielded areas are symmetric with a size relatively independent of particle concentration.<sup>71</sup> Microscale investigations of depletion gels, however, reveal asymmetric deformation fields around microprobes.<sup>69</sup> Much sparser fiber networks could have even more complex yielded areas, so we next attempt to map such heterogeneity effects during yielding.

Tracking tracer particle motion enables us to approximately identify the region of the fluid that moves around the bubble during yielding. Successive images of the tracer particles during a yielding event are shown in Figure 2.9a for different fiber concentrations. The sequences include a single frame after the bubble has moved out of the field of view. The displacement of tracers in the direction of the bubble movement is large nearest the bubble and drops off rapidly moving away from the bubble, indicating the region of influence. Some smaller movement of tracers farther away from the bubble results from small amounts of bulk fluid drift, but are subtracted out of subsequent analyses. Consistent with earlier arguments that low fiber concentrations permit greater restructuring and densification, lower concentrations may also allow greater variations in yielded region size than for denser systems. Noticeable in Figure 2.9a is the two-dimensional asymmetry of the yielded regions, also consistent with the angular bubble trajectory results in Figures 2.7 and 2.8. A number of tracer paths have a pronounced hook shape that indicates an elastic rebound by that fluid region after yielding, similar to observations of microgel glass yielding.<sup>39</sup>

Quantitative assessment of the flows in Figure 2.9b is obtained by plotting the dimensionless ratio of tracer to bubble displacement ( $d_t/d_b$ ) against the normalized distance of tracers from the bubble center ( $r/a$ ). The size of the yielded region can be estimated from the position of tracers where dimensionless displacement levels off, indicated by red dashed lines in Figure 2.9b. Although difficult to quantify given the region's asymmetry, lower MFC concentrations seem to produce larger yielded regions but vary in size with fiber levels. More homogeneous yield stress fluids tend to exhibit yielded regions, with less dependency on dispersion concentration<sup>72</sup> Yielding of glassy Carbopol gels by bubbles or particles only produces a dimensionless yielded region radius of 1.3<sup>39,73</sup> whereas the MFC fibers here vary from 2 to 5

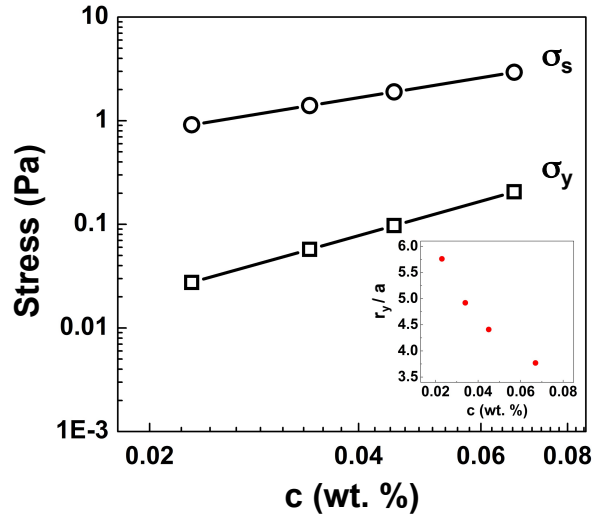


**Figure 2.10:** The microscale yield stress,  $\sigma_s$ , of MFC gels is 30 times the bulk value,  $\sigma_y$ , at 0.023% w/w and is 15 times higher than the most concentrated system at 0.067%. The size of dimensionless yielded radius, calculated by reconciling measurements at the two length scales, decreases with increasing fiber concentration, inset, which is consistent with the yielded regions in Figure 2.9.

in Figure 2.9b. Emady *et al.*<sup>4</sup> also hypothesized variation of yielded region sizes of MFC to explain its anomalous suspension ability, and we can potentially use this information to reconcile the measurements of bulk and microscale yield stress.

Comparison of Figures 2.3 and 2.4 indicates the microscale ( $\sigma_s$ ) and the bulk ( $\sigma_y$ ) yield stress differ by as much as a factor of 30, Figure 2.10. The assumption that yielding occurs only in a thin hemispherical layer at the bubble surface is clearly oversimplified. Back-calculating the yielded area needed for the bulk and microscale stresses to agree provides a second estimate of the radius of the yielded region to compare with Figure 2.9b. The estimated values of yielded radius normalized by initial bubble radius,  $r_y/a$ , decreased from around 5.7 to 3.7 with increasing fiber concentration (Figure 2.10 inset). Comparison with decaying tracer velocity data in Figure 2.9 shows reasonable agreement, given the asymmetry of the yielding trajectory and the lower resolution of tracer velocity at high fiber loadings, but significant

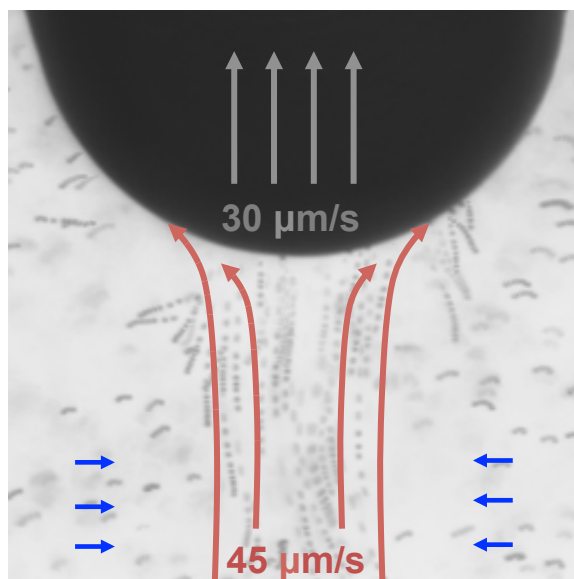


**Figure 2.11:** The total motion of tracers behind a bubble just after yielding of a network, containing 0.067% w/w fibers, using a composite of several image frames. The velocity of these tracers exceeds that of the probe bubble, indicating the separation of aqueous phase from the fiber network can occur during deformation.

uncertainty remains. Reconciliation of the micro and bulk measurements indicates a larger yielded area in sparse networks can effectively increase the suspension efficiency of particles with length scales similar to the fibers. Although a heterogeneous microstructure formed around the bubble prior to yielding, the microscale yield stress measurement might not be significantly affected, as the restructuring is slight and the bubble can escape the strongest areas and yield the non-rearranged network as seen in Figure 2.7. We can not currently quantify how the above measurements are affected by the microstructure compression observed in Figure 2.6, but will examine restructuring effects in Chapter 3. For now, we explore the possibility of two-fluid behavior by this system as a starting point.

The hypothesized densification of the fiber network in Figures 2.7 and 2.8 implies that sparse fiber networks behave as a two-fluid system: an elastic network permeated by a viscous fluid.<sup>74,75</sup> Simple evidence of two-fluid behavior is seen

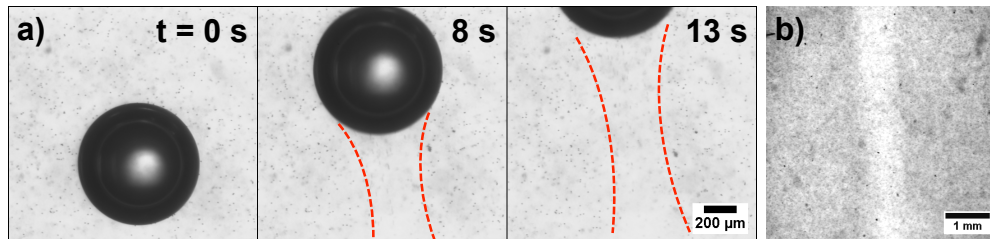


**Figure 2.12:** (a) Microstructure formed by non-Brownian fibers can not be totally recovered after yielding and a scar is left by a bubble after breaking a network of 0.067% w/w MFC. The boundary between flowing and static regions is mapped by red dashed lines. (b) A scar is more obvious at a higher MFC concentration of 0.2% w/w and is reinforced by repeatedly passing bubbles through the scar.

in the flow behind a bubble after yielding in Figure 2.11. Estimating local velocity from tracer flows in Figure 2.11 indicates that tracers following the bubble actually move 50% faster,  $45 \mu\text{m/s}$ , than the bubble itself,  $30 \mu\text{m/s}$ . The discrepancy is perhaps because water has flowed out of the fiber network during deformation and yielding, allowing faster local flow. A second likelihood is that elastic rebound of the surrounding network pushes in toward the region trailing the bubble as it moves upward. Recent bulk rheology studies found negative normal forces and increased elasticity for sheared weak space filling gels, apparently because denser fiber networks formed as fluid was extracted during shear.<sup>76</sup> Better understanding of yielding in sparse systems, incorporating microstructural evolution, is clearly needed to know when such systems can not be treated as homogeneous fluids.

Heterogeneity effects are accentuated in these non-Brownian suspended fiber systems, as the rearranged microstructure can not spontaneously rejuvenate after network yielding. Flow through such a network leaves a “scar”, as we see in Figure 2.12, and without re-dispersion will present a different flow environment for subsequent particles. The retention of such scars increases at higher fiber concentrations, as the network is less likely to rejuvenate. A more visible scar forms in 0.2% MFC gel, seen in Figure 2.12b.

## 2.4 Conclusions

We have studied the yield stress behavior of cellulose microfiber suspensions, near the length scale of the gel building blocks, to better explain past observations of enhanced suspension performance. A simple rheometer, using stress applied by a controlled size bubble, has been used to probe the dynamics of flow and structure leading up to the onset of yielding. Bulk and microscale measurements are compared and the inconsistencies interpreted using study of the local deformation of fiber microstructure. Beyond interpretations of the fluid as a homogeneous system, several observations indicate two-fluid behavior by the fiber suspension. Localized restructuring seems to occur above bubbles prior to yielding, likely as a result of the stress-responsive fiber networks forming locally denser regions. As a result, the bubbles usually depart from vertical trajectories during yielding and flow. Unlike more homogeneous yield stress fluids, the size of the gel's yielded region decreases with increased fiber concentration, another indicator of strong microstructural effects on microscale yielding.

Given the apparent importance of restructuring to sparse network yielding and flow, local deformation rates are expected to play a key role in overall suspension behavior.<sup>26</sup> More study is needed to quantify the nature and rate-dependence of restructuring, as such effects are now known to affect bulk rheological measurements<sup>76,77</sup> as well as simulated phenomena like bond breaking and reformation.<sup>78</sup> Although heterogeneous structures complicate flow and rheology studies, they also offer a clear advantage in efficiency, of material use and performance, for particle suspension in formulated fluids. Further study is needed of how, and when, local network rearrangements occur during deformation in order to understand how such changes affect fiber network yielding. Direct confocal imaging<sup>79</sup> is an option

we explore, in Chapter 3, to better visualise and quantify the structural changes we observed here.

## 2.5 References

- [1] M. Fourmentin, G. Ovarlez, P. Faure, U. Peter, D. Lesueur, D. Daviller, P. Coussot, *Rheologica Acta* **2015**, *54*, 647–656.
- [2] R. Buscall, *Colloids Surf.* **1990**, *43*, 33–53.
- [3] T. Mason, J. Bibette, D. Weitz, *J. Colloid Int. Sci.* **1996**, *179*, 439–448.
- [4] H. Emady, M. Caggioni, P. Spicer, *J. Rheo.* **2013**, *57*, 1761–1772.
- [5] M. J. Solomon, P. T. Spicer, *Soft Matter* **2010**, *6*, 1391–1400.
- [6] M. R. Bhole, L. K. Hui, C. Gomez, C. P. Bennington, G. A. Dumont, *Canad. J. Chem. Eng.* **2011**, *89*, 985–995.
- [7] L. Hough, M. Islam, P. Janmey, A. Yodh, *Phys. Rev. Lett.* **2004**, *93*, 168102.
- [8] R. Egres Jr, M. Decker, C. Halbach, Y. Lee, J. Kirkwood, K. Kirwood, N. Wagner, E. Wetzel, *Stab resistance of shear thickening fluid (STF)-Kevlar composites for body armor applications*, Dtic document technical report, **2004**.
- [9] P. B. Laxton, J. C. Berg, *J. Colloid Int. Sci.* **2005**, *285*, 152–157.
- [10] S. Mirzaagha, R. Pasquino, E. Iuliano, G. D'Avino, F. Zonfrilli, V. Guida, N. Grizzuti, *Physics of Fluids* **2017**, *29*, 093101–9.
- [11] M. Iguchi, S. Yamanaka, A. Budhiono, *J. Mat. Sci.* **2000**, *35*, 261–270.
- [12] M. A. S. Azizi Samir, F. Alloin, A. Dufresne, *Biomacromolecules* **2005**, *6*, 612–626.
- [13] I. Siró, D. Plackett, *Cellulose* **2010**, *17*, 459–494.
- [14] A. Nakagaito, S. Iwamoto, H. Yano, *Applied Physics A* **2005**, *80*, 93–97.
- [15] O. Shezad, S. Khan, T. Khan, J. K. Park, *Carbohydrate Polymers* **2010**, *82*, 173–180.
- [16] M. Pääkkö, M. Ankerfors, H. Kosonen, A. Nykänen, S. Ahola, M. Österberg, J. Ruokolainen, J. Laine, P. T. Larsson, O. Ikkala *et al.*, *Biomacromolecules* **2007**, *8*, 1934–1941.

## References

---

- [17] K.-Y. Lee, F. Quero, J. J. Blaker, C. A. Hill, S. J. Eichhorn, A. Bismarck, *Cellulose* **2011**, *18*, 595–605.
- [18] J. Wu, Y. Zheng, Z. Yang, Q. Cui, Q. Wang, S. Gao, X. Ding, *J. Polymer Res.* **2012**, *19*, 1–8.
- [19] T. Saito, S. Kimura, Y. Nishiyama, A. Isogai, *Biomacromolecules* **2007**, *8*, 2485–2491.
- [20] A. Kuijk, R. Koppert, P. Versluis, G. van Dalen, C. Remijn, J. Hazekamp, J. Nijse, K. P. Velikov, *Langmuir* **2013**, *29*, 14356–14360.
- [21] S. J. Veen, A. Kuijk, P. Versluis, H. Husken, K. P. Velikov, *Langmuir* **2014**, *30*, 13362–13368.
- [22] S. J. Veen, P. Versluis, A. Kuijk, K. P. Velikov, *Soft Matter* **2015**, *11*, 8907–8912.
- [23] I. Balberg, N. Binenbaum, N. Wagner, *Phys. Rev. Lett.* **1984**, *52*, 1465.
- [24] L. C. Hsiao, R. S. Newman, S. C. Glotzer, M. J. Solomon, *Proc. Natl. Acad. Sci.* **2012**, *109*, 16029–16034.
- [25] B. Derakhshandeh, G. Petekidis, S. S. Sabet, W. Y. Hamad, S. G. Hatzikiriakos, *J. Rheo.* **2013**, *57*, 131–148.
- [26] D. de Kort, S. J. Veen, H. van As, D. Bonn, K. P. Velikov, *Soft Matter* **2016**, *12*, 1–10.
- [27] K. Pickrahn, B. Rajaram, A. Mohraz, *Langmuir* **2009**, *26*, 2392–2400.
- [28] B. Rajaram, A. Mohraz, *Soft Matter* **2010**, *6*, 2246–2259.
- [29] H. K. Chan, A. Mohraz, *Phys. Rev. E* **2012**, *85*, 041403.
- [30] H. K. Chan, A. Mohraz, *Rheologica Acta* **2013**, *52*, 383–394.
- [31] J. P. Rich, J. Lammerding, G. H. McKinley, P. S. Doyle, *Soft Matter* **2011**, *7*, 9933–9943.
- [32] A. Jamburidze, M. D. Corato, A. Huerre, V. Garbin, *Soft Matter* **2017**, *13*, 3946–3953.
- [33] C. J. Dimitriou, G. H. McKinley, *Soft Matter* **2014**, *10*, 6619–6644.
- [34] P. Moller, A. Fall, V. Chikkadi, D. Derks, D. Bonn, *Phil. Trans. R. Soc. A* **2009**, *367*, 5139–5155.
- [35] J. A. Yanez, T. Shikata, F. F. Lange, D. S. Pearson, *Journal of the American Ceramic Society* **1996**, *79*, 2917–2917.
- [36] C. A. Schneider, W. S. Rasband, K. W. Eliceiri, *Nat. Meth.* **2012**, *9*, 671–675.

- 
- [37] P. Lopez-Sanchez, M. Rincon, D. Wang, S. Brulhart, J. Stokes, M. Gidley, *Biomacromolecules* **2014**, *15*, 2274–2284.
- [38] N. Dubash, I. Frigaard, *J. Non-Newt. Fluid Mech.* **2007**, *142*, 123–134.
- [39] N. Mougin, A. Magnin, J.-M. Piau, *J. Non-Newt. Fluid Mech.* **2012**, *171*, 42–55.
- [40] R. Sonntag, W. Russel, *J. Colloid Int. Sci.* **1987**, *116*, 485–489.
- [41] H. Wu, M. Morbidelli, *Langmuir* **2001**, *17*, 1030–1036.
- [42] Q. Beuguel, J. R. Tavares, P. J. Carreau, M.-C. Heuzey, *Journal of Rheology* **2018**, *62*, 607–618.
- [43] S. B. Lindström, D. A. Vader, A. Kulachenko, D. A. Weitz, *Phys. Rev. E* **2010**, *82*, 051905.
- [44] A. Sharma, A. Licup, R. Rens, M. Sheinman, K. Jansen, G. Koenderink, F. MacKintosh, *Nat. Phys.* **2016**, *12*, 584–587.
- [45] M. Gardel, J. Shin, F. MacKintosh, L. Mahadevan, P. Matsudaira, D. Weitz, *Science* **2004**, *304*, 1301–1305.
- [46] F. MacKintosh, J. Käs, P. Janmey, *Phys. Rev. Lett.* **1995**, *75*, 4425.
- [47] C. Broedersz, M. Sheinman, F. MacKintosh, *Phys. Rev. Lett.* **2012**, *108*, 078102.
- [48] C. Bennington, R. Kerekes, J. Grace, *Canad. J. Chem. Eng.* **1990**, *68*, 748–757.
- [49] F. Martoša, P. Dumont, L. Orgéas, M. Belgacem, J.-L. Putaux, *Soft matter* **2016**, *12*, 1721–1735.
- [50] M. Mohtaschemi, K. Dimic-Misic, A. Puisto, M. Korhonen, T. Maloney, J. Paltakari, M. J. Alava, *Cellulose* **2014**, *21*, 1305–1312.
- [51] A. V. Kyrilyuk, P. van der Schoot, *Proc. Nat. Acad. Sci.* **2008**, *105*, 8221–8226.
- [52] R. Tharmann, M. Claessens, A. Bausch, *Biophys. J.* **2006**, *90*, 2622–2627.
- [53] P. A. Janmey, S. Hvidt, J. Käs, D. Lerche, A. Maggs, E. Sackmann, M. Schliwa, T. P. Stossel, *J. Bio. Chem.* **1994**, *269*, 32503–32513.
- [54] A. Wierenga, A. P. Philipse, H. N. Lekkerkerker, D. V. Boger, *Langmuir* **1998**, *14*, 55–65.
- [55] P. A. Janmey, S. Hvidt, J. Lamb, T. P. Stossel, *Nature* **1990**, *345*, 89–92.
- [56] B. Gurmessa, R. Fitzpatrick, T. T. Falzone, R. M. Robertson-Anderson, *Macromolecules* **2016**, *49*, 3948–3955.

## References

---

- [57] A. Beris, J. Tsamopoulos, R. Armstrong, R. Brown, *J. Fluid Mech.* **1985**, *158*, 219–244.
- [58] T. M. Squires, *Langmuir* **2008**, *24*, 1147–1159.
- [59] M. Beaulne, E. Mitsoulis, *J. Non-Newt. Fluid Mech.* **1997**, *72*, 55–71.
- [60] X. Zhang, O. Fadoul, E. Lorenceau, P. Coussot, *Physical review letters* **2018**, *120*, 048001.
- [61] J. P. Pantina, E. M. Furst, *Phys. Rev. Lett.* **2005**, *94*, 138301.
- [62] J. Sprakel, S. B. Lindström, T. E. Kodger, D. A. Weitz, *Phys. Rev. Lett.* **2011**, *106*, 248303.
- [63] D. Vader, A. Kabla, D. Weitz, L. Mahadevan, *PloS one* **2009**, *4*, e5902.
- [64] P. Quinto-Su, X. Huang, S. Gonzalez-Avila, T. Wu, C. Ohl, *Phys. Rev. Lett.* **2010**, *104*, 014501.
- [65] G. Žagar, P. R. Onck, E. van der Giessen, *Biophys. J.* **2015**, *108*, 1470–1479.
- [66] J. Feng, H. Levine, X. Mao, L. M. Sander, *Soft matter* **2016**, *12*, 1419–1424.
- [67] M. Hariharaputhiran, R. S. Subramanian, G. A. Campbell, R. P. Chhabra, *J. Non-Newt. Fluid Mech.* **1998**, *79*, 87–97.
- [68] G. Gheissary, B. Van den Brule, *J. Non-Newt. Fluid Mech.* **1996**, *67*, 1–18.
- [69] M. H. Lee, E. M. Furst, *Phys. Rev. E* **2008**, *77*, 041408.
- [70] B. Gueslin, L. Talini, Y. Peysson, *Rheo. Acta* **2009**, *48*, 961–970.
- [71] E. Mitsoulis, *Rheo. Rev.* **2007**, *2007*, 135–178.
- [72] D. Atapattu, R. Chhabra, P. Uhlherr, *J. Non-Newt. Fluid Mech.* **1995**, *59*, 245–265.
- [73] Y. Holenberg, O. M. Lavrenteva, U. Shavit, A. Nir, *Phys. Rev. E* **2012**, *86*, 066301.
- [74] A. J. Levine, T. Lubensky, *Physical Review E* **2001**, *63*, 041510.
- [75] F. Brochard, P. De Gennes, *Macromolecules* **1977**, *10*, 1157–1161.
- [76] H. C. G. D. Cagny, B. E. Vos, M. Vahabi, N. A. Kurniawan, M. Doi, G. H. Koenderink, F. C. Mackintosh, D. Bonn, *Phys. Rev. Lett.* **2016**, *117*, 217802.
- [77] J. Kim, D. Merger, M. Wilhelm, M. E. Helgeson, *J. Rheol.* **2014**, *58*, 1359–1390.
- [78] J. Colombo, E. Del Gado, *J. Rheol.* **2014**, *1089*, 1089–1116.
- [79] A. Mohraz, M. J. Solomon, *Langmuir* **2005**, *21*, 5298–5306.

## Chapter 3

# Heterogeneity, suspension, and yielding in sparse microfibrillar cellulose gels: Strain rate-dependent two-fluid behavior

### 3.1 Introduction

Yield stress fluids can behave as solids under small external applied stress, but as liquids at larger stresses. They are widely used in products like shampoo and toothpaste, yogurt and salad dressing<sup>1</sup>, pharmaceutical nasal sprays<sup>2</sup>, and injectable gels<sup>3</sup>. Highly loaded glassy systems like mineral slurries, compressed emulsions, and swollen polymer gels possess high yield stresses, and high viscosity, due to crowding of non-interacting particles.<sup>4,5</sup> However, colloidal gels can impart low, but useful, yield stresses to fluids at much lower volume fractions by interaction of, for example, anisotropic particles.<sup>6,7</sup>

Bacterial cellulose fibers are advantageous for making low yield stress colloidal gels, and their nanoscale widths and microscale lengths enable a broad range of applications. Cellulose fibers produced by bacterial fermentation have a higher mechanical strength than fibers produced by attrition,<sup>8,9</sup> yet are easily dispersed into microfibrillar cellulose, or MFC. The large aspect ratio of MFC,  $\sim 1000$ , increases

---

This chapter originally published as Song, J.; Caggioni, M.; Squires, T. M.; Gilchrist, J. E.; Prescott, S. W. & Spicer, P. T. "Heterogeneity, suspension, and yielding in sparse microfibrillar cellulose gels 2. Strain rate-dependent two-fluid behavior" *Rheologica Acta*, **2019**, 58, 231-239

the probability of fiber-fiber interaction, while the fibers' slightly negative surface charges prevent alignment and bundle formation, instead forming sparse efficient networks.<sup>10</sup> Sparse MFC networks can suspend valuable particles, without noticeably increasing a fluid's viscosity, and extend the shelf-life of numerous formulated liquid products.

Microstructural differences between yield stress fluids can alter the mesoscopic mechanism of flow resistance, though low volume fraction gels can resemble highly loaded glassy systems when studied by bulk rheology.<sup>11</sup> In jammed glassy systems, the resistance of individual particle deformation and structural reorganization resists flow, while colloidal gels of entangled and bundled fibers form highly reconfigurable mesh networks. Rearrangement of fiber networks under stress, via stretching, bending, aligning and buckling,<sup>12,13</sup> helps dissipate stress and stabilise fluids like cellular cytoplasm.<sup>14–16</sup> The microscale yielding behaviours of sparse fiber networks should then be quite different from denser, jammed systems. For instance, MFC gels can suspend much larger granular particles than jammed microgel composed of spheres, even when both fluids have the same bulk yield stress.<sup>7</sup> Fiber-scale studies of yielding in MFC systems indicate that restructuring of the sparse fiber network plays a key role in enhanced suspension and local yielding.<sup>17</sup>

Continuum yield stress models are unable to explain the aforementioned microstructure-dependent yielding and time-dependency.<sup>18</sup> A "two-fluid" approach is one way to account for differences in the continuous and dispersed phase flow of poroelastic fluid microstructures at low strain rates.<sup>19–24</sup> Two-fluid effects on fiber network rheology have not been widely studied, though recent bulk rheology studies indicate low deformation rates can cause negative normal stresses in collagen fiber dispersions<sup>22</sup> and increase fluid elastic modulus in actin networks<sup>22,25</sup>, but microstructural studies are rare.

In this Chapter, a simple microbubble-based technique<sup>17</sup> is used to study the deformation rate-dependent yielding of MFC gels as a function of fiber concentration. We find the local yield stress of the fiber network varies significantly with deformation rate, greatly enhancing the suspension capacity of the dispersion. Significant increases in yield stress occur for deformation rates below a critical rate that depends on fiber concentration. These observations are consistent with predictions of a two-fluid model, and are further supported by confocal microscopy observations of local restructuring of the local fiber network at low strain rates. Sparse fiber dispersions are a highly responsive fluid matrix with significantly varying fluid mechanical properties, making them valuable for rheology modification of formulated materials and study of the yielding transition in fluids.

## **3.2 Experimental methods**

### **3.2.1 Sample preparation**

Bacterial cellulose samples (Wong Coco, Indonesia) were first rinsed multiple times in deionized water to remove any non-cellulosic contaminants. Dispersions were then prepared using mechanical disruption in a standard laboratory blender (Sunbeam, Australia). Microbiological stability of the samples is ensured by addition of 0.5 mL of Kathon (Supelco, USA) to 500 mL samples. The solids level of every feed stock was determined by gravimetric measurement. Subsequent dilution with deionized water was then used to prepare different fiber concentrations for rheological characterization. All dilutions were then mixed with a T18 digital ULTRA-TURRAX homogenizer, IKA for 5 min to achieve homogenous dispersion before measurement.

### 3.2.2 Fiber imaging

MFC dispersions were first stained by 1 mg/mL Congo Red (Sigma-Aldrich, USA) solution for 15 min, followed by centrifugation at 11,000 g for 10 min. The sediments were then resuspended in 1 mol/L potassium chloride (Univar, Australia) for 10 min to remove any unbound Congo red. Stained cellulose was finally resuspended in deionized water, to produce different concentrations, and homogenized for 10 min. We tested the rheology of MFC gels with and without Congo red addition and did not see any evidence of effects on fiber interactions.

Fiber imaging was performed on a confocal microscope (Leica SP5 WLL gSTED, Germany). A 10× dry objective, with numerical aperture  $NA = 0.3$ , and a 63× oil immersion objective, with  $NA = 1.3$ , were used. Congo Red dye was excited with a  $\lambda_0 = 496$  nm laser beam. All images were taken in regions where the brightness of images is proportional to particle density. The radial intensity and fast Fourier transform (FFT) of images were analysed using ImageJ.<sup>26</sup>

### 3.2.3 Critical suspension stress measurements

A bubble rheometer was developed to study local rheology of MFC gels before, during, and after yielding.<sup>17</sup> A volume of 3 mL of different concentration gels was placed into sample cuvettes with some headspace remaining. The top of the cuvette was connected to Tygon tubing (Saint-Gobain, France) which was then connected to a syringe (BD, Singapore). A bubble was generated in the gel before sealing the lid with epoxy (Araldite, NZ) to make it airtight. The size of the bubble was small compared to the cuvette diameter, to minimize wall effects. Bubble growth was observed by a large working distance stereomicroscope (Leica WILD M3C, Germany) and recorded by a digital camera (Moticam 10MP, Europe) at different time intervals to capture yielding dynamics.

The system controls stress by varying pressure in the sealed cuvettes. Reduction in pressure increases bubble size and the gravitational force on the bubble. Since the bubble responds rapidly to pressure changes, the rate of stress increase is linearly controllable. The response of the bubble enables instantaneous measurement of the force it exerts on the fluid, and its effects on the surrounding structures. The relaxation time of the gels, measured by oscillatory frequency sweep, is on the order of 10 ms and is smaller than the typical rates of expansion used here of  $60 - 5000 \mu\text{m}^2/\text{s}$ .

Experiments were performed only using bubbles that remain spherical throughout the measurement. The critical suspension stress,  $\sigma_s$ , is indicative of the local fluid yield stress and is obtained by calculating the buoyant force on the bubble, then dividing it by the hemispherical surface area of the bubble size at yielding:

$$\sigma_s = \frac{\frac{4}{3}\pi R^3(\rho_{gel} - \rho_{air})g}{2\pi R^2} = \frac{2(\rho_{gel} - \rho_{air})gR}{3} \quad (3.1)$$

where  $R$  is the bubble radius,  $\rho_{gel}$  is the liquid density,  $\rho_{air}$  is the air density and  $g$  is the gravitational constant. Densities used in all calculations are  $\rho_{air} = 1.205 \text{ kg/m}^3$  and  $\rho_{gel} = 1000 \text{ kg/m}^3$ . Our observations indicate yielding occurs as a shearing flow, though the bubble generated small extensional flow in all directions at the beginning of bubble expansion. Since the buoyancy force acts upward and the bubble finally yields and rises, we assume here that the fiber networks around the hemispherical top half of the bubble bear the stress. Yielding was defined as the moment the bubble discontinuously begins a steady flow upward.<sup>17</sup> Errors in measurement of  $\sigma_s$ , on the order of 0.02 Pa, stem from optical resolution limits to bubble size measurement as well as uncertainty over the imaging time intervals used. Some

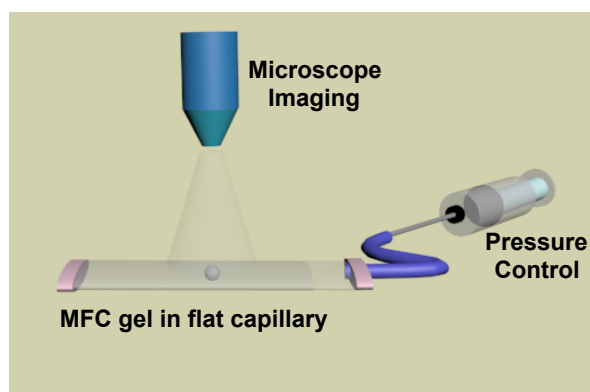


*Figure 3.1: Schematic diagram of horizontal static network deformation.*

variation in the starting bubble diameter and microstructure heterogeneity also contribute to experimental variability.<sup>17</sup>

### 3.2.4 Static structure deformation

Yielding studies are performed using bubbles free to move vertically in the networks,<sup>17</sup> but we also isolate the effects of bubble expansion on the fiber structures prior to yielding. A horizontal sample cell is used for static studies, as it prevents bubbles from rising, but still allows radial expansion and fiber imaging, Figure 3.1. In static experiments, a bubble was generated in a dispersion of Congo Red-stained MFC and transferred into a  $0.2 \times 2$  mm rectangular flat capillary (VitroCom, USA). Epoxy resin was used to seal one end of the flat capillary and connect the other end, via tubing, to a syringe for pressure variation. Fibers were then visualised around bubbles via confocal imaging while bubbles were forced to expand at specific rates. The bubble was found to attach to the inner surface of the capillary, and the bubble diameter is larger than the thickness of the capillary, allowing horizontal bubble expansion without vertical displacement. Also, as the fiber mesh size,  $< 5\mu\text{m}$ , is much smaller than the height of the capillary,  $200\mu\text{m}$ , the regions we study for structural changes are not expected to be affected by confinement.

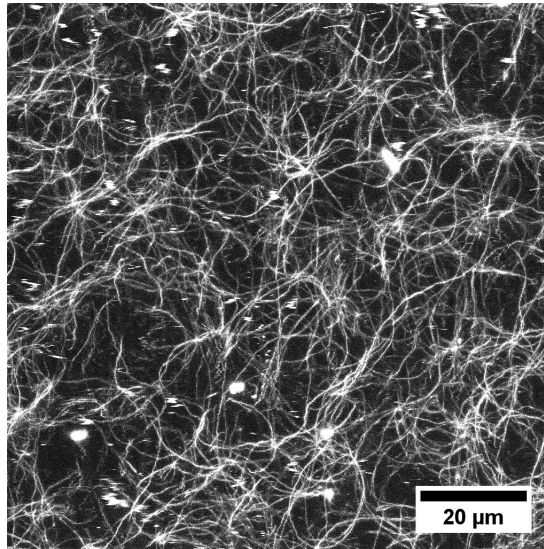


**Figure 3.2:** Confocal microscopy image of a dispersed bacterial cellulose network. MFC was dispersed in water to the concentration of 0.023% and stained by Congo red dye before imaging. Ten images with 400 nm intervals were assembled into this two-dimensional image.

### 3.3 Results and discussion

A confocal image of the bacterial cellulose network, at 0.023% w/w fibers, is shown in Figure 3.2. The fibers are mostly nanoscale in thickness, but micron-scale in length, imparting a significant aspect ratio and connectivity efficiency to the network.<sup>10,27</sup> A time sequence of the growth of bubbles used to characterize fluid yield stress is shown in Figure 3.3 for 0.023% fibers, with small adjustments made to compensate for small motion of the bubble prior to yielding. Two different bubble expansion rates are examined in Figure 3.3 to compare the significance of local deformation rate on the suspension ability of the MFC network. Figure 3.3 shows a time sequence of images comparing two bubbles expanding at a rapid ( $3400 \mu\text{m}^2/\text{s}$ ) and slow rate ( $100 \mu\text{m}^2/\text{s}$ ). The right-hand image in each row shows the final stable bubble size attained just before the suspending network yields. The slower expansion rate produces a maximum stable bubble diameter that is twice the diameter of

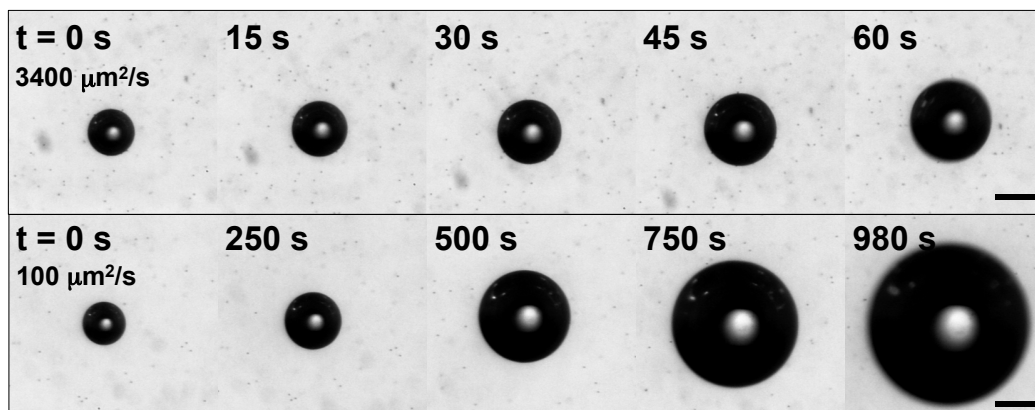


**Figure 3.3:** Time sequences of bubble growth in 0.023% MFC dispersions at fast,  $3400 \mu\text{m}^2/\text{s}$ , and slow,  $100 \mu\text{m}^2/\text{s}$ , expansion rates. The final bubble size represented the largest that the MFC gel can suspend. Scale bar is  $200 \mu\text{m}$ .

the bubble expanded at a larger expansion rate, Figure 3.3. A naive calculation of the stress on each bubble before yielding gives 1.2 Pa for the faster expansion rate and 2.5 Pa for the slower rate, a factor of two difference in suspension ability. Below we investigate the microstructural origins of the observed performance discrepancy to better understand the effects of fluid deformation rate.

The rate-dependent yielding of MFC networks was explored for different fiber concentrations by plotting the  $\sigma_s$  of each fluid as a function of expansion rate in Figure 3.4. Error bars indicate variability of the results due to fiber network heterogeneity and variation in initial bubble diameter. All concentrations exhibit a gradual increase of  $\sigma_s$  as expansion rate decreases, with the effect becoming much stronger at low expansion rates, consistent with Figure 3.3. Below a critical expansion rate, measured values of  $\sigma_s$  are as much as two and half times larger at lower bubble expansion rates for the lowest MFC concentration. The observed enhancement of  $\sigma_s$  is consistent with previous work that found fiber network rearrangement increased shear elastic modulus,  $G'$ , during low-frequency oscillatory deformation.<sup>21,22,25</sup>

From our observations in Chapter 2 and the rate-dependent yielding observed in Figure 3.4, we suggest that MFC colloidal gels behave as a combination of two

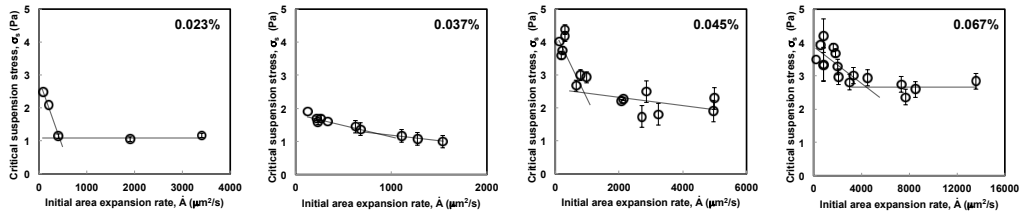


**Figure 3.4:** The critical suspension stress is less rate-dependent at high bubble initial area expansion rates, but increases more dramatically at low rates. The intersection of two best-fit linear regressions for each concentration indicates the transition to locally enhanced fiber networks.

fields: a continuous viscous fluid that permeates an elastic network. Because water is incompressible, the MFC network can only compress if water flows out. Such fluid flow exerts viscous stress on the surrounding network; the faster the relative flow, the higher the stress. At high bubble expansion rates, the gel is carried by the fluid without compressing, and the resulting  $\sigma_s$  is relatively low. At low expansion rates, however, fluid can “drain” through the gel without causing it to yield. The displacement of water allows the elastic fiber network to compress, and therefore increases  $\sigma_s$  at low rates.

We hypothesize that the critical area expansion rate, below which  $\sigma_s$  increases most dramatically, reflects the onset of network rearrangement and a local strengthening of the fiber network. Assuming the existence of such a transition, we arbitrarily map its location by fitting the data at low and high expansion rates using linear regression, shown in Figure 3.4. The subset of data used for each grouping is chosen based on the best fit to a linear equation, with at least three points used. The intersection of the two fits at a given MFC concentration then gives the critical area expansion rate, with the clearly significant amount of uncertainty quantified by error propagation from the standard errors of the original fits. The critical area expansion rate increases as fiber concentration increases, from around 400  $\mu\text{m}^2/\text{s}$ , in 0.023% MFC, to around 4000  $\mu\text{m}^2/\text{s}$  in 0.067% MFC gels.

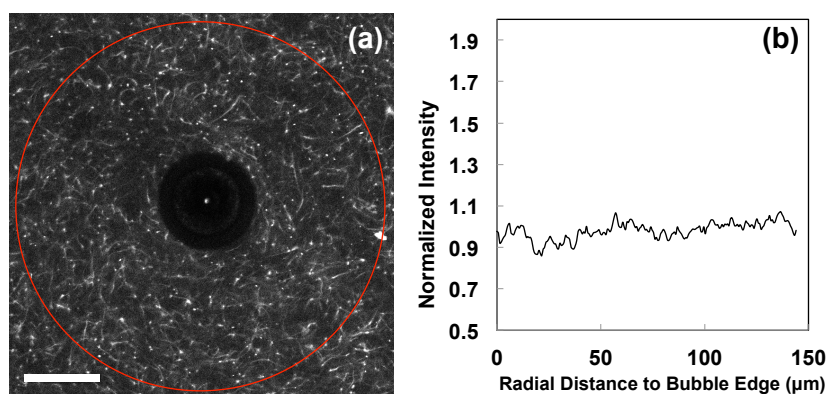


**Figure 3.5:** (a) Example of fiber density measurement using radial intensity averaging around the bubble tracer within the red circle boundary in a confocal microscopy image. The bubble is visible as a black circle at the image center. Scale bar is 100  $\mu\text{m}$ . (b) Plot of the normalized radial intensity profile of the image in (a), used to indicate the density of fibers present.

Local fiber consolidation provides a plausible explanation for the enhanced suspension ability of the MFC dispersions. The hypothesized consolidation can be directly quantified by confocal imaging of the fiber network as a function of position, relative to the expanding bubble. Local intensity of the fluorescing fibers indicates their relative concentration during an experiment. Figure 3.5 demonstrates the measurement of image intensity of a confocal image, Figure 3.5a, of 0.023% MFC around a bubble tracer. A radial profile of the intensity around the bubble is plotted as a normalized intensity relative to the average intensity, inside the red circle, before expansion, Figure 3.5b. An uncompressed network should maintain a normalized intensity around unity, with only minor random fluctuations, moving radially out from the bubble edge, as we see in Figure 3.5b. Figure 3.5b indicates the creation of a bubble tracer does not alter the surrounding network significantly. As the bubble is then expanded, its boundary can constantly exert a stress against the surrounding fibers at controlled rates. Any changes in network microstructure can then be identified, via imaging, and linked to the rate of small scale flow in the sample.

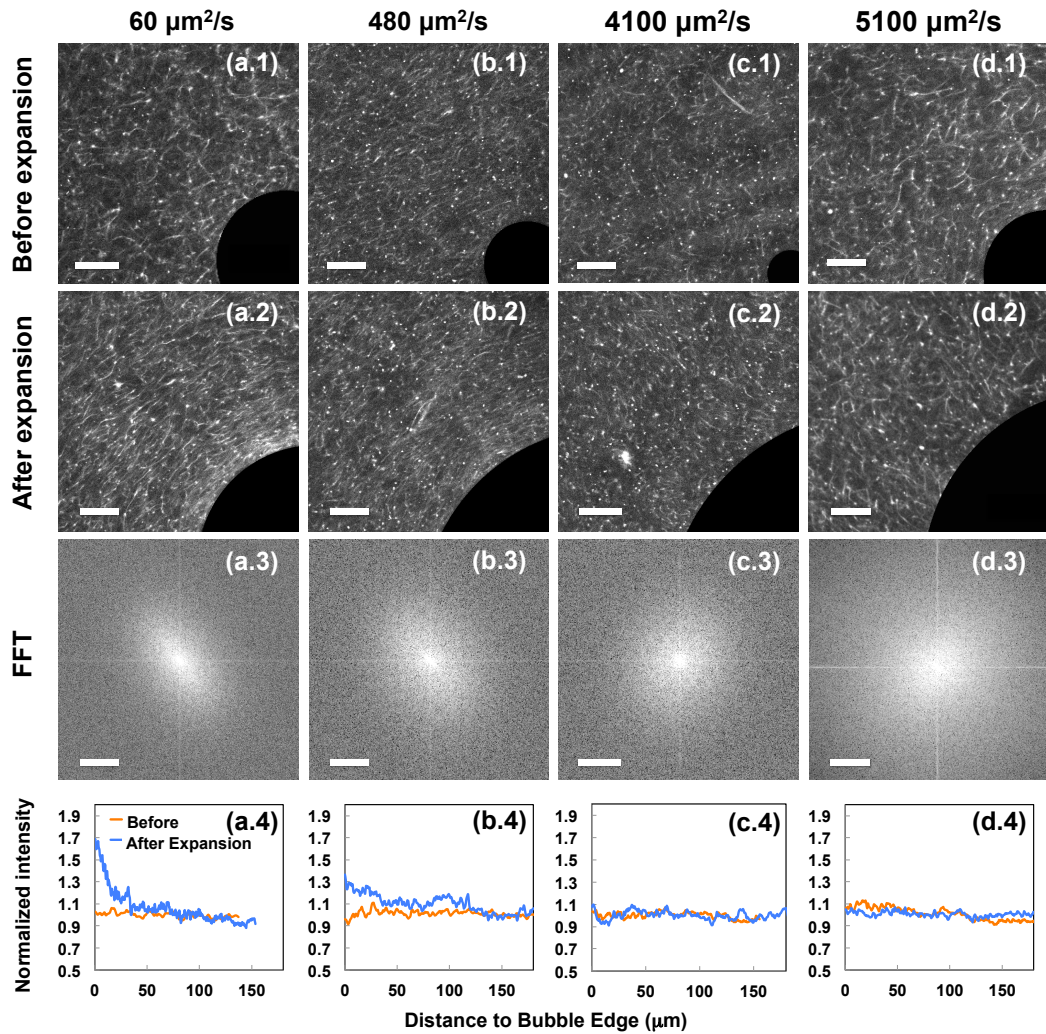


**Figure 3.6:** Confocal images of 0.023% MFC networks before (a.1 - d.1) and after (a.2 - d.2) expansion at the rates of  $60 \mu\text{m}^2/\text{s}$ ,  $480 \mu\text{m}^2/\text{s}$ ,  $4100 \mu\text{m}^2/\text{s}$  and  $5100 \mu\text{m}^2/\text{s}$ . Fast Fourier Transforms of the images in (a.2 - d.2) are shown in (a.3 - d.3) to characterize fiber orientation effects of bubble expansion. (a.4 - d.4) show plots of normalized radial intensity for each image as an indication of local fiber concentration. Scale bar is  $50 \mu\text{m}$ .

Figures 3.6a.1-3.6d.1 show confocal images of an MFC network before bubble expansion begins, where the bubble is visible as a dark circle in the lower right corner of each image. Bright spots are visible where small dye aggregates formed, but the labeled fibers are clearly identifiable, allowing their relative density and orientation to be mapped. Initially the fibers are randomly oriented and uniformly distributed relative to the bubble. Images obtained after continuous expansion at different rates are shown in Figures 3.6a.2 - 3.6d.2. A clear effect of expansion rate on local fiber packing is visible: slower expansions produce regions of clearly compressed fiber structures outside of the bubble boundary. The two lowest rates produce much denser packings, containing noticeably aligned fibers (Figures 3.6a.2 and b.2), while the two larger rates appear to have simply moved the fibers outward without significantly altering their packing or orientation (Figures 3.6c.2 and 3.6d.2). Image analysis allows us to quantify these changes, relative to the bubble surface position.

Figures 3.6a.3 - 3.6d.3 show fast Fourier transform, or FFT, images of the full field of view of the corresponding second row images as a measure of fiber orientation after expansion. Figure 3.6a.3 reveals a relatively sharp anisotropic pattern, indicating a significant number of fibers are oriented by the expanding bubble boundary. The angle of the FFT pattern,  $45^\circ$ , reflects the average fiber orientation with the spherical bubble edge, varying between  $60^\circ$  and  $30^\circ$  as a result of sustained radial compression. As expansion rate increases, we see a less defined anisotropic pattern in Figure 3.6b.3, and increasingly isotropic patterns in Figures 3.6c.3 and 3.6d.3, confirming the fibers have not significantly aligned or otherwise ordered.

The measurements of the variation of fiber intensity before and after bubble expansion at different expansion rates are shown in Figures 3.6a.4 - 3.6d.4. Initially, the density of fibers around the bubble is quite uniform for all rates studied, as

indicated by the orange line fluctuating around unity in Figures 3.6a.4 - 3.6d.4. After the bubble has expanded at low rates, fiber intensity is quite large at the bubble edge and decays rapidly moving away from it, Figures 3.6a.4 and 3.6b.4. A distinct peak near the bubble edge at the lowest expansion rate,  $60 \mu\text{m}^2/\text{s}$ , is about 60% larger than the baseline value. Increasing the expansion rate to  $480 \mu\text{m}^2/\text{s}$  produces less relative local compression, but a clear intensity peak is visible that is still 20% higher than the baseline value. The resultant increase in local yield stress observed in Figure 3.4 is thus consistent with increased fiber density at low deformation rates. Similarly, at higher expansion rates, above  $480 \mu\text{m}^2/\text{s}$ , the fibers around the bubble edge remain uniformly distributed and indistinguishable from those farther away, Figures 3.6c.4 and 3.6d.4.

After connecting the  $\sigma_s$  enhancement at low expansion rates with local fiber compression, we now seek a physical model of these results. The two-fluid model characterizes rate-dependent restructuring and yielding of a viscoelastic fluid by quantitatively coupling viscous stress, from the continuous phase fluid, with elastic stress from the dispersed fiber network.<sup>20,28</sup> The gel composed of fibers consists of a homogeneous and compressible elastic network, with a shear modulus,  $G$ , and compressive modulus,  $K$ , and an incompressible fluid with viscosity,  $\eta$ . The external force acting on the fluid results in the displacement of both elastic,  $\frac{\partial u}{\partial t}$ , and fluid phases,  $\frac{\partial v}{\partial t}$ :

$$\rho_e \frac{\partial^2 u}{\partial t^2} = (K + \frac{1}{3}G)\nabla(\nabla \cdot u) + G\nabla^2 u + \Gamma_\xi(v - \frac{\partial u}{\partial t}) \quad (3.2)$$

$$\rho_f \frac{\partial v}{\partial t} = -\nabla p + \eta\nabla^2 v - \Gamma_\xi(v - \frac{\partial u}{\partial t}) \quad (3.3)$$

where  $\rho_e$  and  $\rho_f$  represent the mass densities of the elastic and fluid phases, respectively, and  $\Gamma_\xi$  is a friction coefficient that relates the force exerted on either phases to the relative velocities between the fluid and solid phases. Treating the

network as porous media with pore spaces set by mesh size  $\xi$ ,  $\Gamma_\xi$  is given by the Darcy permeability:

$$\Gamma_\xi \sim \frac{\eta}{\xi^2} \quad (3.4)$$

The critical time scale for network “draining” can be estimated from Equation 3.2 and 3.3, solved for small bubble oscillation at frequency  $\omega$ . The transition between compressible and incompressible deformation occurs at a critical frequency that arises when the relative velocity between liquid and solid phases becomes appreciably non-zero. This occurs at frequency,  $\omega_c$ , which corresponds to:<sup>22</sup>

$$\omega_c = \frac{G\xi^2}{\eta R^2} \quad (3.5)$$

Above the critical frequency, viscous coupling dominates and the network and fluid deform as a single unit. Below the critical frequency, the liquid has time to drain from the elastic network. The drainage of liquid from compressed elastic networks, at low frequency, under external stress results in heterogeneous microstructure deformation.<sup>28</sup> It is valuable to now compare the model predictions with our experimental observations as a preliminary evaluation of our hypothesis of two-fluid behavior.

In shear rheometry, the Cox-Merz “rule” posits that the steady shear viscosity  $\eta(\dot{\gamma})$  of a material is equal to the real part of the (frequency-dependent) complex viscosity,  $\eta'(\omega)$ . Its validity is based on the argument that critical frequencies,  $\omega_c$ , at which a material response changes qualitatively correspond to dominant relaxation times,  $\tau_c \sim \omega_c^{-1}$ , of the equilibrium microstructure. Consequently, for steady shearing at low shear rates, *i.e.*, where  $\dot{\gamma}\tau_c \ll 1$ , systems are not driven significantly from equilibrium, since the material relaxes far more quickly than the shearing

deforms it. When  $\dot{\gamma}\tau_c \sim 1$ , on the other hand, the material is driven significantly from equilibrium.

By analogy, we suggest that the critical drainage frequency  $\omega_c$ , given by Equation 3.5, reflects the critical time scale  $\tau_c \sim \omega_c^{-1}$ , for the two fluids to freely drain relative to one another. We thus expect that a bubble that expands at an area expansion rate

$$\dot{A} = \dot{\gamma}R^2, \quad (3.6)$$

much slower than  $\tau_c$  permits fluid to drain from the fiber matrix around the bubble while also compressing the fibers. Bubbles that expand faster than

$$\dot{A}_c \sim \omega_c R^2 = \frac{G\xi^2}{\eta}, \quad (3.7)$$

on the other hand, deform the MFC gel incompressibly. We hypothesize that  $\dot{A}_c$  reflects the transition to heterogeneous (compressive) MFC deformation, and that the effective suspending yield stress is larger at slow expansion rates ( $\dot{A} < \dot{A}_c$ ) than at fast rates.

The dependence of the critical expansion rate,  $\dot{A}_c$ , on MFC concentration can be estimated using complementary experimental results. Previous rheology measurements on MFC<sup>17</sup> revealed the shear modulus grows with concentration like  $G \sim \Gamma C^{2.5 \pm 0.1}$ . The characteristic pore size of networks of long, semi-flexible cylinders scales like  $\xi \approx k/\sqrt{C}$ , where  $k$  is a constant that varies with fiber system.<sup>29,30</sup> With these results, Equation 3.7 becomes

$$\dot{A}_c \sim \left( \frac{\Gamma k^2}{\eta} \right) C^{1.5}, \quad (3.8)$$

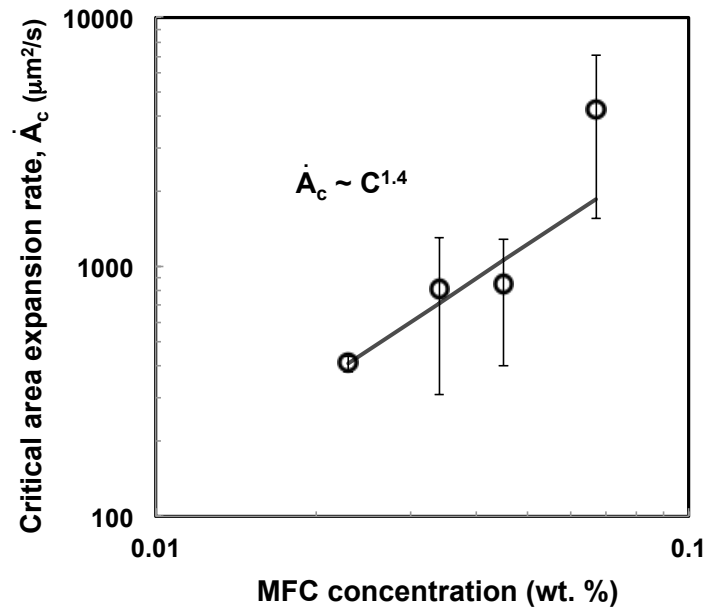


**Figure 3.7:** The critical area expansion rate, obtained from Figure 3.4, increased with increasing MFC concentration with a power law exponent of  $1.4 \pm 0.4$  from an error-weighted best fit to the data.

predicting a power-law relationship where critical area expansion rate  $\dot{A}_c$  increases with MFC concentration by an exponent of  $1.5 \pm 0.1$ .

The critical area expansion rates, estimated from the transition of rate-independent to rate-dependent yielding in Figure 3.4, are plotted as a function of MFC concentration in Figure 3.7. The potential critical area expansion rates at each MFC concentration are determined from the intersection of two linear fits to the data, Figure 3.4, and the error bars indicate the significant uncertainty propagated from the standard error of the slope and intercept of each fit. The results show a power law increase of critical area expansion rates with increasing fiber concentration, with an exponent of  $1.4 \pm 0.4$  from an error-weighted best fit to the data, Figure 3.7. We see reasonable agreement of the experimental and theoretical scaling behavior,

though the significant uncertainty in the measurements suggests the need for more detailed study.

Measurements of the transitional expansion rates from bubble studies agree loosely with the compaction prediction by the two-fluid model, and are in turn consistent with our direct confocal microscopy observations in Figure 3.6. We conclude that the enhanced suspension yield stress observed in slowly-growing bubbles arises due to structural rearrangement and reinforcement. The changes of structures observed in Figure 3.6, occur as a result of a complex balance of compression, deformation, and fluid flow through porous media. Models of such complex flows are beginning to be developed and applied to describe polymer gel mechanics and cellular response<sup>31</sup>, as well as commercial product performance<sup>7</sup>.

### **3.4 Conclusions**

This work examined the rate dependence of small-scale colloidal fiber network yielding to explain previous observations of enhanced suspension ability. The bubble rheometer enables the study of microscale fluid yielding by controlling headspace pressure to vary bubble size and applied stress. The rate at which the bubble expands and strains the network determines the final local suspension stress of the network, with faster rates producing a weaker suspension stress than slow rates. The mechanism for the significant changes in suspension ability is the localized consolidation of the poroelastic network of fibers. When bubbles expand slowly, the network is locally expels interstitial water, consolidates, and becomes denser. Confocal studies of the fiber network at different expansion rates confirm that consolidation occurs and identify the transition from structural rearrangement to uniform network yielding. The work indicates rich possibilities for further study of local structure and rheology evolution within sparse gels, especially with techniques

like active microrheology<sup>32</sup>. Application of these phenomena to design responsive, efficient complex fluids will be of use for soft material development as well as understanding analogous cellular and biophysical behavior. The insight that two-fluid behavior can describe rate-dependent yielding of sparse gels nicely connects the fields of microrheology and poroelasticity in soft materials. Additional innovations are envisioned where commercially relevant phenomena, like product stability and gel collapse<sup>33</sup>, are controlled.

### 3.5 References

- [1] A. Okiyama, M. Motoki, S. Yamanaka, *Food hydrocolloids* **1993**, *6*, 503–511.
- [2] P. M. Young, D. Traini, H. X. Ong, A. Granieri, B. Zhu, S. Scalia, J. Song, P. T. Spicer, *Drug Development and Industrial Pharmacy* **2017**, *43*, 1729–1733.
- [3] B. D. Olsen, J. A. Kornfield, D. A. Tirrell, *Macromolecules* **2010**, *43*, 9094–9099.
- [4] R. Buscall, P. Mills, R. Stewart, D. Sutton, L. White, G. Yates, *Journal of Non-Newtonian Fluid Mechanics* **1987**, *24*, 183–202.
- [5] M. Fourmentin, G. Ovarlez, P. Faure, U. Peter, D. Lesueur, D. Daviller, P. Coussot, *Rheologica Acta* **2015**, *54*, 647–656.
- [6] M. J. Solomon, P. T. Spicer, *Soft Matter* **2010**, *6*, 1391–1400.
- [7] H. Emady, M. Caggioni, P. Spicer, *J. Rheo.* **2013**, *57*, 1761–1772.
- [8] S. J. Veen, A. Kuijk, P. Versluis, H. Husken, K. P. Velikov, *Langmuir* **2014**, *30*, 13362–13368.
- [9] S. M. Keshk, *Journal of Bioprocessing & Biotechniques* **2014**, *2014*, 1–10.
- [10] G. M. Wilkins, P. T. Spicer, M. J. Solomon, *Langmuir* **2009**, *25*, 8951–8959.
- [11] P. C. Møller, J. Mewis, D. Bonn, *Soft matter* **2006**, *2*, 274–283.
- [12] P. Quinto-Su, X. Huang, S. Gonzalez-Avila, T. Wu, C. Ohl, *Physical review letters* **2010**, *104*, 014501.

- 
- [13] M. Gardel, J. Shin, F. MacKintosh, L. Mahadevan, P. Matsudaira, D. Weitz, *Science* **2004**, *304*, 1301–1305.
- [14] J. Sprakel, S. B. Lindström, T. E. Kodger, D. A. Weitz, *Physical review letters* **2011**, *106*, 248303.
- [15] A. B. Fall, S. B. Lindström, J. Sprakel, L. Wågberg, *Soft Matter* **2013**, *9*, 1852–1863.
- [16] P. Ronceray, C. P. Broedersz, M. Lenz, *Proceedings of the National Academy of Sciences* **2016**, 201514208.
- [17] J. Song, M. Caggioni, T. M. Squires, J. F. Gilchrist, S. W. Prescott, P. T. Spicer, *Rheologica Acta* **2019**, *58*, 231–239.
- [18] M. M. Denn, D. Bonn, *Rheologica acta* **2011**, *50*, 307–315.
- [19] F. Brochard, P. De Gennes, *Macromolecules* **1977**, *10*, 1157–1161.
- [20] A. J. Levine, T. Lubensky, *Physical Review E* **2001**, *63*, 041510.
- [21] P. Lopez-Sanchez, M. Rincon, D. Wang, S. Brulhart, J. Stokes, M. Gidley, *Biomacromolecules* **2014**, *15*, 2274–2284.
- [22] H. C. de Cagny, B. E. Vos, M. Vahabi, N. A. Kurniawan, M. Doi, G. H. Koenderink, F. C. MacKintosh, D. Bonn, *Physical Review Letters* **2016**, *117*, 217802.
- [23] M. Bouzid, E. Del Gado, *Langmuir* **2018**, *34*, 773–781.
- [24] M. Vahabi, B. E. Vos, H. C. De Cagny, D. Bonn, G. H. Koenderink, F. C. Mackintosh, *Physical Review E* **2018**, *97*, 32418.
- [25] M. Gardel, J. Shin, F. MacKintosh, L. Mahadevan, P. Matsudaira, D. Weitz, *Physical review letters* **2004**, *93*, 188102.
- [26] C. A. Schneider, W. S. Rasband, K. W. Eliceiri, *Nature Methods* **2012**, *9*, 671–675.
- [27] M. Pääkkö, M. Ankerfors, H. Kosonen, A. Nykänen, S. Ahola, M. Österberg, J. Ruokolainen, J. Laine, P. T. Larsson, O. Ikkala *et al.*, *Biomacromolecules* **2007**, *8*, 1934–1941.
- [28] F. Gittes, B. Schnurr, P. Olmsted, F. C. MacKintosh, C. F. Schmidt, *Physical review letters* **1997**, *79*, 3286.
- [29] F. Meng, E. M. Terentjev, *Polymers* **2017**, *9*, 52.
- [30] L. Hough, M. Islam, B. Hammouda, A. Yodh, P. Heiney, *Nano letters* **2006**, *6*, 313–317.

## References

---

- [31] X. Xu, S. A. Safran, *Physical Review E* **2017**, 95, 052415.
- [32] J. P. Pantina, E. M. Furst, *Phys. Rev. Lett.* **2005**, 94, 138301.
- [33] S. Manley, J. Skotheim, L. Mahadevan, *Physical Review Letters* **2005**, 94, 1–4.

## Chapter 4

# Accelerated gravitational yielding of sparse fiber colloidal gels

### 4.1 Introduction

Particle sedimentation in fluids is important across broad industrial areas, and can be a helpful phenomenon, aiding separation of valuable minerals<sup>1</sup> and clean water<sup>2</sup>, or a negative effect when commercial products physically separate during their shelf-life.<sup>3,4</sup> The hydrodynamics of a single particle falling through a fluid are described by Stokes' Law, while Kynch developed a theory for the settling process of concentrated hard-sphere particle dispersions due to local particle crowding.<sup>5</sup> Particles in colloidal gels, however, have strong attractive interactions that create an elastic, space-filling microstructure that deforms and fails under gravity with complex dynamics.<sup>6-8</sup>

The gravitational collapse of colloidal gels has been extensively studied for spherical Brownian particles,<sup>9,10</sup> identifying the ability of diffusive particle rearrangement to cause sudden collapse after a period of elastic compression.<sup>11-13</sup> Solvent back-flow rates determine the initial rates of collapse in both cases due to viscous drag, but the overall magnitude depends on the balance between gravitational stress and gel elasticity.<sup>6</sup>

The delayed collapse occurs widely in attractive colloidal gels composed of spheres because of structure erosion driven by thermal diffusion in a gel.<sup>11,12</sup> The delayed

time can vary from  $10^2$  to  $10^6$  seconds due to different degree of attractive force between particles.<sup>7</sup> Increasing attractive interactions or particle concentrations can slow down thermal diffusion and increase the delay time.<sup>14</sup> Bulk flow studies also found delayed yielding in attractive colloidal gels when applied shear stress exceeded the gel yield stress. The results were explained using a bond-rupture model that suggested the differential rates between inter-particle bond breaking and reformation determines delay time.<sup>9,11,15-17</sup>

While gels of entirely Brownian particles undergo diffusional rearrangement of particles that can cause catastrophic collapse, microfibrillar cellulose gels possess a unique blend of nanoscale and microscale dimensions, making them efficient and less prone to diffusional rearrangements. The collapse dynamics of gels like microfibrillar cellulose (MFC), however, have not been well explored, despite their efficiency at practical functions like suspension of particles, rheological modification<sup>18,19</sup> and two-fluid resistance<sup>20,21</sup> to yielding. Traditional gravitational collapse studies are hard to perform on such low concentration gels composed of fibers as their driving force for collapse is minimal.

Conventional gel collapse tests are time-consuming and highly variable because of dependence on gel stress alone. Phase separation must often be observed over time scales from a few months to even a year. Such slow dynamics hinder efficient use for prediction of consumer product stability, and accelerated aging by centrifugation is not representative due to network damage. Although some theories have been developed to model and predict the dynamics of collapse in gels of spherical particles,<sup>8-10</sup> commercial products often use rheological modifiers with more complex shapes to minimize cost, complicating theoretical prediction of real sedimentation.

In this chapter, we accelerate the sedimentation of gels composed of fibers at low volume fractions by increasing the gravitational stress with uniform addition of dense suspended particle loads. Systematically increasing gravitational stress in a controlled way enables careful study of the gel yielding phenomenon, and better mimics the practical use of such gels in, for example, consumer products with suspended particles or droplets. Local microstructure changes of gels during bulk collapse were studied by tracking the motion of tracer particles. The initial solvent back-flow largely controls the gel sedimentation kinetics, similar to the case of gels of spherical particles, and we show that the process can be predictably tuned by increasing the viscosity of the gel liquid phase. The use of gel collapse as a fluid suspension characterization technique enables determination of important kinetic parameters, as well as characterization of gel structural parameters like colloid network permeability. We suggest the method as a way to enable accelerated testing and modeling of gel collapse, providing a quantitative physical approach to optimization of chemical product design.

## **4.2 Experimental methods**

### **4.2.1 Sample preparation**

Commercial bacterial cellulose (Wong Coco, Indonesia) was first soaked and rinsed in deionized water multiple times to remove any non-cellulosic contaminants. Microfibrous cellulose dispersions were then prepared using mechanical disruption in a laboratory blender for coarse dispersion followed by a similar time in a high-shear homogeniser (T18 digital Ultra Turrax homogenizer, IKA) for uniformity. The resulting dispersions contain fibers with a width around 40 – 60 nm and length of 5 – 10  $\mu\text{m}$ .<sup>19,22</sup> The fiber concentration of each starting dispersion was determined

by comparison of the sample weight before and after oven drying to determine solids level. Kathon (Supelco, USA) preservative was added at 0.1 wt.% to all dispersions to prevent bacterial contamination.

Subsequent dilutions of MFC gels were prepared from stock dispersions by mixing with deionized water. Each new MFC gel was initially homogenised for about 5 minutes before experiments. Particles of silicon dioxide (Sigma-Aldrich, USA), with density of  $2.65 \text{ g/cm}^3$  and size of  $5 \mu\text{m}$  ( $> 90\%$ ) were added to apply a controlled gravitational stress on MFC gels. After adding  $\text{SiO}_2$ , samples were gently shaken to disperse the heavy particles in the fiber networks before exploring their collapse dynamics.  $\text{SiO}_2$  and cellulose fibers do not significantly interact because of negative charges on both surfaces.<sup>23</sup> The loaded particles thus do not affect the original mechanical properties of fiber networks, as we verified by rheology. Since 90% of the  $\text{SiO}_2$  particles are larger than  $5 \mu\text{m}$  and the average mesh size of the fiber network at the lowest concentration studied here is around  $0.3 \mu\text{m}$ ,<sup>24</sup>  $\text{SiO}_2$  particles can be assumed to be trapped in the fiber networks after dispersion. Local gel strain was tracked during sedimentation using  $300 \mu\text{m}$  tracer particles (Polyscience, USA) trapped in the gels in order to link bulk phenomena to microstructure changes during different collapse phenomena.

### 4.2.2 Visual observations

The microstructure of fiber networks containing  $\text{SiO}_2$  particles was studied via differential interference contrast (DIC) imaging on a Leica DM2500M microscope. The accelerated gravitational collapse of MFC gels was studied using time-lapse imaging. Sample volumes of 40 mL and initial sample height,  $h_0$ , of 6.8 cm were transferred into glass vials and time-lapse observations started immediately at  $25^\circ\text{C}$ . Images were subsequently analysed using ImageJ to track movement of the air-

liquid interface height as well as tracer particle motion.<sup>25,26</sup> Multiple samples were assessed to ensure reproducibility.

The small width of the sample, less than 10 mm, can significantly alter the collapse process because the breaking of gel microstructure often starts from the walls and propagates to the bulk.<sup>27</sup> The beginning of structure collapse can be influenced by particle nucleation at the interface.<sup>8</sup> The dispersed particles at the air-water interface need to overcome interfacial drag before settling, which may slow down the initial collapse process.

### 4.2.3 Rheology measurement

The rheology of the gels was measured on a stress-controlled rheometer (AR-1500, TA instruments, New Castle, DE) with cone and plate geometry (cone diameter 60 mm, angle 2°). All measurements were performed at 25 °C and after a 30 s pre-shear, followed by a two minute relaxation. The continuous phase viscosity was tuned by addition of 20% glycerine solution (Sigma-Aldrich, USA) to diluted MFC dispersions. After collapse was judged to have stopped, the upper supernatant mixture of water and glycerine was sampled for viscosity measurement. The liquid was loaded on the rheometer and sheared from 1000 s<sup>-1</sup> to 1 s<sup>-1</sup> to measure its viscosity.

Measurement of the bulk yield stress,  $\sigma_y$ , of MFC gels was performed by shearing the samples under steady state flow with shear rate decreasing from 1000 s<sup>-1</sup> to 1 s<sup>-1</sup>. The shear stress response reduced with shear rate until a critical shear rate, after which the measured shear stress increased due to some re-building of microstructure on time scales shorter than the flow rate.<sup>28,29</sup> Only data from above the transition to structure recovery were fitted to the Herschel-Bulkley equation to

determine bulk yield stress:

$$\sigma = \sigma_y + K\dot{\gamma}^n \quad (4.1)$$

Here  $\sigma$  is the total fluid stress,  $K$  is the consistency factor,  $\dot{\gamma}$  is the shear rate, and  $n$  is the flow index. The particle-scale suspension stress,  $\sigma_s$ , can be connected to bulk yield stress,  $\sigma_y$ , by the dimensionless yield stress,  $Y$ :<sup>30</sup>

$$Y = \frac{\sigma_y}{\sigma_s} = \frac{2\pi R^2 \sigma_y}{\frac{4}{3}\pi R^3 (\rho_p - \rho_l) g} \quad (4.2)$$

Here  $R$  is the particle radius,  $g$  is the gravitational constant, and  $\rho_p$  and  $\rho_l$  are the density of the silica particle and continuous phase fluid, respectively. The  $Y$  value for MFC suspensions is known to be  $\sim 0.1$  from sedimentation experiments,<sup>18</sup> meaning the  $\sigma_s$  of MFC gels can be as much as ten times larger than  $\sigma_y$ .

#### 4.2.4 Curve fitting and calculation

The collapse dynamics of MFC gels were determined using re-sliced images from the middle position of the vials, Figure 4.1b, to fit pixel position to linear and exponential functions:<sup>6</sup>

$$h(t) = a_1 t + b_1 \quad (4.3)$$

$$h(t) = a_2 e^{-b_2/t} + c_2 \quad (4.4)$$

Where  $h(t)$  is instantaneous interface height,  $t$  is collapse time, and  $a$ ,  $b$ , and  $c$  are fitting constants.

Gravitational stress in the system is dominated by the loaded silica particles because of the relatively low concentration of fibers<sup>31</sup> and its variation with vertical

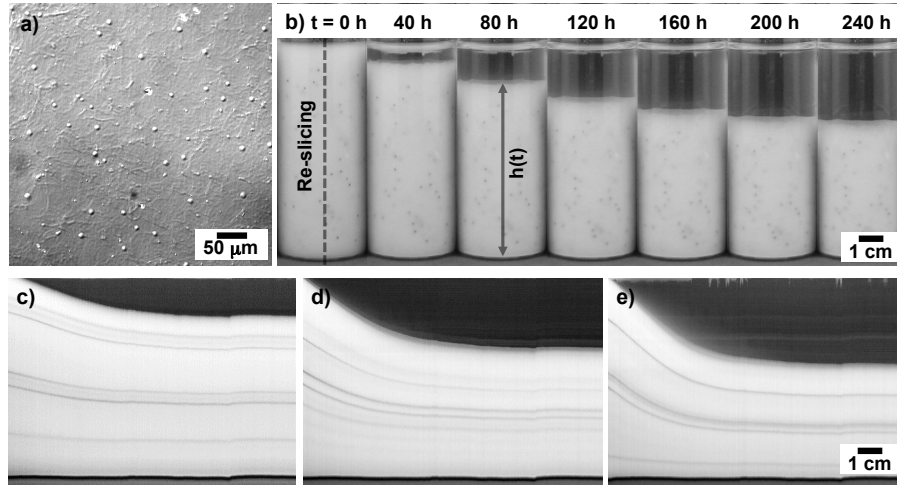


**Figure 4.1:** (a) DIC image of sparse fiber networks incorporating trapped  $\text{SiO}_2$  particles. Image sequences in (b) illustrate collapse of an MFC gel over time as a result of  $\text{SiO}_2$  loading. Black dots are  $300\ \mu\text{m}$  tracer particles suspended within the networks. (c - e) Composite kymograph images of 0.11 wt. % MFC gel with three loadings of  $\text{SiO}_2$ , 1 wt.%, 2 wt.% and 3 wt.% respectively, showing the decrease of interfacial height and tracer trajectories over time.

position,  $z$ , can be calculated from:

$$\sigma_s(z) = \frac{(\rho_p - \rho_l)gV_p}{\pi r^2} \times \left(1 - \frac{z}{h_{susp}}\right) \quad (4.5)$$

Here,  $V_p$  is the total volume of loaded particles,  $r$  is vial inner radius, 1.5 cm, and  $h_{susp}$  is suspension height.

By tracking and analysing the movements of trapped tracers at different heights, we quantified the degree of microstructure deformation by local strain. The local compressive strain,  $\epsilon$ , is calculated from changes in distance between targeted tracers:

$$\epsilon = \frac{L - L'}{L} \quad (4.6)$$

Where  $L$  and  $L'$  are the initial and instantaneous distance between analysed tracers.

### 4.3 Results and Discussion

Figure 4.1a shows a microscopic image of MFC gels with the loaded SiO<sub>2</sub> particles trapped within the sparse fiber network. Low concentration MFC gels are essentially transparent, but dispersed SiO<sub>2</sub> particles scatter light in the sample and make them opaque, as seen from macroscopic observation of the vial, Figure 4.1b at  $t = 0$ . The dense SiO<sub>2</sub> increases the gravitational stress on the fiber network and accelerates gel sedimentation. A time-lapse image sequence of 0.11 wt.% MFC with 2 wt.% loaded SiO<sub>2</sub> requires 10 days to collapse to its final height, Figure 4.1b. As the fiber and SiO<sub>2</sub> suspension interface height decreased, clarified water is visible at the top. Depending on the particle load and yield stress of the formulation, commercial collapse tests can require a few months to a year to complete. Centrifugation is sometimes used in an attempt to accelerate the outcome and predict long-term results, but the much stronger additional stress can simply destroy the gel structure without measuring true long-term stability. Adjusting the loading of heavy particles, without dramatically affecting the original network properties, can accelerate the collapse process without changing the key physics.

Combining a one-pixel wide slice from each frame of the time-lapse images into a composite kymograph shows how the interface height falls over time. The kymographs in Figures 4.1c - 4.1e show that sedimentation became more significant for 0.11% MFC gels, in terms of both initial speed and total interface height reduction, when SiO<sub>2</sub> concentration was increased from 1 wt.% to 3 wt.%. The quick collapse of the structure at high loads of SiO<sub>2</sub> results in re-suspension of a minor mass of small SiO<sub>2</sub> particles because of strong back-flow, which can be seen from the blurred white areas on the top of collapse boundary in Figure 4.1e and is consistent with simulations of the collapse of Brownian systems<sup>32</sup>. The large tracers also settle

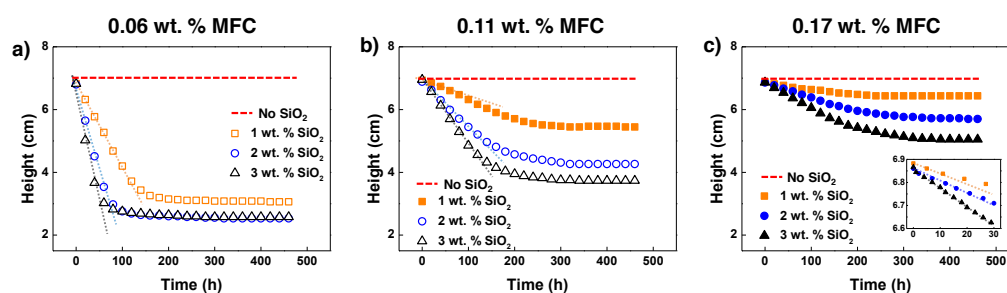


**Figure 4.2:** Interface height changes over time in three MFC concentrations and different loadings of  $\text{SiO}_2$ . There was no collapse occurring in pure MFC gels within the observation time of 480 hours, while loading  $\text{SiO}_2$  increases gravitational stresses, accelerating gel structure yielding. Depending on the competition between gel network strength and gravity, the samples experienced either a fast collapse (open symbols) or slow condensation (solid symbols). The initial reduction of interface height was linear for all the samples.

along with the fiber networks during a collapse, and the black lines in Figures 4.1c - 4.1e are tracer trajectories that quantify local structure deformation.

Quantitative image analysis allows us to plot the MFC gel interface height with time for different concentrations and applied stresses, Figure 4.2. In MFC dispersions without any additional particles, the gel structures were stable, and the interface height remained constant at 6.8 cm with time for all MFC concentrations studied here. The addition of  $\text{SiO}_2$  provides the driving force for sedimentation of the gel, and for all systems there are two main stages of behavior. In the initial stage of sedimentation the interface height falls linearly with time, consistent with studies of spherical particle gels, and is the result of viscous back-flow through the porous medium of the MFC gel.<sup>6</sup> After some time, sedimentation slows and height decays exponentially as compression of the elastic gel microstructure dominates the process, Figure 4.2. Increasing the amount of particle load proportionally increases the rate of linear sedimentation in the MFC gels, while an increase in fiber concentrations slows the initial linear sedimentation process by reducing the permeability of the gel and increasing resistance to fluid back-flow, Figure 4.2.

Sedimentation in Figure 4.2 approaches equilibrium within 10 days based on plateau heights in the later stages. The gels at low concentration collapsed quickly under applied gravitational stress and reached a final height of around 3 cm, Figure 4.2a, indicating the maximum compaction of the gel dominates final sedimentation height. The final height depends more strongly on the percentage of loaded SiO<sub>2</sub> at MFC concentrations above 0.06 wt.%, Figures 4.2b and 4.2c, but the final height is much larger than at lower MFC concentrations. Reducing the proportion of loaded SiO<sub>2</sub> particles noticeably decreases the degree of sedimentation because the compression of fiber networks is stress-responsive. At 0.17 wt.% MFC and above, the network may not even rupture, instead just compressing poroelastically, indicating a degree of responsiveness that is valuable in formulating commercial fluid products. We emphasize as well that the MFC is highly efficient, providing strong resistance to significant particle load stresses at concentrations 10-100X smaller than those used to create spherical colloidal gels.<sup>8</sup>

Distinct from past work on colloidal gels of spherical particles, for all the gels of non-Brownian fibers studied no delay was observed before collapse began. The absence of a delay is likely because the fibers, though only nanometers thick, have a micron-scale length that prevents significant diffusion. For the MFC gels, changes in microstructure are driven solely by gravitational stress, which can either compress the elastic structure or directly break connections between fibers.

Quantitative analysis of collapse dynamics shows two distinct behaviors: fast yielding and poroelastic compression, Figure 4.3. In 0.11% MFC gels, both phenomena were observed as SiO<sub>2</sub> concentration increased, so this system is used as an example here. Under low 1% SiO<sub>2</sub> loading, the MFC gel compressed poroelastically, Figure 4.3a. In this case, the gel strength is larger than gravitational stress and the interface height decreased exponentially with time over almost the entire

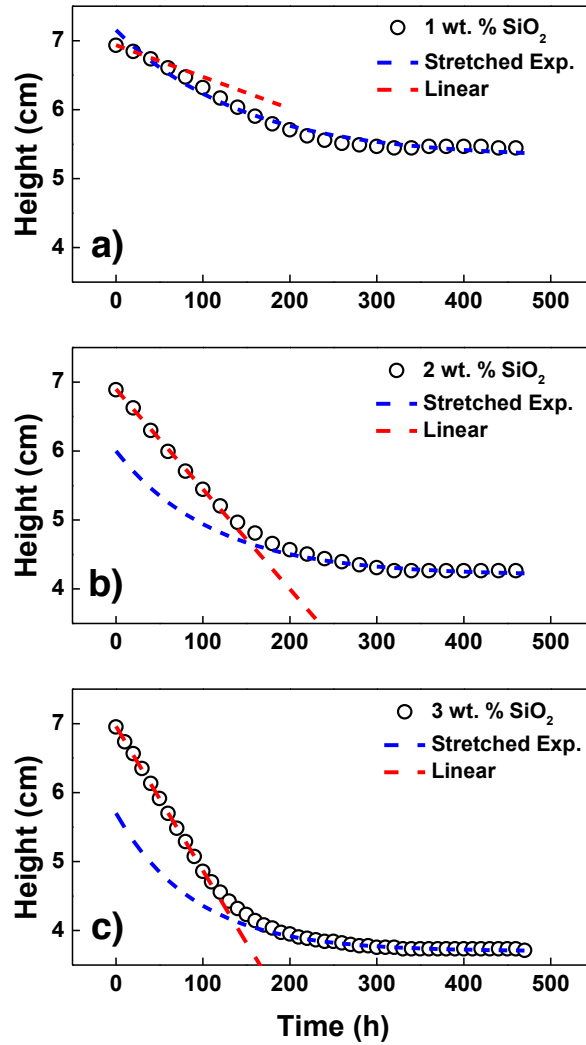


**Figure 4.3:** The transition from poroelastic compression to fast yielding dynamics were explored in 0.11% MFC gels when increasing loaded SiO<sub>2</sub> concentrations. Quantitative fittings on the plots of interfacial height as a function of time indicate two collapse regimes: elastic compression (a), in which the overall sample was compressed exponentially, and fast collapse (b - c), referring to a long time linear yielding followed by an exponential consolidation.

process, with just a small linear region at short times. The results indicate that the bulk MFC gel structure can be compressed by as much as 30% without significant yielding, which is more than three times higher than the compressive yielding strain of around 10% found in the gravitational collapse of gels of spherical particles.<sup>6</sup> The large compressive strain in MFC gels results from a much higher capacity for structural rearrangement,<sup>18</sup> enabling large non-linear deformation that enhances fiber structure suspension performance.<sup>19,33,34</sup>

As particle loads increase to 2 wt.% and 3 wt.%, the interface height of the samples decreased more sharply with larger linear region, followed by a stretched exponential compaction, Figures 4.3b and 4.3c. In these cases, the gravitational stress is higher than the MFC gel strength, resulting in localised yielding.<sup>6</sup> For semi-stable spherical gels, network fracture occurs throughout the whole sample after a delay period, and the final sedimentation height is a result of maximum compaction of particles.<sup>8</sup> In our systems, if the entire fiber network ruptures and all particles simply settled down, the final sediment height should be dominated by the maximum compaction of fibers, as they have a much larger excluded volume than SiO<sub>2</sub> spheres.<sup>35</sup> The local gel structure deformation should then be a strong function of gravitational stress at different sample heights, contrary to spherical gels that experienced integral structural failure when yielding.

Local structure deformation during sedimentation is mapped by tracking motion of 300  $\mu\text{m}$  polystyrene tracers density-matched with water. Figure 4.4 shows microstructure deformation in four MFC gel concentrations under controlled loads of 1.5 wt.% SiO<sub>2</sub>. This system covers the full range of collapse dynamics, from fast yielding to elastic compression. At low MFC concentrations, the gel experienced a clear bottom-up collapse as strain starts increasing from the bottom where stress is highest, Figure 4.4a and 4.4b. However, in some sub-stable gels, collapse can

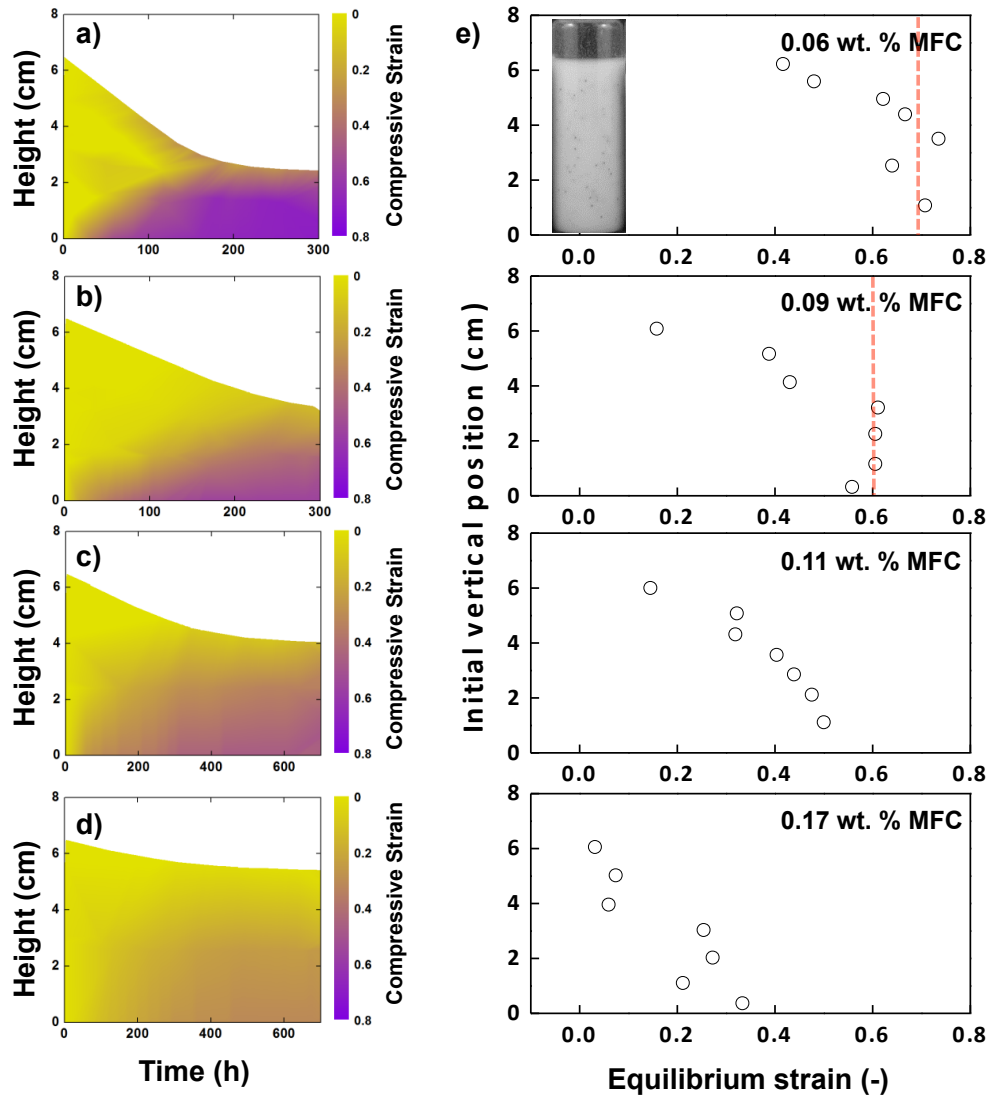


**Figure 4.4:** (a - d) Time evolution of the height profile, with a superimposed heat map of the compressive strain,  $\epsilon$ , under controlled loads of 1.5 wt.% SiO<sub>2</sub> at 0.06 wt.%, 0.09 wt.%, 0.11 wt.% and 0.17 wt.% MFC. (e) Total local microstructure deformation is plotted against the initial vertical sample position to demonstrate possible onset of structural yielding in the gel when particle load stress dominates. The red dashed lines indicated yielding strains.

be initiated from the top of the sample, where a dense disconnected particle layer formed<sup>8</sup> or many small cracks were generated<sup>27</sup>, leading to a sudden bulk collapse. When increasing MFC concentrations to more than 0.1 wt.%, the gel suspension stress is higher than the maximum gravitational stress, and the overall microstructure is able to rearrange and dissipate stress without yielding. In this case, the overall structure was compressed gradually, but more significant closer to the bottom of the sample, Figure 4.4c and 4.4d.

The equilibrium strain is the maximum deformation of microstructure under an applied load. Figure 4.4e plots the equilibrium strain as a function of initial vertical position, showing the deformation of sparse fiber networks is highly stress-responsive. Although the data are scattered, we note a potentially discontinuous transition due to structural yielding. In weak MFC gels, the bottom of the sample shared a similar equilibrium strain because of microstructure failure that allows fibers and silica particles to pack randomly. The maximum equilibrium strain was found to be roughly 0.7 in 0.06 wt.% MFC gel and reduced to 0.6 when MFC concentration increased to 0.09% MFC, Figure 4.4e (dash lines). Past studies on fiber networks found the structures experience linear deformation, when  $\epsilon < 0.1$ , followed by a large region of non-linear deformation as  $\epsilon \sim 0.6$ .<sup>19,36</sup> The yielding strain of fiber networks at low concentrations ranges from 0.6-1.2,<sup>36,37</sup> which confirms our prediction of network rupture in the bottom of fast yielding gels.

However, on the top of the sample in fast yielding, the equilibrium strain decays linearly approaching the water-air interface, showing a poroelastic compression process. The boundary between network break and compression occurred at the vertical position where the gravitational stress is comparable to the gel suspension yield stress. For example, in 0.06% MFC the structure yielding starts from the height of 3.4 cm - 4.4 cm, where the gravitational stress ranges from 1.2 Pa to 1.7 Pa, quite

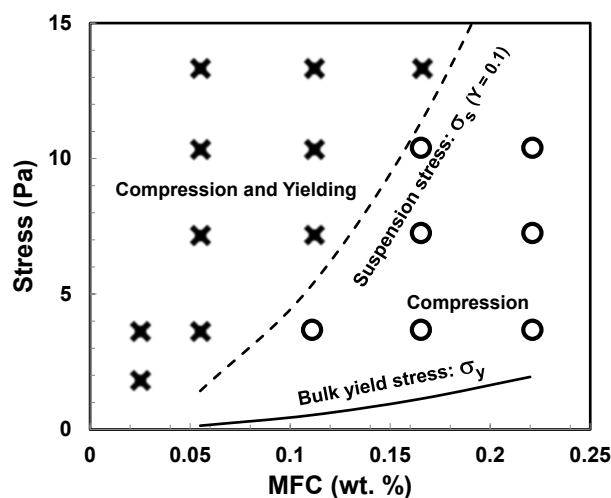


**Figure 4.5:** Fast yielding occurred (error symbols) when the stress, generated from loaded  $\text{SiO}_2$ , is higher than  $\sigma_s$  of MFC gels (dash line), while the gels compressed elastically (circles), when the applied stress is smaller than gel  $\sigma_s$ . The bulk yield stress (solid line) underestimates the suspension ability of MFC gels.

close to the suspension yield stress of the gel, around 1.4 Pa. The observation of poroelastic compression on the top of the sample during fast yielding also supports our hypothesis of partial structure preservation, proposed in Figure 4.3. In high strength MFC gels, however, the whole microstructure was deformed elastically, indicated by the linear decay of strain across the sample height. The deformation of fiber networks is relatively uniform in its response to applied gravitational stress during compression in high concentration MFC gels.

A summary of the regimes of collapse behavior is mapped in Figure 4.5 as a function of gravitational stress and MFC concentration. The value of gravitational stress,  $\sigma_g$ , plotted here is the maximum stress at the bottom of each sample. Open symbols and cross symbols represent poroelastic compression and fast yielding, respectively, in Figure 4.3 based on assignment from quantitative fits to sedimentation dynamics. The bulk yield stress of MFC gels,  $\sigma_y$ , underestimates the suspension ability of the gels, solid line in Figure 4.5. MFC gels compressed poroelastically,

though the  $\sigma_g$  on the networks is larger than gel  $\sigma_y$ . Instead, the gravitational stress, related to the gel suspension stress (dash line), decides the regime of collapse behavior. When the  $\sigma_g$  is higher than the  $\sigma_s$ , the gels yield and collapse quickly. However, if the  $\sigma_g$  is smaller than gel  $\sigma_s$ , samples compress elastically. The boundary to fast yielding indicates the maximum ability of gels to suspend particles without significant structure failures, which can be successfully predicted by gel suspension yield stress.

Overall, the bulk sedimentation dynamics of MFC gels under accelerated gravity were governed by the competition between gel suspension yield stress and maximum gravitational stress, while the microstructure deformation is dominated by local gravitational stress. The yielding of fiber networks does not necessarily occur over the entire gel structure in these systems, even those experiencing fast collapse. More specifically, if  $\sigma_g < \sigma_s$ , the overall microstructure was compressed poroelastically, while if  $\sigma_g > \sigma_s$ , the fiber network ruptured at the bottom and compressed on the top without any delay time. However, in colloidal gels of Brownian spheres, microstructure erosion controls changes of the gel structure, and a delay time is always observed before either compression or sudden collapse. Similar to gels composed of spherical particles, the rate of initial collapse of sparse gels with fibers is dominated by the back-flow of interstitial fluid, independent of the overall collapse dynamics.<sup>6</sup> All initial collapse rates for the tests performed here are consistent with the critical deformation rate determined via bubble microrheology to allow interstitial flow in MFC networks,<sup>19,21</sup> further supporting the theory of back-flow controlled initial collapse rates in our experiments. This also provides a unique opportunity for additional characterization of these networks during a collapse experiment. By analyzing the rate of initial collapse, the permeability of sparse networks can be quantified.

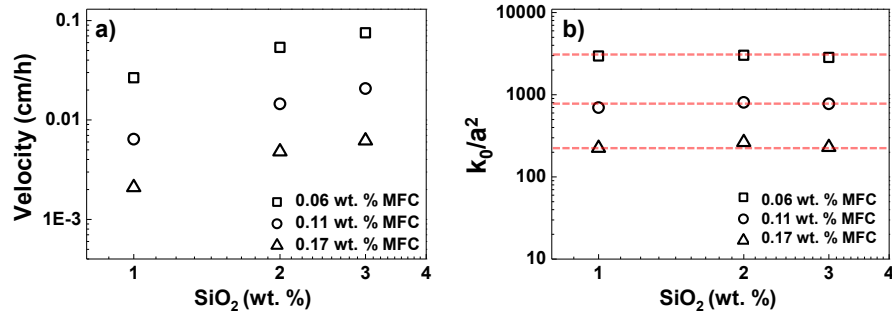


**Figure 4.6:** (a) The velocity of initial interface sedimentation increased linearly under high gravitational stress with more load. (b) Dimensionless permeability of fiber networks is independent of the amount of SiO<sub>2</sub> load, and the values reduce with increasing MFC concentrations.

Permeability,  $k_0$ , is an intrinsic property critical to set the rate of fluid flow through a porous structure. In fibrous media,  $k_0$  depends on the fiber size, concentration and arrangement.<sup>38</sup> Without considering fiber orientation,  $k_0$  can be connected to fiber volume fraction,  $\phi$ , and the radius of the fibers,  $a$ , by:

$$f(\phi) = \frac{k_0}{a^2} \quad (4.7)$$

Using the theory of gel collapse<sup>6</sup>, we can back-calculate the dimensionless gel permeability from the initial collapse dynamics:

$$\frac{k_0}{a^2} = -\frac{\eta_s v_0}{(\rho_p - \rho_s) g \phi_p} \quad (4.8)$$

where  $\eta_s$  is the viscosity of background fluid and  $v_0$  is the initial collapse velocity. Using the calculated gel permeability values at three fiber concentrations, under different gravitational loads, the permeability is determined from the initial linear collapse velocity, Figure 4.6a, and shown to be nicely independent of the applied load, Figure 4.6b. Although dense suspended particles increase gravitational stress and the rate of back-flow, they did not significantly affect the dominant porosity

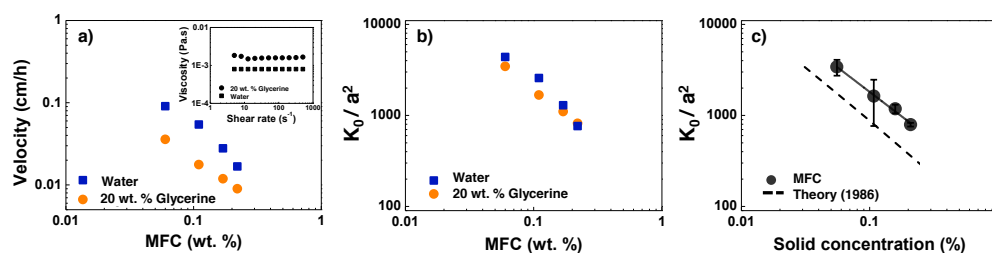


**Figure 4.7:** (a) The velocity of collapse reduced as background fluid viscosity increased (inset). (b) The calculated permeability of the fiber networks is essentially the same for the two different fluid systems when continuous phase viscosity is accounted for (c) The calculated permeability scales similarly to theory for random fiber packings.<sup>38</sup>

of the fiber networks. However, small increases in fiber concentration significantly reduce the size of pores, making the microstructure is less permeable to fluids.

For a given permeability of a porous medium, the rate of fluid flow will be determined by driving force and fluid viscosity, seen from Equation 4.8. This presents another opportunity to apply these findings as a means of designing formulated products. Increasing the viscosity of the gel background fluid provides a simple to controllably reduce the initial gel collapse rate, regardless of the regime of behaviour. This assertion was tested by replacing the water of previous samples with a 20 wt.% aqueous solution of glycerine to increase the continuous phase viscosity without significantly affecting fiber interactions or network strength. The change increased the background viscosity to  $\sim 1.6$  mPa.s, around twice that of the water, Figure 4.7a (inset plot). The rate of initial collapse of the glycerine-containing MFC gels was slowed down by a similar factor as a result of the background fluid viscosity increase, Figure 4.7a. Using the measured viscosity of glycerine solution, the permeability of gels was rescaled and shown to agree quite well with the initial water dispersion permeability, Figure 4.7b. The experiment validates the measurement of fibrous network permeability using this accelerated gel collapse technique, as well as suggesting a way to design gel collapse rates in commercial fluids.

In Figure 4.7b, the permeability of MFC gels decreased with fiber concentration following a power law exponent of  $1.1 \pm 0.4$ , which is relatively consistent for data on fractal gels of spheres<sup>6</sup> and rods<sup>39</sup>. Figure 4.7c indicates the dimensionless permeability of MFC gels is reasonably close to theory and simulations of fluid flow through random fiber packings,<sup>38,40,41</sup> though the larger magnitude of our data may be the result of fiber polydispersity or structural heterogeneities in our fiber samples.<sup>38,41–44</sup>

## 4.4 Conclusions

The collapse of colloidal gels of attractive fibers was studied at volume fractions significantly smaller than previously studied for spherical particle gels. Adding known dense particle loads to a colloidal gel applies controlled gravitational stress that can be used to quantitatively characterise long-term collapse behaviour. Two types of bulk collapse are observed, depending on relative particle load stress and gel yield stress: yielding collapse or creep collapse. Yielding collapse occurs when the stress capacity of a gel is smaller than the applied gravitational stress, and a lower region of the gel fails. Overall linear collapse kinetics are then observed at a rate determined by fluid back-flow, followed by a slower poroelastic compression in the upper region of the sample. Only the latter elastic compression stage was observed when the gravitational load on the gel did not exceed the gel yield stress.

There were no delay times before collapse began in both regimes, another distinction from behaviour of colloidal gels of spherical particles. We expect the microstructure rearrangement of non-Brownian gels composed of fibers is dominated by external stress, rather than the thermal dynamics predominant for delayed collapse in gels composed of spheres<sup>8</sup>.

The use of controlled loads to assess gel collapse is a general approach that enables characterisation of other gel properties as well. The MFC gel permeability was calculated here using the back-flow dominated data, and was shown to be consistent with theories of fluid flow through fibrous packings. Since the rate of back-flow is inversely proportional to continuous phase viscosity, it was also shown that modification of the suspending fluid viscosity allowed straightforward tuning of the collapse kinetics, reducing its rate by a factor of two to ten times. The approach studied here is expected to be useful to both simulation of gel collapse and practical design of commercial suspension products by linking measurable physical parameters to the desired shelf-life and time scale of product stability against sedimentation.

## 4.5 References

- [1] Y. M. Joshi, *Annu Rev Chem Biomol Eng* **2014**, *5*, 181–202.
- [2] C. P. Johnson, X. Li, B. E. Logan, *Environ. Sci. Technol.* **1996**, *30*, 1911–1918.
- [3] P. Laxton, J. Berg, *J. Colloid Int. Sci.* **2005**, *285*, 152–157.
- [4] J. Y. Huh, M. L. Lynch, E. M. Furst **2007**, *76*, 51409.
- [5] G. J. Kynch, *J. Chem. Soc. Faraday Trans* **1952**, *48*, 166–176.
- [6] S. Manley, J. Skotheim, L. Mahadevan, D. A. Weitz, *Phys. Rev. Lett* **2005**, *94*, 218302.
- [7] P. Bartlett, L. J. Teece, M. A. Faers, *Phys. Rev. E* **2012**, *85*, 021404.
- [8] R. Harich, T. Blythe, M. Hermes, E. Zaccarelli, A. Sederman, L. F. Gladden, W. Poon, *Soft Matter* **2016**, *12*, 4300–4308.
- [9] S. B. Lindström, T. E. Kodger, J. Sprakel, D. A. Weitz, *Soft Matter* **2012**, *8*, 3657–3664.
- [10] C. Kim, Y. Liu, A. Kühnle, S. Hess, S. Viereck, T. Danner, L. Mahadevan, D. A. Weitz, *Phys. Rev. Lett* **2007**, *99*, 028303.
- [11] J. Sprakel, S. B. Lindström, T. E. Kodger, D. A. Weitz, *Phys. Rev. Lett* **2011**, *106*, 248303.
- [12] J. D. Park, K. H. Ahn, S. J. Lee, *Soft Matter* **2015**, *11*, 9262–9272.

- 
- [13] L. J. Teece, J. M. Hart, K. Y. N. Hsu, S. Gilligan, M. A. Faers, P. Bartlett, *Colloids Surf. A* **2014**, *458*, 126–133.
- [14] D. Senis, C. Allain, *Phys. Rev. E* **1997**, *55*, 7797.
- [15] D. Bonn, H. Kellay, M. Prochnow, K. Ben-Djemaa, J. Meunier, *Science* **1998**, *280*, 265–267.
- [16] P. J. Skrzyszewska, J. Sprakel, F. A. de Wolf, R. Fokkink, M. A. Cohen Stuart, J. van der Gucht, *Macromolecules* **2010**, *43*, 3542–3548.
- [17] G. Brambilla, S. Buzzaccaro, R. Piazza, L. Berthier, L. Cipelletti, *Phys. Rev. Lett* **2011**, *106*, 118302.
- [18] H. Emady, M. Caggioni, P. Spicer, *J. Rheol* **2013**, *57*, 1761–1772.
- [19] J. Song, M. Caggioni, T. M. Squires, J. F. Gilchrist, S. W. Prescott, P. T. Spicer, *Rheologica Acta* **2019**, *58*, 217–229.
- [20] H. C. de Cagny, B. E. Vos, M. Vahabi, N. A. Kurniawan, M. Doi, G. H. Koenderink, F. C. MacKintosh, D. Bonn, *Phys. Rev. Lett* **2016**, *117*, 217802.
- [21] J. Song, M. Caggioni, T. M. Squires, J. F. Gilchrist, S. W. Prescott, P. T. Spicer, *Rheologica Acta* **2019**, *58*, 231–239.
- [22] S. J. Veen, A. Kuijk, P. Versluis, H. Husken, K. P. Velikov, *Langmuir* **2014**, *30*, 13362–13368.
- [23] A. Kuijk, R. Koppert, P. Versluis, G. van Dalen, C. Remijn, J. Hazekamp, J. Nijse, K. P. Velikov, *Langmuir* **2013**, *29*, 14356–14360.
- [24] L. Hough, M. Islam, B. Hammouda, A. Yodh, P. Heiney, *Nano letters* **2006**, *6*, 313–317.
- [25] J. Schindelin, I. Arganda-Carreras, E. Frise, V. Kaynig, M. Longair, T. Pietzsch, S. Preibisch, C. Rueden, S. Saalfeld, B. Schmid *et al.*, *Nat. Methods* **2012**, *9*, 676.
- [26] C. A. Schneider, W. S. Rasband, K. W. Eliceiri, *Nat. Methods* **2012**, *9*, 671.
- [27] L. Starrs, W. Poon, D. Hibberd, M. Robins, *J. Phys. Condens. Matter* **2002**, *14*, 2485.
- [28] C. J. Dimitriou, G. H. McKinley, *Soft Matter* **2014**, *10*, 6619–6644.
- [29] P. Moller, A. Fall, V. Chikkadi, D. Derks, D. Bonn, *Philos. Trans. Royal Soc. A* **2009**, *367*, 5139–5155.

## References

---

- [30] A. Beris, J. Tsamopoulos, R. Armstrong, R. Brown, *J. Fluid Mech.* **1985**, *158*, 219–244.
- [31] C. C. Sun, *J. Pharm. Sci* **2005**, *94*, 2132–2134.
- [32] Z. Varga, J. L. Hofmann, J. W. Swan, *Journal of Fluid Mechanics* **2018**, *856*, 1014–1044.
- [33] P. L. Chandran, V. H. Barocas, *J. Biomechanical Eng* **2004**, *126*, 152–166.
- [34] A. M. Stein, D. A. Vader, D. A. Weitz, L. M. Sander, *Complexity* **2011**, *16*, 22–28.
- [35] I. Balberg, C. Anderson, S. Alexander, N. Wagner, *Phys. Rev. B* **1984**, *30*, 3933.
- [36] A. R. Wufsus, K. Rana, A. Brown, J. R. Dorgan, M. W. Liberatore, K. B. Neeves, *Biophys. J* **2015**, *108*, 173–183.
- [37] S. Motte, L. J. Kaufman, *Biopolymers* **2013**, *99*, 35–46.
- [38] G. W. Jackson, D. F. James, *The Canadian Journal of Chemical Engineering* **1986**, *64*, 364–374.
- [39] A. Mohraz, D. B. Moler, R. M. Ziff, M. J. Solomon, *Phys. Rev. Lett* **2004**, *92*, 155503.
- [40] L. Spielman, S. L. Goren, *Environ. Sci. Technol* **1968**, *2*, 279–287.
- [41] P. Soltani, M. S. Johari, M. Zarrebini, *Powder Technology* **2014**, *254*, 44–56.
- [42] A. Tamayol, K. Wong, M. Bahrami, *Phys. Rev. E* **2012**, *85*, 026318.
- [43] A. Tamayol, M. Bahrami, *Phys. Rev. E* **2011**, *83*, 046314.
- [44] D. Shou, J. Fan, F. Ding, *Int. J. Heat Mass Transf* **2011**, *54*, 4009–4018.

## Chapter 5

# Enhancing surface coating by adding a small yield stress to fluids with microfibrinous cellulose

### 5.1 Introduction

Surface coatings find a range of applications in daily life, including painting, hand washing, and even drug delivery. The active components, such as pigments and drugs, are commonly dispersed in an aqueous phase, and then shear stress applied during application coats the target surfaces.<sup>1,2</sup> The stability and thickness of liquid films formed on the surfaces after the shear stress is removed are strongly associated with product performance. For instance, increasing the thickness of sprayed films formed in the nasal cavity can increase delivery of an anti-inflammatory drug dose.<sup>3-5</sup>

In a traditional coating process, the contact time and length of liquids on the surfaces are critical. Enhancing the spreadability and wettability of the fluid on the surface could effectively increase the coating efficiency.<sup>6,7</sup> For instance, the polymer additives could increase the contact time of aqueous liquid on a hydrophobic surface, like pea leaves, preventing the rebounding of droplets and resulting in a higher deposition.<sup>8,9</sup> When the size of the droplet is smaller than the capillary length, the film thickness is dominated by surface energy. In contrast, the large sample sizes

---

This chapter originally published as Young, P. M.; Traini, D.; Ong, H.; Granieri, A.; Zhu, B.; Scalia, S.; Song, J. & Spicer, P. T. "Novel nano-cellulose excipient for generating non-Newtonian droplets for targeted nasal drug delivery" *Drug development and industrial pharmacy*, **2017**, 43, 1729-1733

will flat the fluid on the surface, and the eventual film thickness is determined from the balance between surface energy and gravity.<sup>10</sup> If the coating process includes a run-off stage, the rheological properties of fluids play some critical roles. For example, the application of thixotropic fluid can prevent flowing quickly after the shear removed, and thus increasing fluid retention on the surfaces. A fluid that continues to flow after application results in non-uniform coating and some undesirable performance, such as fluid dripping.<sup>11</sup> A traditional approach to offset dripping is to incorporate “thickening” polymers into the formulations to increase viscosity and slow down the flow. Common thickening polymers include hydroxyl-propyl-methyl-cellulose (HPMC), polyethylene glycol (PEG) and proprietary blends of microcrystalline cellulose (MCC), and carboxymethylcellulose sodium (CMC), for instance.

Highly thickened fluids, however, have negative impacts on fluid spreadability, and higher energy is required to shear and apply the materials in the coating process. In addition, viscous fluids only slow down flow and do nothing to halt fluid flow as it is ultimately desired. Introducing a yield stress to fluids provides a more effective way to stop flow immediately after application. Fluid yield stress is the minimum stress that can cause a fluid to begin to flow. While very viscous fluids begin to flow under any value of stress, yield stress fluids act as elastic solids until a threshold stress, or larger, is applied. The restoration of fluid microstructure after shear is removed can “re-solidify” the fluid and resume its total resistance to flow. The quick re-building of fluid microstructures can immediately prevent the flow and ensure the thick film formation on the surface, before the liquid run away. While some polymer thickeners can impart a yield stress to a fluid, the resulting high viscosity that accompanies is too high for common application methods like spraying.

We explore here a novel material that can add a yield stress to a formulation but with minimum effects on the viscosity, providing a substitute for more commonly used additives. Microfibrillar cellulose (MFC) is an alternative form of cellulose to those more commonly used in formulation, having higher purity and mechanical strength as well as more nanoscale dimensions, with a width of around 50 nm and lengths of 1 – 10  $\mu\text{m}$ , creating sparse elastic networks with low viscosity.<sup>12-15</sup> Optimal use of MFC can potentially stop flow after application, without harming the spreading and spraying, and improve the retention of the coating long-term, all at low levels of use.

This chapter investigates the novel use of MFC fibers to generate aqueous liquid films on surfaces. We find that MFC dispersions are highly shear-thinning, with a viscosity close to water at high shear rates, resulting in minimal effects on spreading properties. The existence of a yield stress, and the quick formation of microstructure after removal of shear, contributes to formation of a thicker film on surfaces versus systems with only increased viscosity, such as aqueous HPMC. We propose MFC as a potential additive for use in numerous commercial formulations, including nasal sprays, paints, and other surface coatings.

## **5.2 Experimental methods**

### **5.2.1 Sample preparation**

MFC was prepared from bacterial cellulose cubes (Wong Coco, Indonesia). Cubes were first rinsed multiple times in deionized water (Merck Millipore, Bayswater, VIC, Australia) to remove any non-cellulosic contaminants. Dispersions were then prepared using mechanical disruption in a laboratory blender (Sunbeam, Australia) followed by 5 minutes homogenization (T18 digital ULTRA-TURRAX homogenizer,

IKA). The solids level of every feedstock was determined by gravimetric measurement, and subsequent dilution with deionized water was then used to prepare different concentrations used in this study. Molecular dispersions of HPMC (~ 26 kDa, 80-120 cP, 2% in water, Sigma, Australia) were prepared in deionized water in the following concentrations: 0.2%, 0.5%, 1.0% and 1.8% w/w.

### **5.2.2 Fiber network observation**

The morphology of the cellulose was observed by a scanning electron microscope (FEI Nova NanoSEM 450FE-SEM, Tokyo, Japan) at a number of magnifications, using 5 kV accelerating voltage. 100  $\mu$ L of the 0.01% w/w cellulose suspension was first dropped onto a silicone waver that was subsequently placed on adhesive black carbon tape. After that, the sample was dried in an oven overnight at 50 °C and then gold coated with a sputter coater (BAL-TEC SCF 005, Tokyo, Japan) for SEM imaging.

### **5.2.3 Rheological characterization**

The rheological characteristics of the MFC dispersions were evaluated using a stress-controlled rheometer (AR-1500 EX, TA instruments) with a cone and plate geometry (60 mm, 2°). All measurements were performed at 25 °C and after a 30 s pre-shear and a 2 min relaxation period. The flow curves of fluids were studied using a steady state flow with a shear rate decreasing from 1000  $s^{-1}$  to 1  $s^{-1}$ . The dynamic yield stress was determined by fitting to the Herschel-Bulkley model, above a critical shear rate that allows relatively homogeneous flow.<sup>16</sup> The response time of the fluids to the external stress or flow was measured by step-increasing the applied stress for a fixed time, then measuring the rate at which elasticity is recovered, or the fluid reaches a steady state flow.

### 5.2.4 Run-off film thickness measurements

The run-off film thickness of each solution was evaluated by depositing 1 mL of either HPMC or MFC dispersion onto a flat glass microscope slide, which was then oriented to 45° from the horizontal. A Leica Wild M3C (Sydney, Australia) microscope connected to a Moticam 10MP (Causeway Bay, Hong Kong) camera was then used to record the images of the resulting film on the glass slide. Experimental film thickness was measured using ImageJ software.<sup>17</sup> The sizes of initial droplets are much larger than the capillary length of around 2.7 mm.<sup>10</sup>, and there is a run-off stage involved in the experiments. The thickness of the film formed on the surface is mainly governed by the gravity and fluid yield stress:

$$h_i = \frac{\sigma_y}{\rho g \cos\theta} \quad (5.1)$$

where  $h_i$  is the theoretical film thickness,  $\rho$  is the fluid density (1000 kg/m<sup>3</sup>),  $g$  is gravitational acceleration (9.8 m/s<sup>2</sup>),  $\sigma_y$  is the yield stress, and  $\theta$  is the angle of the slope from the vertical (45°).<sup>18</sup>

### 5.2.5 Surface tension measurements

The interfacial tension of the MFC dispersions at different concentrations was measured using a ring tensiometer (TensioCAD, China), and the results were subsequently compared to surface tension measurement of water at room temperature. At least three replicates were performed on each sample.

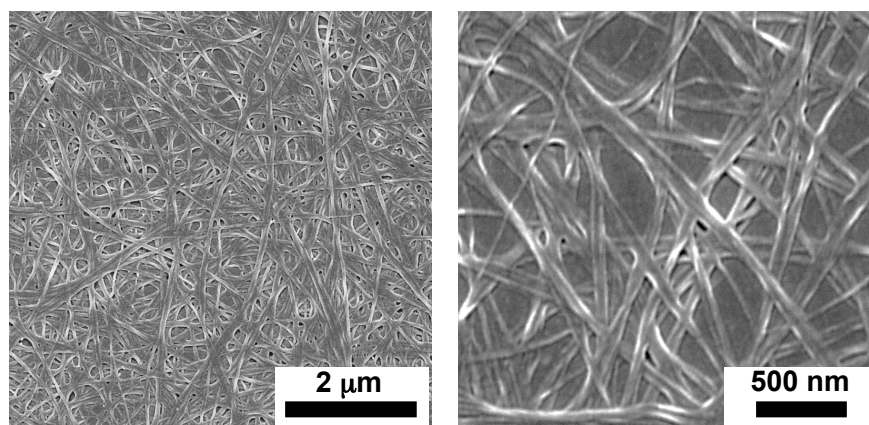


**Figure 5.1:** Scanning electron microscope image of microfibrillar cellulose prepared by drying a 0.01% w/w solution on a silicon wafer.

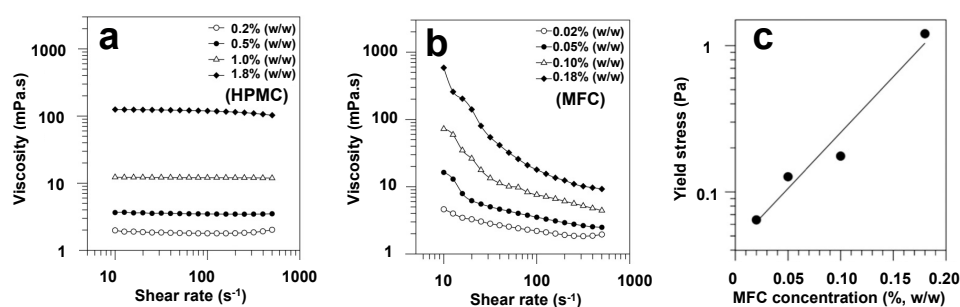


**Figure 5.2:** Viscosity of HPMC (a) and MFC dispersions (b) as a function of shear rate at multiple concentrations. The yield stress of the MFC gel increased as a function of concentration by power law (c), and HPMC dispersions did not exhibit any yield stress in measured concentrations.

### 5.3 Results and discussion

The morphology of cellulose produced from bacterial fermentation is shown in Figure 5.1. The fibers have a width of around 50 nm and a length of more than a few micrometers, resulting in an aspect ratio more than 1000.<sup>19</sup>

The viscosity of HPMC and MFC dispersions as a function of shear rate is shown in Figures 5.2a and 5.2b, respectively. The shear rates are between  $10 \text{ s}^{-1}$  to  $500 \text{ s}^{-1}$  since most surface coating processes, such as painting and delivering drugs into the nasal cavity, occur at high deformation rates.<sup>20</sup> The viscosity of HPMC and cellulose

dispersions both increased at higher solid concentrations. Increasing fluid viscosity can proportionally slow down the rate of fluid flow. However, HPMC dispersions at any given concentration behave as viscous Newtonian fluids, while MFC dispersions are dramatically shear-thinning. For 0.1% MFC dispersions, the viscosity reduced by two orders of magnitude when increasing shear rate from  $10\text{ s}^{-1}$  to  $500\text{ s}^{-1}$ . At much higher shear rates, the viscosity of MFC dispersions is expected to approach a value  $\sim 1\text{ mPa}\cdot\text{s}$ , quite close to the viscosity of water at room temperature.

The unique shear-thinning dynamics of MFC dispersions are advantageous for coating processes. For instance, the shear rate applied by conventional nasal spray pumps is estimated to be  $> 10^5\text{ s}^{-1}$ .<sup>20</sup> The low viscosity of MFC dispersions at high shear rates makes them easily spreadable and can lead to improved droplet formation when actuated through a conventional nasal spray.<sup>21</sup> At low shear rates, however, the significantly increased viscosity of MFC dispersions can effectively slow down fluid flow, until its yield stress can halt it.

MFC dispersions possess a yield stress at all concentrations studied here. The dynamic yield stress increased by a power law correlation with increasing cellulose concentrations, Figure 5.2c, indicating the significant contributions of small amounts of fibers to the network strength.<sup>22</sup> In comparison, HPMC dispersions did not exhibit any yield stress at concentrations below 2%, though it can effectively increase viscosity, Figure 5.2a. Interaction and aggregation of long MFC fibers can form sparse networks at low concentrations, and the resulting yield stress in fluids can effectively prevent flow. However, the HPMC particles are unlikely to build self-supported networks at low concentrations, and thus only alter fluid flow by modifying viscosity.

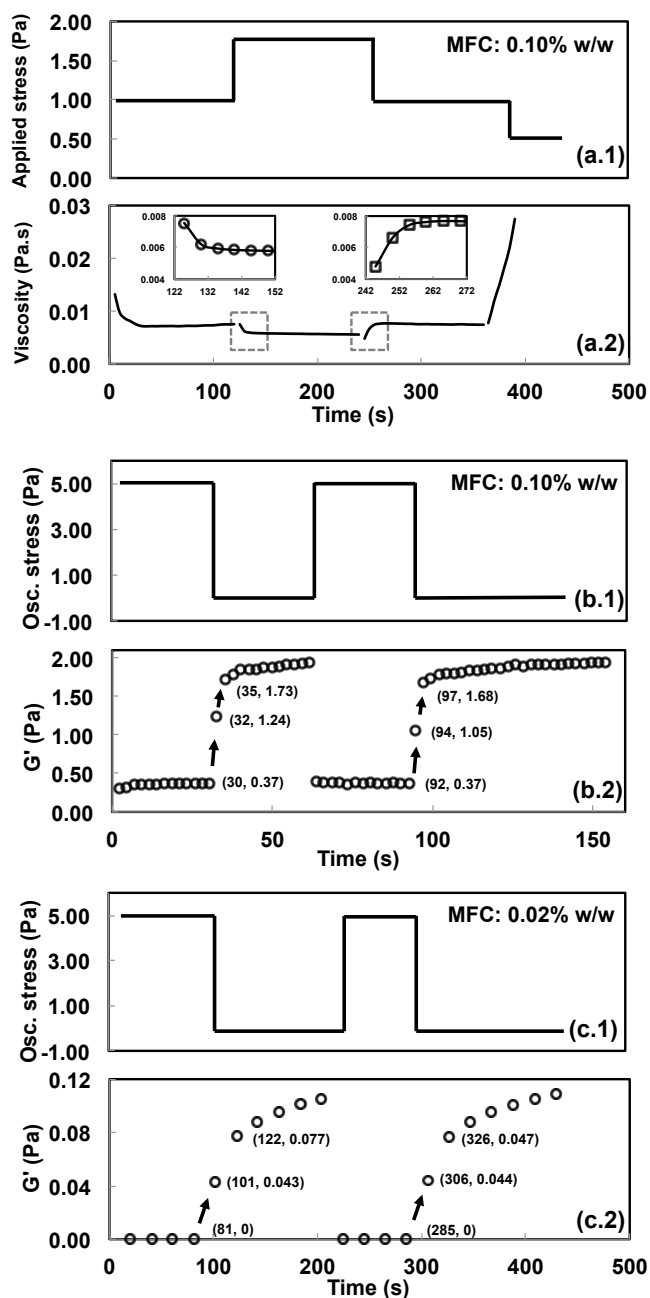


**Figure 5.3:** The viscosity response time of 0.10% cellulose dispersion is less than 5 s after a sudden increase or decrease in applied stress (a.1 and a.2). Elasticity of a 0.10% MFC dispersion regrows quickly, within 5 s, after a large oscillatory stress was suddenly removed in a step-wise oscillation measurement at a frequency of 1 Hz (b.1 and b.2), while the samples of lower MFC concentrations, like 0.02%, take more than 10 s to reform fiber networks. The continuous growth of elasticity indicates network rearrangement under small deformations.

The thixotropy of cellulose gels demonstrates how quickly the network can rearrange, and was also evaluated by step-stress measurements,<sup>16,23</sup> Figure 5.3. The fast reformation of fiber networks after removal of shear can significantly benefit liquid film deposition on a surface. Figures 5.3a.1 and 5.3a.2 show the sudden changes of applied stress and response of the fluid viscosity as a function of time. Since the applied stresses are higher than the gel yield stress, the fluids flow under these conditions. Figure 5.3a.2 indicate that, after a sudden increase in applied stress, the viscosity decreased due to shear-thinning, rapidly reaching a constant, steady-state value. The response time of the viscosity of 0.1% MFC gel is seen to be less than 5 s as a result of relatively quick re-arrangement of fiber networks.

More direct measurement of microstructure recovery after yielding is performed via small oscillatory tests, Figures 5.3b.1-5.3b.2 and Figures 5.3c.1-5.3c.2. The initial applied oscillatory stress, 5 Pa lasting for more than 20 s, was higher than the gel yield stress, ensuring the break-down of fiber networks to a gel elasticity,  $G'$ , near zero. After a sudden decrease of oscillatory stress to 0.1 Pa, lower than the gel yield stress,  $G'$  values increased and reached a plateau value of around 1.7 Pa for 0.1% cellulose gel. The growth of  $G'$  indicates the reformation of networks, and the response time for 0.1% MFC gel is between 2 s to 5 s, which is consistent with the results found for large-amplitude flow in Figures 5.3a.2.

However, for low concentration MFC gels of 0.02%, the oscillatory measurements show that the reformation of fiber networks took around 10 s, and the small applied oscillatory stress induced a continuous growth of  $G'$ , Figure 5.3c.2. The continued growth of  $G'$  may result from the sparse fiber network rearranging into a denser structure with time, a behavior we have recently observed in MFC networks at low deformation rates.<sup>14,15,24,25</sup> Microstructure re-arrangement in sparse fiber

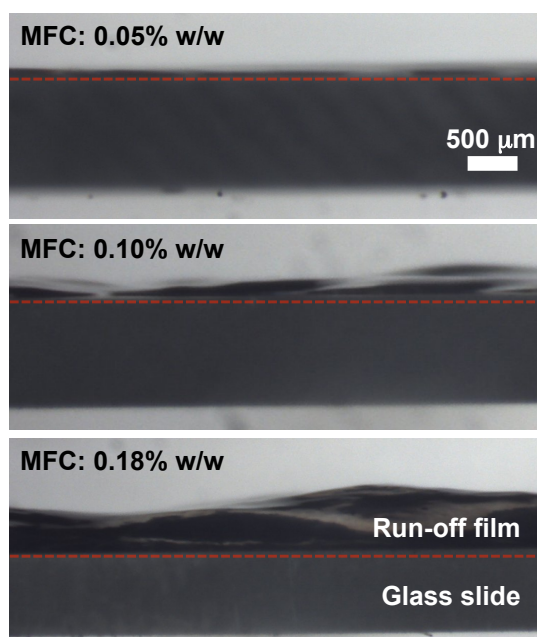


**Figure 5.4:** Microscopy images of films remaining after bulk run-off experiments for MFC dispersion on a glass surface. The dashed lines indicate the position of the surface of the glass slide.

networks can enhance gel strength and is potentially advantageous for retention of thick films after formation on surfaces.

The film thickness of MFC and HPMC dispersions was explored by flowing fluids on a glass slide surface. At all concentrations, the majority of HPMC fluids run off the glass surface, leaving a very thin liquid film on the surface. The thickness of run-off film for HPMC dispersion is difficult to image as a result of the limited imaging resolution. However, MFC dispersions left relatively thick films on the glass surface after running off, Figure 5.4. Although significantly larger than the films formed by HPMC, the MFC films were often uneven, potentially due to the some fluid heterogeneity or thixotropy-induced non-uniformity.<sup>14</sup>

The above experiments indicate that the viscosity of the fluid is not the relevant property for enhancing coating thickness, as high viscosity merely slows down the flow, for example in HPMC dispersion. Instead, it is the fluid yield stress that is

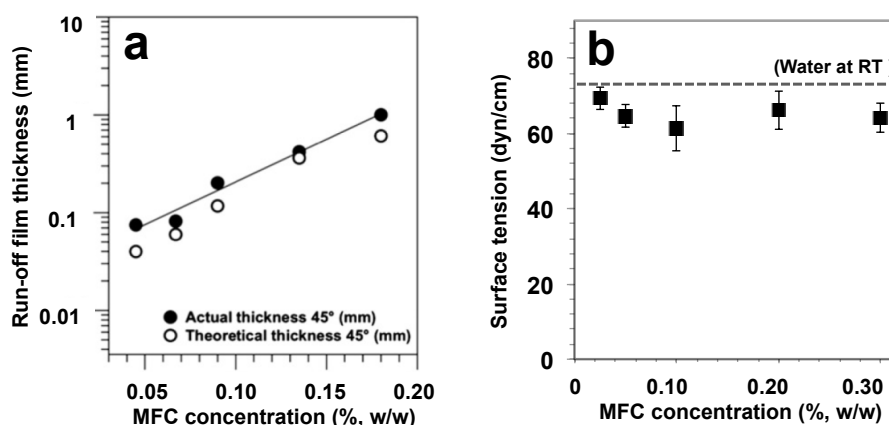


**Figure 5.5:** (a) Run-off film thickness increased with increasing MFC concentrations, and the values are higher than the theoretical prediction at the measured yield stress. (b) The surface tension of MFC dispersions is slightly lower than water.

responsible for the significant coating benefits observed for the MFC gels. In MFC dispersions, the fluid does not flow at all when stresses are below the yield stress. Therefore, MFC can dramatically benefit some surface coating processes that require more considerable deposition, enhanced residence time, and minimum run-off. For example, MFC was reported as a superior excipient for formulating stable nasal sprays with consistent droplet size and enhanced deposition in the nasal cavity.<sup>21</sup>

The run-off film thickness for MFC dispersions as a function of concentration is compared with the theoretical estimation, using Equation 5.1 in Figure 5.5a. MFC dispersions can generate liquid films on a surface with limited run-off, increasing from around 0.1 mm thick at 0.05% to almost 1 mm thick at 0.18%. The experimental results agree well with the theoretical prediction, though a small deviation was observed with the actual film thickness values higher than theoretical values at small MFC concentrations. It is likely that at low MFC concentrations, the surface tension of the solution can dominate the coating process instead of rheology effects. The surface tension of MFC dispersion, however, is slightly lower than water at room

temperature, Figure 5.5b. Therefore, we conclude the existence of yield stress in MFC gels leads to thick liquid film formation on the surface.

## 5.4 Conclusions

The use of microfibrinous cellulose materials with very high aspect ratios can generate a thicker liquid film on a surface than traditional thickening additives, primarily due to the formation of a yield stress. The quick recovery of networks after application, in 5 s, can prevent flow and enhance coating. MFC dispersions are highly shear-thinning, possessing a small viscosity at high rates, allowing easy flow and spraying. In contrast, conventional additives create thick and stable liquid films that can not halt flow after applications. Therefore, MFC can provide a replacement for some thickeners to enhance surface coating processes by halting flow, for example in nasal spray. Further exploring the responses of MFC droplets in more controlled spreading processes, such as impacting drops and forced coating, could promote the understanding and applications of MFC fluid coatings on surfaces. More tests of fluid deposition on realistic surfaces and geometry are also required in future studies.

## 5.5 References

- [1] M. Pozzoli, H. X. Ong, L. Morgan, M. Sukkar, D. Traini, P. M. Young, F. Sonvico, *European Journal of Pharmaceutics and Biopharmaceutics* **2016**, *107*, 223–233.
- [2] S. Patil, A. Babbar, R. Mathur, A. Mishra, K. Sawant, *Journal of drug targeting* **2010**, *18*, 321–331.
- [3] M. Koźmiński, M. Kupczyk, *Advances in Respiratory Medicine* **2015**, *83*, 157–163.
- [4] R. Bacon, S. Newman, L. Rankin, G. Pitcairn, R. Whiting, *International journal of pharmaceutics* **2012**, *431*, 39–44.

- 
- [5] S. V. Dhuria, L. R. Hanson, W. H. Frey II, *Journal of pharmaceutical sciences* **2010**, *99*, 1654–1673.
- [6] F. Brochard-Wyart in *Soft matter physics*, Springer, **1999**, pp. 1–46.
- [7] Y. C. Jung, B. Bhushan, *Langmuir* **2008**, *24*, 6262–6269.
- [8] M. Smith, V. Bertola, *Physical review letters* **2010**, *104*, 154502.
- [9] V. Bergeron, D. Bonn, J. Y. Martin, L. Vovelle, *Nature* **2000**, *405*, 772–775.
- [10] P.-G. De Gennes, *Reviews of modern physics* **1985**, *57*, 827.
- [11] W. E. Berger, J. W. Godfrey, A. L. Slater, *Expert opinion on drug delivery* **2007**, *4*, 689–701.
- [12] S. J. Veen, A. Kuijk, P. Versluis, H. Husken, K. P. Velikov, *Langmuir* **2014**, *30*, 13362–13368.
- [13] D. Klemm, F. Kramer, S. Moritz, T. Lindström, M. Ankerfors, D. Gray, A. Dorris, *Angewandte Chemie International Edition* **2011**, *50*, 5438–5466.
- [14] J. Song, M. Caggioni, T. M. Squires, J. F. Gilchrist, S. W. Prescott, P. T. Spicer, *Rheologica Acta* **2019**, *58*, 231–239.
- [15] J. Song, M. Caggioni, T. M. Squires, J. F. Gilchrist, S. W. Prescott, P. T. Spicer, *Rheologica Acta* **2019**, *58*, 217–229.
- [16] P. C. Møller, J. Mewis, D. Bonn, *Soft matter* **2006**, *2*, 274–283.
- [17] C. A. Schneider, W. S. Rasband, K. W. Eliceiri, *Nature methods* **2012**, *9*, 671.
- [18] P. Coussot, *Rheometry of pastes, suspensions, and granular materials: applications in industry and environment*, John Wiley & Sons, **2005**.
- [19] D. W. De Kort, S. J. Veen, H. Van As, D. Bonn, K. P. Velikov, J. P. Van Duynhoven, *Soft Matter* **2016**, *12*, 4739–4744.
- [20] J. Pennington, P. Pandey, H. Tat, J. Willson, B. Donovan, *Drug development and industrial pharmacy* **2008**, *34*, 923–929.
- [21] P. M. Young, D. Traini, H. X. Ong, A. Granieri, B. Zhu, S. Scalia, J. Song, P. T. Spicer, *Drug development and industrial pharmacy* **2017**, *43*, 1729–1733.
- [22] M. J. Solomon, P. T. Spicer, *Soft Matter* **2010**, *6*, 1391–1400.
- [23] P. Møller, A. Fall, D. Bonn, *EPL (Europhysics Letters)* **2009**, *87*, 38004.

## References

---

- [24] P. Lopez-Sanchez, J. Cersosimo, D. Wang, B. Flanagan, J. R. Stokes, M. J. Gidley, *PLoS one* **2015**, *10*, e0122132.
- [25] H. Emady, M. Caggioni, P. Spicer, *Journal of Rheology* **2013**, *57*, 1761–1772.

## Chapter 6

### Soft bacterial cellulose microcapsules with adaptable shapes

#### 6.1 Introduction

Microcapsules have been widely applied as vehicles for encapsulation, protection and controlled release of various substances, such as pharmaceuticals, flavours and cells.<sup>1-3</sup> Critical characteristics of microcapsules are membrane permeability, mechanical stability and adhesion properties. The porosity of microcapsules determines the size and speed of the contents' exchange with the bulk environment. Most artificial microcapsules are designed for slow release of their contents. A strong shell is able to provide a robust protective barrier for the encapsulated contents and increase the stability of microcapsules under flow and deformation. Soft particles increase interactions with cells<sup>4</sup> and enhance targeted delivery, enabling transport into organs that would block hard particles and extending circulation time.<sup>5</sup>

Many methods of fabricating microcapsules have been developed, including interfacial self-assembly<sup>6-9</sup> and template polymerisation<sup>9-11</sup>. Capsules often have nanoscale pore sizes, but can easily collapse under high osmotic pressure because of limited solute exchange with the bulk environment.<sup>12</sup> However, more open microcapsule structures are sometimes useful, for example to encapsulate fragile cellular cargo while allowing free transport of nutrients.

---

This chapter originally published as Song, J.; Babayekhorasani, E. & Spicer, P. T. "Soft bacterial cellulose microcapsules with adaptable shapes" *Biomacromolecules*, **2019**, 20(12), 4437-4447

Past efforts to increase the stability of microcapsules mainly focused on increased capsule rigidity,<sup>10,13</sup> sometimes achieving strengths as high as 0.5 GPa.<sup>13</sup> However, some “soft” microcapsules also have performance advantages, aiding in adhesion and uptake in cases where particle and cell mechanical properties are important.<sup>4,5</sup> For instance, red blood cells can deform by more than 100% under compression by changing shape but are highly stable against stretching. Folding of pollen grains during drying protects structural integrity while keeping out damaging substances, a key evolutionary adaptation preventing harm to the encapsulated DNA.<sup>14</sup> Soft microcapsules thus offer unique benefits by using elasticity to enable complex shape deformation.<sup>15</sup>

Soft polymeric microcapsules typically have elastic modulus on the order of 1 – 10 kPa and their structure tends to be homogeneous, with mechanical properties consistent with the bulk polymer. As a result, resistance to stretch and rupture is often relative, as materials like poly(ethylene glycol) (PEG) and 2-hydroxyethyl acrylate (HEA) hydrogels can be too soft<sup>5,16</sup> to resist shearing and tearing. A useful step forward would be fabrication of materials with substantial tensile strength as well as a flexible response to deformation, and the key to achieving this is often a novel microstructure.

One material with useful hierarchical mechanical and structural properties is bacterial cellulose, a strong, flexible, and biodegradable fiber that is easily produced via fermentation.<sup>17</sup> *Acetobacter xylinum* synthesizes nanoscale fibers and forms elastic networks at very low concentrations, with densities on the order of 0.01 g/cm<sup>3</sup>.<sup>18–20</sup> Bacterial cellulose is well-studied in its native form and during post-processing, though recent work has explored actively engineering the material as it is being produced by a bacterial culture.<sup>17,21–23</sup> An example is 3D printed materials produced by extruding a cellulose-producing culture medium into soft molds, yielding

complex functional nanocellulose material forms.<sup>24–26</sup> Nanocellulose was also used to reinforce polymer capsules produced via microfluidics,<sup>13</sup> but we are interested here in what sort of capsules could be produced solely by tailoring the bacterial fermentation process in an easily scalable manner.

In this work, we use emulsion droplet interfaces as a passive template for bacterial cellulose growth. During fermentation, the production of cross-linked cellulose networks, constrained by a liquid-liquid interface, forms a unique, hierarchical core-shell structure, and we directly study its properties using 3D confocal microscopy. The cellulose membrane is 10 – 30  $\mu\text{m}$  thick, and the resulting highly porous structure allows rapid exchange of most macromolecules. The microcapsules are soft and flexible, but remarkably stable under shear and deformation. They can easily pass through narrow constrictions by bending and folding without rupturing the membrane structure, and the spherical shape can be fully recovered after compression by as much as 20%.

## 6.2 Experimental methods

### 6.2.1 Materials and microcapsule preparations

*Acetobacter xylinum* was purified and concentrated from Kombucha culture (Nourishme Organics, Australia) by gradient centrifugation. The bacteria were uniformly dispersed in a fermentation medium composed of coconut water (Cocobella, Indonesia), 10% w/v white sugar (Black & Gold, Australia) and 1% w/v phosphate (AJAX chemicals, Australia). Hydrogenated castor oil wax, HCO, was used as an organogelator to produce a yield stress matrix,  $\sigma_y \sim 10$  Pa for emulsion stabilization. The organogel was prepared by dispersing 2.5 g of HCO wax (Acme-Hardesty, USA) into 100 mL of canola oil (Coles, Australia) at 90 °C on a hot plate (Ika-Works, VWR,

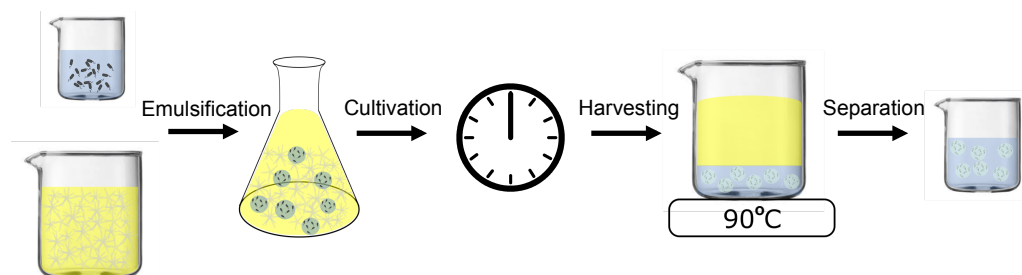


**Figure 6.1:** Schematic diagram showing the process of cellulose microcapsule production: an aqueous *Acetobacter xylinum* bacterial culture (blue) is dispersed into droplets in a gelled oil phase (yellow) and the droplet interfaces used to template bacterial cellulose growth into capsule forms. Melting of the organogelator allows recovery of the capsules and removal of the bacteria.

Australia), and mixing for 10 min until all the wax melts. The system was then cooled in a static state to 25 °C.

Cellulose microcapsules were prepared by growing cellulose in monodisperse emulsion droplets, Figure 6.1. Emulsion droplets can provide a stable environment for bacterial survival and cellulose growth.<sup>27,27-29</sup> A co-flow millifluidic device was used to generate monodisperse water-in-oil emulsion droplets.<sup>11</sup> A capillary (VitroCom, USA), tapered by a micropipette puller (P-97, Sutter Instrument), with tip diameter around 50  $\mu\text{m}$ , was secured into another capillary with an inner diameter of 1 mm. Teflon tubing (IDEX, USA) then connected two capillaries with two 10 mL syringes (BD Plastipak, USA) for sample loading. Water-based media with bacteria flowed through the pulled capillary at 0.02  $\mu\text{m}/\text{s}$  as a dispersed phase, with the continuous phase a 2.5% HCO gel, flowing at 0.2  $\mu\text{m}/\text{s}$ . The speed of the flows was controlled by syringe pumps (WPI 947-371-1003, USA). The emulsion was collected at the end of flow into a glass bottle (Cospak, Australia) and covered to prevent contamination but allow air exchange, for cultivation.

The emulsion was incubated at 25 °C statically for one to two weeks. The shape of the emulsion droplets is templated into microcapsules by the growth of cellulose

and is preserved stably in the water once sufficient cellulose has occurred, typically after one week. In order to release the microcapsules from the oil, some water was first added to the emulsion, followed by heating at 90°C on the hot plate to melt the HCO crystals and remove the yield stress. The liquid oil separated from water at the top, while the cellulose microcapsules settled down into the bottom water phase. The oil was then removed and recycled, leaving pure cellulose microcapsules in water.

Cellulose microcapsule purification is performed by heating at 90°C for two hours to kill the bacteria, that then detach from cellulose and can be washed away in later steps. The samples were then soaked in 2% w/v NaOH (Chem-Supply Pty Ltd, Australia) overnight and washed by deionized water at least three times to remove other impurities completely.

### 6.2.2 Optical microscopy imaging and analysis

Bacteria and HCO crystals were observed using differential interference contrast (DIC) imaging mode on a Nikon Optiphot microscope. The emulsion droplets and cellulose microcapsules were imaged in water using a stereoscope long working distance objective (WILDM3C, Leica, Germany) at low magnification for a large field of view. The images were taken by a digital camera (2.0MP Motic, Europe).

Imaging of fiber networks was performed on a confocal microscope (Leica SP5 WLL gSTED, Germany). A 10× dry objective, with numerical aperture  $NA = 0.3$ , and a 63× oil immersion objective, with  $NA = 1.3$ , were used, respectively. After removing some bacteria and minor impurities, cellulose microcapsules were stained by 1 mg/mL Congo Red (Sigma-Aldrich, USA) solution for 15 min. Congo red dye was excited with a  $\lambda_0 = 496$  nm laser beam. The microcapsules were scanned and im-

aged from their bottom to middle planes to visualize their 3D structure. All images were taken in regions where image brightness is proportional to fiber density.

Microcapsule shell thickness was measured for a sample of multiple capsules by confocal imaging with a 10× air objective, focusing at the middle plane of the microcapsules. The imaging section thickness is around 5 μm, while the diameter of the microcapsules is, on average, larger than 200 μm. Only microcapsule images with a sharp edge, an indication of focusing at the mid-plane position, were used for shell thickness analysis in order to mitigate measurement errors. A thin rectangle was drawn across the middle of each microcapsule image, and the intensity profile was plotted using ImageJ.<sup>30,31</sup> The inner edge of the capsule shell was defined to be the position where the intensity reduced by 80%.

The pore sizes of cellulose capsule membranes were estimated by diffusing 0.5 μm and 1 μm tracer particles (Polyscience, USA) into the capsules. Plain microcapsules were first soaked in the tracer dispersion for at least three hours. The samples were then imaged by a fluorescent microscope (Leica DM2500M, Germany) under a 50× dry objective, focusing on the middle of the microcapsules. The diffusivity of 0.5 μm tracers was measured at two frames per second acquisition rate, and particle tracking was carried out using Matlab routines, from which an ensemble average mean squared displacement (MSD),  $\Delta r^2(\Delta t) = (r(t + \Delta t) - r(t))^2$ , was determined as a function of the lag time,  $\Delta t$ .<sup>32</sup>

### 6.2.3 Elasticity measurements

A polydimethylsiloxane (PDMS) microfluidic device, with a ratio of microchannel width to constriction width of three, was used to measure the elasticity of microcapsules. The device was made by molding PDMS onto a 500 μm thick piece of adhesive tape cut into a microchannel form using a 3D cutter (Silhouette CAMEO,

China). The microchannel mold was then attached to a clean glass slide and put into a glass petri dish for later use. PDMS was prepared by mixing silicone elastomer base and curing agent (Dow corning, USA) at a ratio of 7:1. When all the bubbles rise and disappear, PDMS solution was added into the petri dish to cover the whole microchannel, then heated at 60 °C overnight.

The solid PDMS was then cut, to a size a bit smaller than the glass slide, and removed. After removing the plastic microchannel mold, the solid PDMS was reattached onto a clean glass slide using air plasma treatment (Harrick Plasma PDC-32G) for one minute. Two holes were opened at each end of the channel and connected to tubing (Tygon, Saint-Gobain) serving as inlet and outlet.

The elastic deformation of cellulose microcapsules was achieved by applying an extensional flow using microchannels with the constriction in the middle. The microcapsules were dispersed into 67 wt.% glycerine solution (Chem-Supply Pty Ltd, Australia), a Newtonian fluid with viscosity of  $\eta = 0.04$  Pa.s. The sample was then transferred into a 1 mL syringe (BD Plastipak, USA) connected to a microchannel. A high-speed camera (Phantom, USA) captured the flow of microcapsules in the channel at 10,000 frames per second, from which we can determine the extensional stress, deformation of microcapsules, and the capsule elasticity.<sup>33,34</sup> A shape parameter is used to quantify microcapsule deformation,  $D$ , defined by the difference of large,  $a$ , and small,  $b$ , radii of the spheroid divided by their sum.<sup>35</sup>

The cellulose microcapsule strength was also characterized by capillary micro-mechanics.<sup>36,37</sup> An individual microcapsule was gradually pushed along a tapered microcapillary using a water column to apply step increases in pressure. An in-line pressure sensor (PX409, OMEGA) recorded the applied stress, while the microcapsule deformation was recorded by a microscopic observations.

### 6.2.4 Large-amplitude microcapsule deformation

Manipulators (Narishige International, USA) allowed precise deformation of microcapsules in a fluid with a low yield stress  $\sigma_y \sim 0.1$  Pa, that prevents movement of the microcapsules but not their deformation. The capsules were deformed by pushing against them using microcapillaries with a controlled tapering at their end. Two capillaries compressed the microcapsule for at least 10 s before allowing it to relax. The process was imaged on an inverted microscope (Motic AE31) at one frame per second.

The folding and buckling of microcapsules was studied by extruding them through a pulled capillary with an end diameter of 110  $\mu\text{m}$ . Microcapsules were shaped and elongated as they passed through the constriction at the exit of the capillary.

## 6.3 Results and discussion

Microcapsules were prepared by templated growth of cellulose on emulsion droplets of bacterial dispersions.<sup>27,38</sup> A co-flow microfluidic device, Figure 6.2a, produced droplets of aqueous culture medium containing 3 – 5  $\mu\text{m}$  rod-shaped bacteria, Figure 6.2b, in an HCO-oil gel phase, Figure 6.2c, yielding monodisperse emulsion droplets, Figure 6.2d. The encapsulated bacteria can survive in the droplets for a few weeks and produce microfibril cellulose, though instead of the pellicle produced at the air-liquid interface in traditional cultures<sup>17</sup>, here the fibers grow at the oil-water interface and template the spherical emulsion droplet. After at least one week of static incubation of the emulsion at 25 °C, bacterial cellulose forms isolated microcapsules inside of the droplets that resemble “jellyfish” after re-dispersion in water, Figure 6.2e. The spherical shape and size were maintained by the cross-linked microfibril cellulose structure, Figure 6.2f. The size of the microcapsules

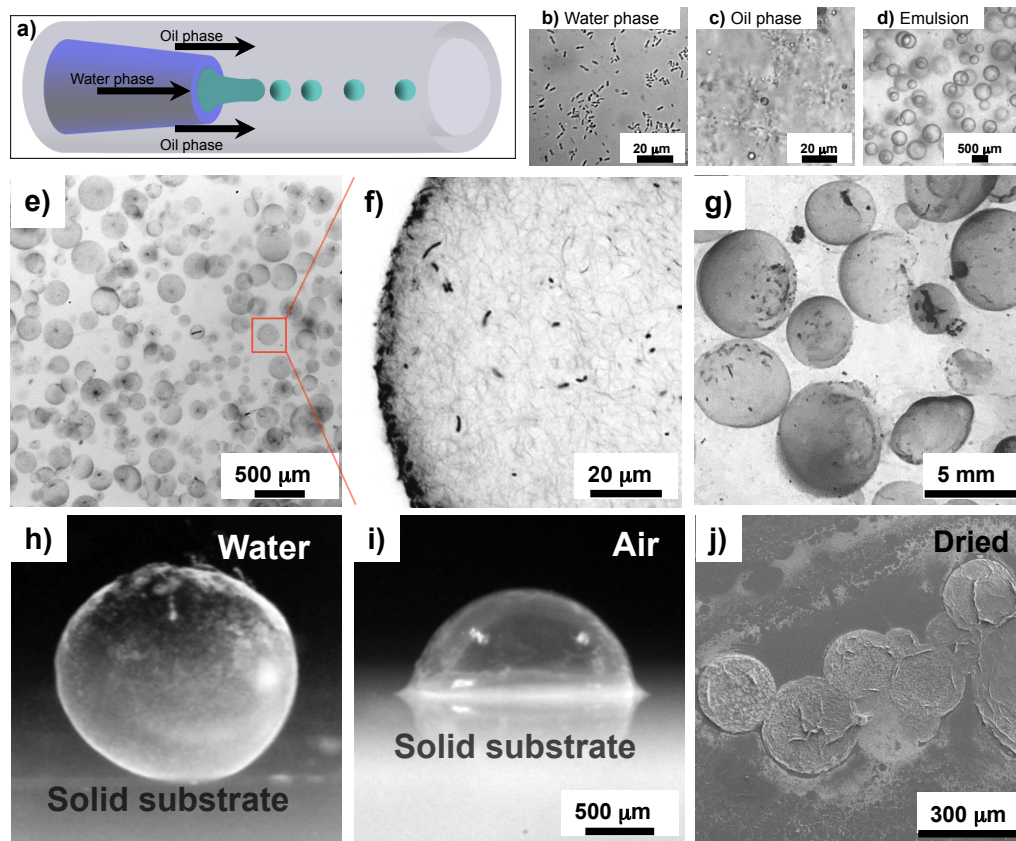


**Figure 6.2:** Bacteria were encapsulated into emulsion droplets created by a co-flow microfluidic device (a), in which bacteria and media (b) flow as a dispersed phase into a continuous phase of 2.5% HCO (c). Emulsion droplets with sizes from 200 μm to 500 μm were collected into vials for cultivation (d). Fiber networks are able to form isolated cellulose microcapsules in water dispersion (e), and the sparse fiber microstructure was observed under the microscope (f). Cellulose capsules can also be produced that are larger than 3 cm (g).

produced is set by the initial droplet size, with a lower limit of 20  $\mu\text{m}$  given the bacterial dimensions, but sizes larger than a few centimeters are easily achieved as well, as shown in Figure 6.2g. The softness of the cellulose microcapsules is illustrated by depositing the particles onto a solid substrate in Figures 6.2h and 6.2i, where the porous capsule is self-supporting in water as a result of its high permeability, but in air is less stable as water evaporates, Figure 6.2i. Full drying of the capsules to remove free water causes complete collapse into a remarkably thin sheet with some folds observed, Figure 6.2j.

In our fermentation conditions, growth times shorter than one week produce capsules with a density of fibers that is too low to fully form an elastic enclosure in water. Increasing the bacteria concentration and the oxygen supply could effectively increase the cellulose productivity, forming stable cellulose microcapsules in a shorter time. Assuming that the water-in-oil interface is comparable with the air-water interface in a bulk bacteria cultivation, we can estimate the volume fraction of bacterial cellulose in the stable capsules to be roughly 0.35% v/v after one week and 0.67% v/v after two weeks of growth, with a shell density on the order of 0.01  $\text{g}/\text{cm}^3$  and a much smaller bulk capsule density. The capsules are therefore highly efficient, given their density is roughly two orders of magnitude smaller than many polymeric and metallic capsule materials, and we are interested in their structure as it will influence applications and mechanical properties.

Figure 6.3 shows confocal microscopy images of sparse cellulose fiber networks in microcapsules after incubating for one and two weeks. The images show slices through the structures at three positions: the bottom, a place between the bottom and middle, and the middle, Figures 6.3 a.1-6.3a.3 (insets). Some remaining bacteria are visible, highlighted with blue coloring to distinguish them from the fibers that are colored black. Nanoscale crosslinked fibers make up the capsules, forming

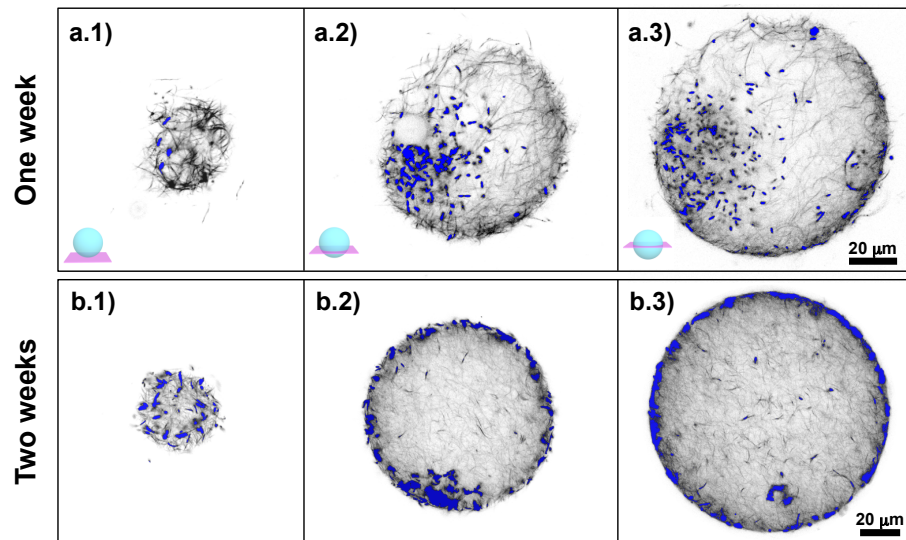


**Figure 6.3:** Two-dimensional confocal slices through the three-dimensional microcapsule structure at different positions indicated by the a.1-a.3 insets. Bacteria are colored blue while fibers are black. Microcapsules have a shell-like fibrous microstructure, with dense fibers at the outside and fewer fibers inside after one week of cultivation (a.1-a.3). More fibers were produced over longer incubation times of two weeks (b.1-b.3). Bacteria are mainly located near the capsule surface but an aggregate of bacteria is often found in the bottom of the capsules as well.

porous networks at the surface and throughout the volume of the capsules, Figures 6.3a.1-6.3b.3. The scan through the middle of the microcapsules shows the fiber concentration is quite large at the edge, but drops off quickly moving toward the core, Figure 6.3a.3 and Figure 6.3b.3. With increasing cultivation time, bacteria reproduce and make more fibers in both the shell and core regions, forming porous elastic spheres. It is interesting to note here that, unlike typical polymer capsules, these structures have an internal organization more similar to a biological cell, as the nanofibers create a sort of cytoskeleton that can organize and protect contents while still allowing transport of molecules by diffusion. After two weeks of cultivation, the relative fiber density at the boundary of the capsule remains higher than in the center as more growth tends to occur near the liquid-liquid interface.

We observe the bacteria mainly distributed at the surface of microcapsules, with a smaller fraction also clustered in one spot that was the microcapsule bottom during growth, Figure 6.3a.2 and Figure 6.3b.2. The capsules form in the droplet by growth of cellulose from the bacterial cells, so their location sets the location of the fibers produced. The capsules have a fairly uniform coating of cellulose over their surface, so the bacteria are evenly distributed throughout the liquid-liquid interface, despite gravitational force directing their movement up. The surface of *Acetobacter xylinum* is hydrophilic and slightly negatively charged.<sup>39</sup> The surface energy between water and oil is normally high, so the bacteria behave like most solid particles that tend to adsorb onto a liquid-liquid interface.<sup>7,40,41</sup> Over time, bacteria grow and distribute more throughout the drop volume, consistent with a previous study of bacterial biofilm growth in monodisperse emulsion drops.<sup>27</sup> As a result, the cellulose matrix grows inward from the interface to yield a core-shell type of capsule structure. The microstructure of microcapsules is strongly correlated with the mechanical properties, which can be characterized by single particle deformation, and permeability that can be estimated from pore size and membrane thickness.

The thickness of the microcapsule shell is characterised by confocal images of Congo red-dyed microcapsules. Figure 6.4a shows an example image of a cellulose microcapsule taken at low magnification, exhibiting higher intensity of fibers at the boundary than the center. Quantitative fluorescent intensity of the microcapsule as a function of distance from the capsule center is plotted in Figure 6.4b for four different orientations of a radial vector. In Figure 6.4b the intensity has a peak near the outer surface, followed by a low intensity region through the capsule center. An estimate of capsule shell thickness was determined by assuming the inner boundary of the shell occurs where the maximum intensity reduced to 80% of its peak value,

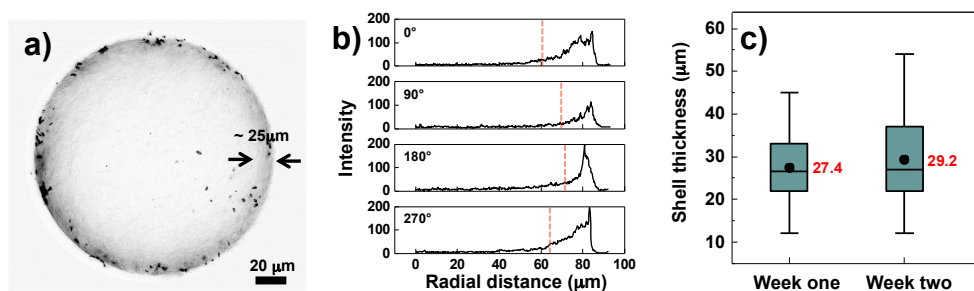


**Figure 6.4:** A one week old cellulose microcapsule imaged under a confocal microscope after dyeing with Congo red (a). The intensity of fibers is high at the capsule edges but decays quickly to the center, indicating the shell thickness is around 25  $\mu\text{m}$  for this typical microcapsule (b). The measured thickness of cellulose microcapsules has a large distribution and almost independent of incubation time (c).

giving an average 25  $\mu\text{m}$  thickness for the microcapsule in Figure 6.4a. A red vertical dashed line in Figure 6.4b indicates the point where the drop in intensity defines the inner edge of the shell, and that the shell thickness varies by only a small amount around the capsule surface. The thickness of the shells is not uniform, likely because of variations in cell density during initial formation and growth, as mentioned above in Figure 6.3.

The dependence of shell thickness on the time of cultivation is shown in Figure 6.4c. At least 20 measurements were performed for each growth time. Half of the data distributes within the box, and the error bars cover all results. The horizontal line in each box is the median value. We found that the data have a broad distribution, and the thickness of the shell did not increase significantly with time in the two weeks examined, though higher fiber concentrations were observed for long cultivation time in Figure 6.3. The average wall thickness is around 30  $\mu\text{m}$ . Although we focused on the shell thickness changing as the cultivation time was extended, the porosity of the membrane structure and the overall mechanical strength could also be changed due to higher fiber density over a longer fermentation. As the capsule

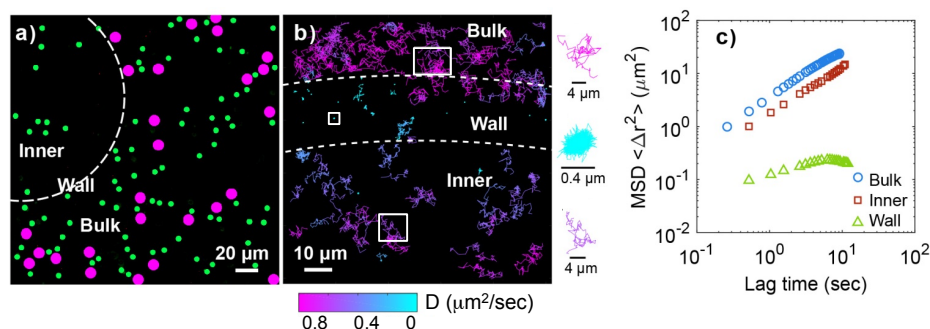


**Figure 6.5:** Cellulose capsules excluded 1  $\mu\text{m}$  tracer particles, marked as magenta, in the bulk solution, while 0.5  $\mu\text{m}$  tracers, colored green, can freely diffuse inside (a). The trajectories show the diffusivity of 0.5  $\mu\text{m}$  tracers in the bulk solution, on the membrane, and inside of the microcapsule, with representative trajectories plotted on the right (b), and the MSD are plotted as a function of lag time for the three locations in the capsule (c).

structure can act as a membrane of sorts, we are also interested in their permeability to external materials.

The barrier properties of the cellulose microcapsule surface were explored by observing diffusion of different sizes of colloidal tracer particles from the bulk solution into the microcapsules. After at least three hours contact in water, 1  $\mu\text{m}$  tracers remained entirely outside of the cellulose microcapsule, as seen from the location of the magenta particles in Figure 6.5a. However, a number of 0.5  $\mu\text{m}$  tracers, marked green in Figure 6.5a, were observed inside of the microcapsule, indicating the capsule membrane pore size is between 0.5  $\mu\text{m}$  and 1  $\mu\text{m}$ . The diffusive dynamics of 0.5  $\mu\text{m}$  tracers, inside the microcapsule, within its wall, and in the bulk solution, were further studied using single particle tracking.

The mobility of colloidal tracer particles is determined by tracking their positions using image frames like Figure 6.5a, producing random walk trajectories like those in Figure 6.5b, that indicate the degree to which fiber constraints hinder particle diffusion. Particle trajectories indicate freely diffusive behavior inside and outside of the microcapsule, but very restricted particle mobility in the capsule

shell, where fiber density is highest, Figure 6.5b. The mobility of the particles in the different regions was characterized by the mean squared displacement, or MSD, in Figure 6.5c.<sup>42</sup> The particles in the bulk solution exhibit unrestricted diffusion, while the MSD of the particles dramatically decreases inside the capsule shell, indicating limited mobility there. A plateau in the MSD was also observed over time in the capsule shell, revealing some particles were trapped within the wall of the microcapsule and that the pore size distribution there is heterogeneous. Such behavior is consistent with previously observed hindered motion of particles in pores.<sup>43,44</sup> Once through the shell, however, most particles are quite mobile inside or outside of the capsule, exhibiting nearly free diffusion. The MSD of the particles in the microcapsule is slightly lower than outside, but remained linear with the lag time, which is an indicator of simple diffusive dynamics. The large particle mobility inside the capsules indicates that, on average, the internal network pore size is significantly larger than the particle size. Extending the cultivation time can increase fiber density, providing a straightforward approach to adjust the porosity of cellulose microcapsules.

The flow of fluids through porous membrane per unit time,  $\dot{Q}_f$ , can be described as:<sup>45,46</sup>

$$\dot{Q}_f = \frac{kA_m\Delta P}{\eta\Delta x} \quad (6.1)$$

where  $k$  is permeability of the membrane,  $A_m$  is membrane area,  $\Delta P$  is pressure difference across membrane,  $\eta$  is fluid viscosity and  $\Delta x$  is membrane thickness. Physically, membrane filtration can be treated as flow through  $N$  cylindrical pores, with radius  $r$  and length  $\Delta x$ . We can apply Poiseuille's law and solve:<sup>47</sup>

$$\dot{Q}_f = \frac{N\pi r^4\Delta P}{8\eta\Delta x} = \frac{A_p r^2\Delta P}{8\eta\Delta x} \quad (6.2)$$

here  $A_p$  is the membrane pore area. From Equation 6.1 and 6.2, we find:<sup>45</sup>

$$k = \frac{r^2}{8} \times \frac{A_p}{A_m} \quad (6.3)$$

Since the cellulose fibers are nanoscale in width and the cellulose membrane structure is very porous, the porosity of the membrane is  $> 0.99$ . The hydrodynamic permeability of the membrane is then approximated by:

$$k \approx \frac{r^2}{8} \quad (6.4)$$

Having determined the pore size above, we obtain a permeability for a cellulose microcapsule membrane at 0.67% v/v on the order of  $k \sim 5 \times 10^{-14} \text{ m}^2$ , giving free and fast exchange of solutes with the bulk environment. The magnitude is consistent with more conventional cellulose porous media at similar fiber density<sup>48</sup>.

The porous cellulose microcapsules can then achieve fast diffusion of small molecules into the capsules, including DNA and proteins, but block out the large particles,  $> 1 \mu\text{m}$ , like bacteria. One potential application for cellulose microcapsules is providing a protective enclosure barrier for mammalian cells without harming the nutrient diffusion from the bulk environment. The cellulose membrane could prevent the contamination of mammalian cells, with the sizes between  $10 \mu\text{m}$  and  $100 \mu\text{m}$ , from all fungi and the majority of bacteria, such as *E. coli* which are larger than  $1 \mu\text{m}$ . Encapsulating mammalian cells into cellulose microcapsules also can benefit traditional anti-body production. For instance, the anti-bodies secreted from the cells can freely diffuse into the medium and be harvested and purified. At the same time, the cells are still alive and keep producing anti-bodies after adding fresh medium.

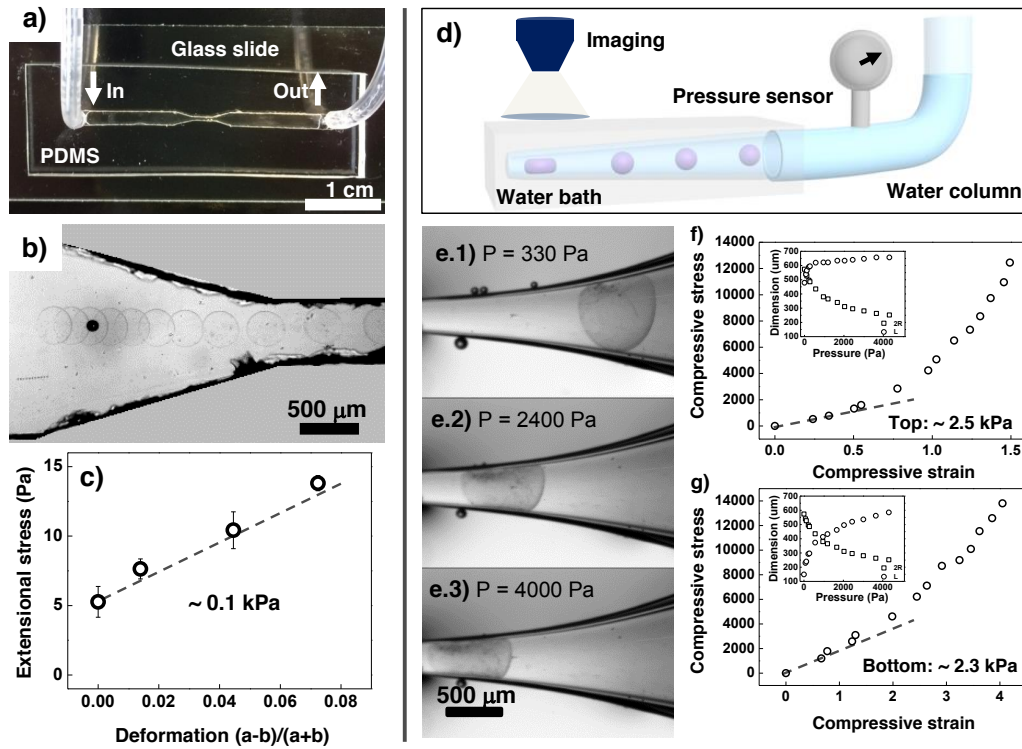


**Figure 6.6:** Cellulose microcapsules were deformed under an extensional flow in a designed PDMS channel (a). The composite images show the deformation of microcapsules when passing the constriction (b). The slope of the stress and deformation plot indicates the elasticity of the microcapsules, around 110 Pa for this targeted microcapsule (c). Schematic of microcapillary setup for measurement of compressive modulus via applied pressure in a tapered channel (d). Images of a capsules being moved along a capillary by increasing pressure (e). Plots of the stress and strain measured by image analysis for the capsules in (e) are shown in (f) and (g).

The mechanical properties of the microcapsules are strongly associated with their stability during processing and use. The particles may collapse, rupture or experience complex shape deformation in a shear flow. For fluid-filled membrane shells with finite permeability, the deformation is more complicated than for empty and solid microcapsules. The original volume of the deformable microcapsules is not preserved under larger deformation, since the inside fluids are incompressible. Although the motion of fluids displays a significant role in large microcapsule deformations, small deformations of less than 20% strain, are dominated by bending and do not yield any difference between empty and fluid-filled shells.<sup>49</sup> Small deformation of microcapsules is also reversible and independent of permeability. The inherent elasticity of microcapsules can then be measured by monitoring the shape changes, during small deformation, under controlled stress.<sup>33,34</sup>

The elasticity of microcapsules was measured by observing their deformation in an extensional flow in a microfluidic channel, Figure 6.6a. A microchannel constriction generates an extensional flow field along the flow direction that can deform microcapsules. The progression of changes from a spherical shape by a ten-day-old microcapsule is shown in several superpositioned image frames, Figure 6.6b. The microcapsule elongates slightly along the flow when approaching the constriction. The shape of the microcapsule was not imaged after the extensional stress was removed, due to the restricted views of the microscope. The elasticity value of the microcapsule was obtained from the slope of a plot of applied extensional stress versus the particle deformation response.<sup>50</sup> For a typical microcapsule shown in Figure 6.6b, the elasticity is around 110 Pa, Figure 6.6c. However, the extensional stresses generated from the flow were not high enough to deform all microcapsules in the sample, which indicates only capsules with the lowest elastic modulus were measured here.

Capillary mechanics allow application of a larger range of stresses to the microcapsules, Figure 6.6d. The technique applies several step increases in applied stress to a capsule blocking the capillary tip, moving it further along and deforming it by an amount we can quantify via image analysis. The deformation of the microcapsule in the constriction is caused by the applied hydrodynamic and radial pressure from the glass wall.<sup>36</sup> Examination of the behavior of a capsule during linear and nonlinear elastic deformation events, as well as their recovery from such events, provides valuable insight into the dynamic behavior of these capsules in diverse flow and confinement situations.

Figures 6.6 e.1-6.6e.2 show images of a microcapsule under increasing applied stress levels and the deformation it exhibits at each stage, along with the calculated stress and strain plotted in Figure 6.6f and Figure 6.6g for a ten-day-old microcapsule. The regimes of linear deformation at small strains, and nonlinear deformation at large strains, are both apparent. The linear deformation behavior allows an estimate of the compressive modulus to be obtained, and we find the capsules exhibit large variation of overall elasticity, ranging from hundreds of Pa to a few kPa in a population. Precisely controlling the bacteria concentration in each droplet and incubating environment, such as oxygen exposure and temperature, would likely reduce the variation in capsule strength. The mechanical properties of cellulose microcapsules can be further modified, such as adding binding polymers and other reinforcements to modify elasticity and permeability.<sup>13</sup> The overall softness of the cellulose microcapsules is several orders of magnitude smaller than other reported microcapsules.<sup>5,16</sup> The flexibility of bacterial cellulose and the highly porous cellulose microstructure are fundamental to the softness, which significantly affects the deformability in constrictions and is increasingly attractive in biological applica-

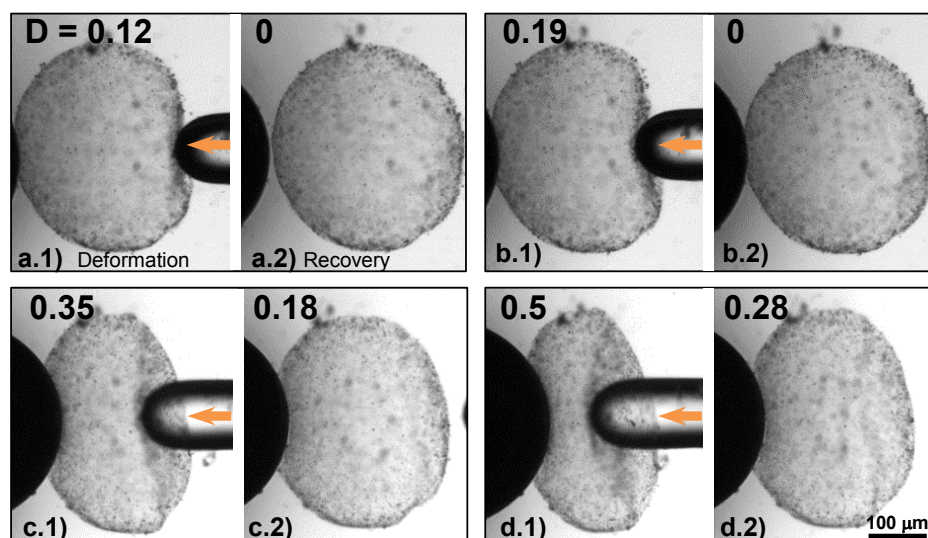


**Figure 6.7:** Deformation and recovery of microcapsules using microcapillary manipulation. The microcapsules were deformed by a capillary tip, and the arrows indicate the direction of compression. The spherical shape is recovered at low levels of strain (a-b) but is permanently deformed at high strains (c-d).

tions.<sup>51</sup> For instance, extraordinarily flexible microparticles could mimic red blood cells.<sup>5</sup>

The reversibility of the capsule deformation was studied by repeatedly deforming a capsule using a microcapillary tip to apply increasing levels of strain, Figure 6.7. At small strains, the cellulose microcapsule was deformed elastically, Figures 6.7a and 6.7b, with the spherical shape fully recovered after the stress is removed. The capsule transitions to only partial recovery above a strain of about 20%, but does not exhibit any obvious damage, and simply adopts a new shape, Figures 6.7c and 6.7d. Cellulose microcapsules fold under such point indentation, unlike other capsules that form small holes due to buckling and wrinkling.<sup>52,53</sup> The folding of the porous membrane under deformation is expected to be dominated by bending, similar to porous pollen folding under drying.<sup>14</sup> Self-folding and ordering in single cellulose nanofibril were also observed under confinement.<sup>54</sup> Although large-strain deformation causes unrecoverable change from the spherical shape of microcap-

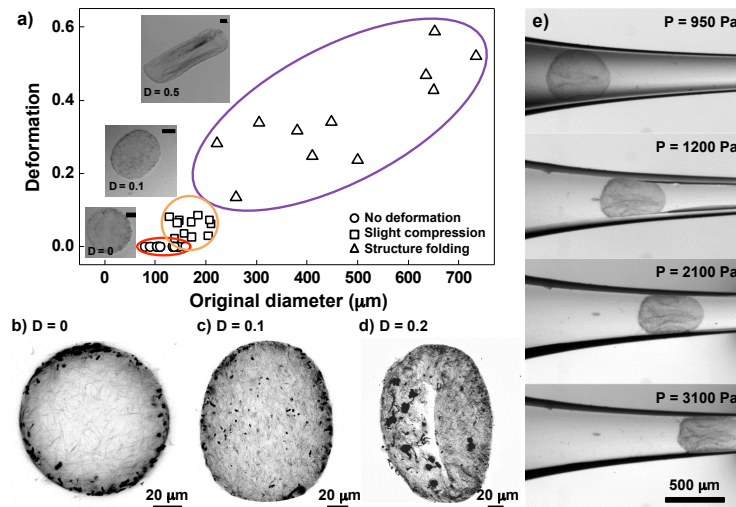


**Figure 6.8:** Three deformation regimes of cellulose microcapsules: elastic deformation, subtle compression or stretching, and structure folding (a). The inset images are the deformed particles in different regimes, and the corresponding fiber network changes are shown below. (b) and (c) are confocal slices through the middle of the capsule, while (d) is through the mid-plane of the folded region nearer the capsule edge. Adjustable shapes of cellulose microcapsules under significant compression is shown in (e).

sules, the membrane retains its overall integrity. No significant fiber network rupture was observed on the microcapsule surface after high levels of compression. We next characterize the folding behavior of the capsules in order to understand their ability to adapt to deformation.

The deformation,  $D$ , of capsules with a long axis  $a$  and short axis  $b$  can be calculated using:<sup>35</sup>

$$D = \frac{a - b}{a + b} \quad (6.5)$$

We plot values of microcapsule deformation in Figure 6.8a as a function of the original capsule diameter in order to classify the range of response we observe to flow through constrictions. Three deformation regimes are identified and grouped in Figure 6.8a: a fully recovered sphere, Figure 6.8b, a slightly compressed sphere with no significant folding or buckling, Figure 6.8c, and a structure with significant buck-

ling that enables shape change and adaptation during flow, Figure 6.8d. The results in Figure 6.8 are consistent with an energetic picture of a deforming capsule finding it easier to compress or stretch than to fold. At higher strains folding becomes preferred.

The dynamic process of shape adaptation possible for these capsules during deformation in a converging channel with pressure increasing is shown in Figure 6.8e. As the microcapsule is forced through a pulled capillary with a decreasing diameter, multiple wrinkles developed during compression. The shape adaptation allows the capsule to pass steadily through the constriction. We speculate that the pore size characterized in Figure 6.5 may be altered by the adaptations, but we have not yet quantified whether this is true. The soft microcapsules fold their shapes under large stresses, instead of breaking their fiber networks, as might occur for more rigid microcapsules. Fiber networks are highly resistant to stretching, but they can easily bend under compression, and avoid catastrophic fracture of the entire network. The folding of fiber networks may also be reversible,<sup>55</sup> so that an expanding force could potentially reshape the compressed microcapsules into their original spherical form. The high tensile strength of the cellulose membrane should be able to withstand large stretching, and provide a robust protective barrier for encapsulated components while preventing their escape.<sup>56</sup> The dynamics of the compressed microcapsule structure changes in Figure 6.8 are evocative of the pollen drying process, and provide a basis for study of the deformation behaviors of fluid-filled porous shells.<sup>14</sup>

## 6.4 Conclusions

Cellulose microcapsules have been successfully fabricated through a simple emulsion-based fermentation process, constraining growth of bacterial cellulose to liq-

uid-liquid interfaces. The sparse fiber networks can form capsular membranes with densities as low as  $0.01 \text{ g/cm}^3$ . The total mass of cellulose production increased with incubation time, while the thickness of the shell did not change significantly. The pore sizes of the cellulose membranes are on the order of  $0.5 \mu\text{m}$ , allowing relatively free exchange of solutes, but blocking particles and microorganisms larger than  $1 \mu\text{m}$  in diameter. The capsules have low elasticity, around  $100 \text{ Pa}$ , but surprising resilience during deformation due to the high tensile strength of the cellulose microstructure. Changing the growth conditions, like bacteria concentration, oxygen supply and incubation time, could effectively adjust the total mass of cellulose production, and thus alter the membrane porosity and mechanical strength as well. The modification of membrane thickness could be achieved through growing cellulose in double emulsions with more controlled thickness of water layer.

The work demonstrates the ability to physically engineer structures made by bacterial fermentation, using constraints provided by interfacial adsorption forces. While most microcapsule fabrication aims to encapsulate and provide slow release of actives, the production of soft, strong, porous microcapsules could enable new applications like protecting living cells and isolating extracellular compounds. Cellulose microcapsules could also potentially act as artificial cells, as they combine a porous outer wall with an inner cytoskeleton of nanofibers that gives them a flexibility reminiscent of, for example, red blood cells.

## 6.5 References

- [1] S. de Koker, R. Hoogenboom, B. G. De Geest, *Chemical Society Reviews* **2012**, *41*, 2867–2884.
- [2] S. D. Hann, T. H. Niepa, K. J. Stebe, D. Lee, *ACS App. Matls. Interfaces* **2016**, *8*, 25603–25611.

## References

---

- [3] Q. Ma, Y. Song, J. W. Kim, H. S. Choi, H. C. Shum, *ACS Macro Letters* **2016**, *5*, 666–670.
- [4] H. Sun, E. H. Wong, Y. Yan, J. Cui, Q. Dai, J. Guo, G. G. Qiao, F. Caruso, *Chemical science* **2015**, *6*, 3505–3514.
- [5] T. J. Merkel, S. W. Jones, K. P. Herlihy, F. R. Kersey, A. R. Shields, M. Napier, J. C. Luft, H. Wu, W. C. Zamboni, A. Z. Wang, J. E. Bear, J. M. DeSimone, *Proceedings of the National Academy of Sciences* **2010**, 586–591.
- [6] G. Kaufman, S. Nejati, R. Sarfati, R. Boltyanskiy, M. Loewenberg, E. R. Dufresne, C. O. Osuji, *Soft Matter* **2015**, *11*, 7478–7482.
- [7] A. Dinsmore, M. F. Hsu, M. Nikolaidis, M. Marquez, A. Bausch, D. Weitz, *Science* **2002**, *298*, 1006–1009.
- [8] R. K. Shah, J.-W. Kim, D. A. Weitz, *Langmuir* **2009**, *26*, 1561–1565.
- [9] V. Mohanta, G. Madras, S. Patil, *ACS App. Matls. Interfaces* **2014**, *6*, 20093–20101.
- [10] L. M. Sagis, R. de Ruiter, F. J. R. Miranda, J. de Ruiter, K. Schroën, A. C. van Aelst, H. Kieft, R. Boom, E. van der Linden, *Langmuir* **2008**, *24*, 1608–1612.
- [11] D. F. Do Nascimento, J. A. Avendaño, A. Mehl, M. J. Moura, M. S. Carvalho, W. J. Duncanson, *Scientific reports* **2017**, *7*, 11898.
- [12] A. Fery, F. Dubreuil, H. Möhwald, *New journal of Physics* **2004**, *6*, 18.
- [13] G. Kaufman, S. Mukhopadhyay, Y. Rokhlenko, S. Nejati, R. Boltyanskiy, Y. Choo, M. Loewenberg, C. O. Osuji, *Soft matter* **2017**, *13*, 2733–2737.
- [14] E. Katifori, S. Alben, E. Cerda, D. R. Nelson, J. Dumais, *Proceedings of the National Academy of Sciences* **2010**, *107*, 7635–7639.
- [15] A. Fery, R. Weinkamer, *Polymer* **2007**, *48*, 7221–7235.
- [16] J. Cui, M. Björnmalm, K. Liang, C. Xu, J. P. Best, X. Zhang, F. Caruso, *Advanced Materials* **2014**, *26*, 7295–7299.
- [17] M. Iguchi, S. Yamanaka, A. Budhiono, *Journal of Materials Science* **2000**, *35*, 261–270.
- [18] M. J. Solomon, P. T. Spicer, *Soft Matter* **2010**, *6*, 1391–1400.
- [19] J. Song, M. Caggioni, T. M. Squires, J. F. Gilchrist, S. W. Prescott, P. T. Spicer, *Rheologica Acta* **2019**, *58*, 217–229.

- 
- [20] J. Song, M. Caggioni, T. M. Squires, J. F. Gilchrist, S. W. Prescott, P. T. Spicer, *Rheologica Acta* **2019**, *58*, 231–239.
- [21] D. Klemm, F. Kramer, S. Moritz, T. Lindström, M. Ankerfors, D. Gray, A. Dorris, *Angewandte Chemie International Edition* **2011**, *50*, 5438–5466.
- [22] F. Torres, S. Commeaux, O. Troncoso, *Journal of Functional Biomaterials* **2012**, *3*, 864–878.
- [23] B. V. Mohite, B. K. Salunke, S. V. Patil, *Applied biochemistry and biotechnology* **2013**, *169*, 1497–1511.
- [24] M. Schaffner, P. A. Rühs, F. Coulter, S. Kilcher, A. R. Studart, *Science Advances* **2017**, *3*, eaao6804.
- [25] S. Kyle, *Trends in biotechnology* **2018**, *36*, 340–341.
- [26] M. K. Hausmann, P. A. Ruhs, G. Siqueira, J. Lauger, R. Libanori, T. Zimmermann, A. R. Studart, *ACS nano* **2018**, *12*, 6926–6937.
- [27] C. B. Chang, J. N. Wilking, S.-H. Kim, H. C. Shum, D. A. Weitz, *Small* **2015**, *11*, 3954–3961.
- [28] T. H. Niepa, L. Hou, H. Jiang, M. Goulian, H. Koo, K. J. Stebe, D. Lee, *Scientific reports* **2016**, *6*, 30578.
- [29] T. S. Kaminski, O. Scheler, P. Garstecki, *Lab on a Chip* **2016**, *16*, 2168–2187.
- [30] J. Schindelin, I. Arganda-Carreras, E. Frise, V. Kaynig, M. Longair, T. Pietzsch, S. Preibisch, C. Rueden, S. Saalfeld, B. Schmid, J.-Y. Tinevez, D. J. White, V. Hartenstein, K. Eliceiri, P. Tomancak, A. Cardona, *Nature Methods* **2012**, *9*, 676.
- [31] C. A. Schneider, W. S. Rasband, K. W. Eliceiri, *Nature Methods* **2012**, *9*, 671.
- [32] T. G. Mason, D. Weitz, *Physical review letters* **1995**, *74*, 1250.
- [33] J. T. Cabral, S. D. Hudson, *Lab on a Chip* **2006**, *6*, 427–436.
- [34] J. D. Martin, J. N. Marhefka, K. B. Migler, S. D. Hudson, *Advanced materials* **2011**, *23*, 426–432.
- [35] H. A. Stone, L. Leal, *Journal of Fluid Mechanics* **1990**, *211*, 123–156.
- [36] H. M. Wyss, T. Franke, E. Mele, D. A. Weitz, *Soft Matter* **2010**, *6*, 4550–4555.

## References

---

- [37] T. Kong, L. Wang, H. M. Wyss, H. C. Shum, *Soft matter* **2014**, *10*, 3271–3276.
- [38] D. Chong, X. Liu, H. Ma, G. Huang, Y. L. Han, X. Cui, J. Yan, F. Xu, *Microfluidics and Nanofluidics* **2015**, *19*, 1071–1090.
- [39] C. Krekeler, H. Ziehr, J. Klein, *Applied microbiology and biotechnology* **1991**, *35*, 484–490.
- [40] L. S. Dorobantu, A. K. Yeung, J. M. Foght, M. R. Gray, *Applied and Environmental Microbiology* **2004**, *70*, 6333–6336.
- [41] P. A. Rühls, L. Böcker, R. F. Inglis, P. Fischer, *Colloids and Surfaces B: Biointerfaces* **2014**, *117*, 174–184.
- [42] E. M. Furst, T. M. Squires, *Microrheology*, Oxford University Press, **2017**.
- [43] M. J. Skaug, D. K. Schwartz, *Industrial & Engineering Chemistry Research* **2015**, *54*, 4414–4419.
- [44] S. L. Eichmann, B. Smith, G. Meric, D. H. Fairbrother, M. A. Bevan, *Acs Nano* **2011**, *5*, 5909–5919.
- [45] J. Pappenheimer, E. Renkin, L. Borrero, *American Journal of Physiology-Legacy Content* **1951**, *167*, 13–46.
- [46] E. M. Renkin, *The Journal of general physiology* **1954**, *38*, 225–243.
- [47] S. P. Sutera, R. Skalak, *Annual review of fluid mechanics* **1993**, *25*, 1–20.
- [48] G. W. Jackson, D. F. James, *The Canadian Journal of Chemical Engineering* **1986**, *64*, 364–374.
- [49] L. Taber, *Journal of Applied Mechanics* **1982**, *49*, 121–128.
- [50] K. A. Erk, J. D. Martin, J. T. Schwalbe, F. R. Phelan Jr, S. D. Hudson, *Journal of colloid and interface science* **2012**, *377*, 442–449.
- [51] H. Sun, M. Björnmalm, J. Cui, E. H. Wong, Y. Dai, Q. Dai, G. G. Qiao, F. Caruso, *ACS Macro Letters* **2015**, *4*, 1205–1209.
- [52] S. S. Datta, S.-H. Kim, J. Paulose, A. Abbaspourrad, D. R. Nelson, D. A. Weitz, *Physical review letters* **2012**, *109*, 134302.
- [53] B. Li, Y.-P. Cao, X.-Q. Feng, H. Gao, *Soft Matter* **2012**, *8*, 5728–5745.

- [54] K. B. Smith, J.-N. Tisserant, S. Assenza, M. Arcari, G. Nyström, R. Mezzenga, *Advanced Science* **2019**, *6*, 1801540.
- [55] O. Chaudhuri, S. H. Parekh, D. A. Fletcher, *Nature* **2007**, *445*, 295.
- [56] S. Wang, F. Jiang, X. Xu, Y. Kuang, K. Fu, E. Hitz, L. Hu, *Advanced Materials* **2017**, *29*, 1702498.



## Chapter 7

### Conclusions and future work

Microstructural effects on suspension and yielding are investigated in this thesis for aqueous dispersions of bacterial cellulose fibers. Contrary to spheres, large aspect ratio fibers are more efficient in building colloidal gels at low concentrations by attractive interactions and entanglements. Using the stable microfibrillar cellulose (MFC) dispersions as suspending agents is of particular value, so the mechanism of fiber network yielding was explored to explain the fundamental reasons that result in better suspension ability than in the gels composed of spheres.

The suspension and yielding of sparse gels with fiber networks were studied using a small suspended air bubble as a sensitive probe particle. An external pressure field was used to control the applied stress and characterize very early stages of fluid yielding, as well as more developed flow. The bubble allows sensitive measurement of small yield stress values, but also indicates a discrepancy between bulk and microscale yield stress values. The size of the yielded region in the gels varied inversely with fiber concentration, but did not fully account for the bulk-microscale discrepancies, indicating the gels are restructuring, responsive fluids. Tracking of trapped tracer particles directly indicates local restructuring occurs in fiber networks, which drives heterogeneous yielding and flow. The observed heterogeneity effects decreased as fiber concentration increased, reducing network restructuring. The conventional yielding model assumes continuum flows, which poorly explains the yielding dynamics of gels with sparse microstructures. Better theory is thus

required to fully account for the heterogeneity and suspension performance in the gels composed of fibers.

By precisely controlling deformation rates in the bubble rheometer, significant variations were noted in suspension performance as a result of fiber rearrangement and heterogeneities. Strong strain rate dependencies were found to alter local network yield strength, and confocal microscopy quantified structural reinforcement and deformation rate effects. The transition to rate-dependent yielding was measured in different MFC gels, and the results agreed well with the predictions from a two-fluid model. The above results indicate a two-fluid description helps interpret sparse network flow and suspension properties. Building the bubble rheometer with a computer-controlled pressure system would enhance our ability to study network deformation under different conditions and further test the two-fluid formulation. For example, oscillating the applied pressure can more precisely expand and shrink bubbles to map the response and recovery time of the fiber networks.

In this thesis, applications of the fiber networks were also studied to assess performance when suspending heavy particles in formulated products, as well as coating tissue surfaces for enhanced nasal drug delivery. Controlled particle loads were used to study sedimentation behaviour of low concentration MFC gels under increased gravitational stress. The bulk collapse of MFC gels at different concentrations and gravitational stresses falls into two regions, fast yielding and poroelastic compression, as a result of competition between gel yield stress and gravitational stress. Contrary to gels of spherical particles, there is no delayed collapse, and the microstructure rearrangement is highly responsive to local stresses that decay as sample height is reduced. The rates of initial settling in both cases were back-flow limited, and increasing the fluid viscosity proportionally reduced sedimentation rates. The dimensionless permeability was also quantified and shown to scale

---

linearly with increasing fiber concentration. This work demonstrated methods of predicting long-term gel collapse behavior, avoiding costly long-term aging studies, as well as how to tune collapse time scales via simple formulation variables.

In addition to a unique suspension ability, MFC also provides improved coating performance for fluids thickened and longer retention time. The rheological properties of fluids were characterized and related to the coating performance in a nasal spray process. Compared to conventional excipients commonly used in nasal spray formulations, the MFC dispersions were more shear-thinning, which means the fluids can easily flow under high shear rates but quickly recover as the shear was removed. The low viscosity of MFC dispersions at high shear rates is beneficial to the nasal spray when compared to thickeners that merely increase viscosity. Future testing should be carried out on biological tissue, with incorporated drug particle mimics to assess the overall performance.

Engineering fiber networks was also carried out by controlling the dynamics of bacteria at an emulsion interface during fermentation to produce strong, but flexible, porous microcapsules from bacterial cellulose at an oil-water emulsion interface. A broad range of microcapsule sizes has been successfully produced, from 100  $\mu\text{m}$  to 5 cm in diameter. The three-dimensional capsule microstructure was imaged using confocal microscopy, showing a cellulose membrane thickness around 30  $\mu\text{m}$  that is highly porous, with some pores larger than 0.5  $\mu\text{m}$  that are permeable to most macromolecules by free diffusion, but can exclude larger structures like bacteria. The mechanical deformation of cellulose microcapsules reveals their flexibility, enabling them to pass through constrictions with a much smaller diameter than their initial size by bending and folding, all without damaging membrane integrity. Our work provides a new approach for producing soft, permeable and bio-compatible microcapsules for substance encapsulation and protection. The

capsules may offer a replacement for suspended polymer beads in commercial applications, and could potentially act as a framework for artificial cells. In the future, more efforts should be placed on modifying microcapsule surfaces to add desirable functions. For instance, polymerizing PLGA on a cellulose microcapsule template could produce temperature and pH-responsive structures.

## Appendix A

### Supplementary information for Chapter 2

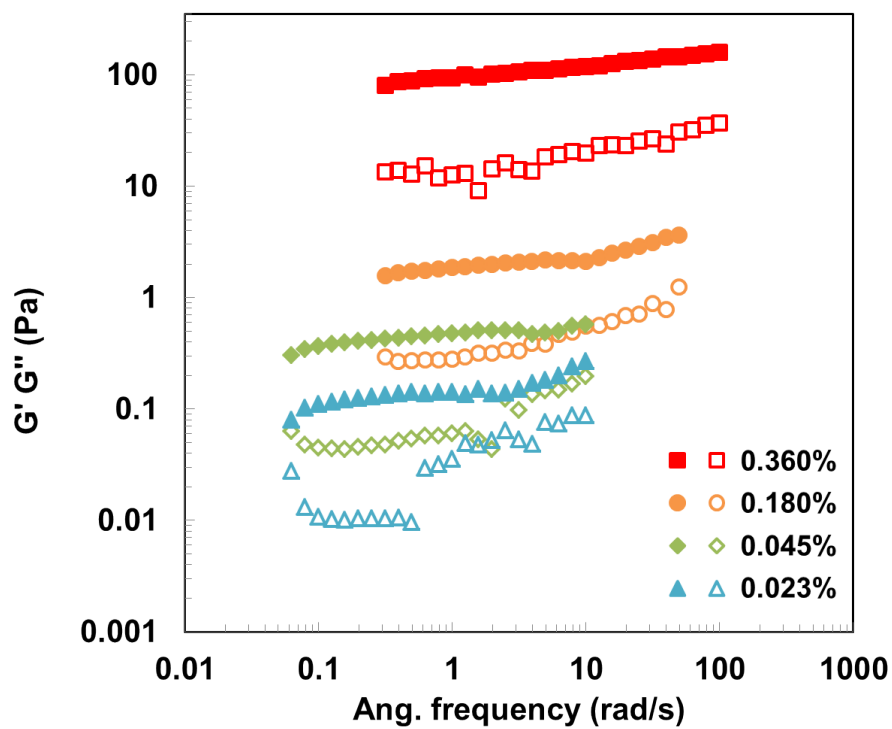


**Figure A.1:** In the linear elastic region, the values of  $G''$  (open symbols) are lower than  $G'$  (solid symbols) in all MFC dispersions measured here, indicating the formation of the gel structure.

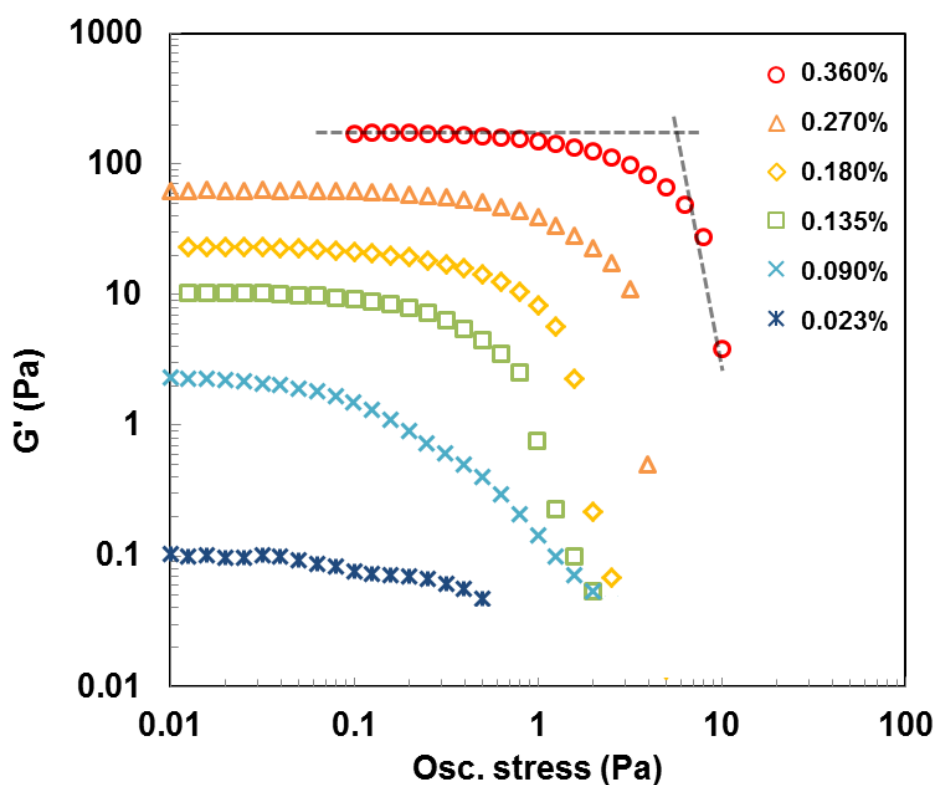


**Figure A.2:** The plateau elasticity of MFC gels was determined from the low stress region of the data. The  $G'$  decreased with increasing oscillatory stress as the microstructure was disrupted. The gel static yield stress is determined as the point of intersection between dash lines drawn through the plateau and declining regions.

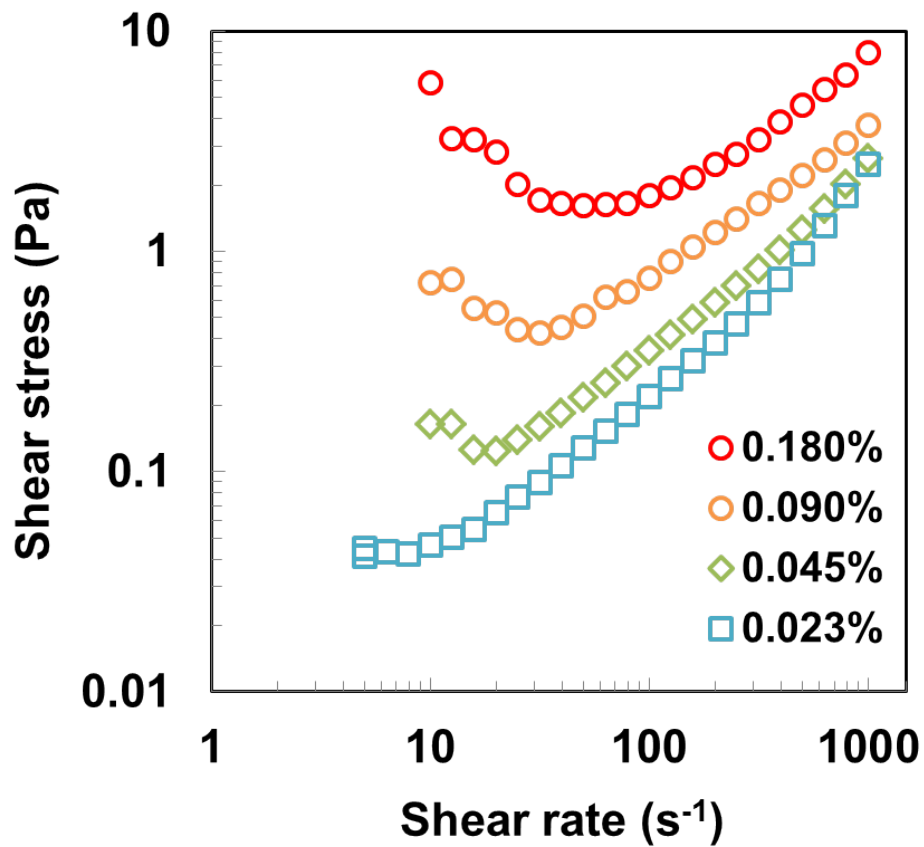


**Figure A.3:** The fluid shear stress decreased with decreasing shear rate, but then increased when the applied shear rate was smaller than a critical value related to the characteristic time of re-agglomeration. Only the data above the critical shear rates were used to fit the Herschel-Bulkley model.